Engineering Optical Properties Using Layered Metamaterials

by

Mohammed Hashim Al Shakhs

B.Sc. Hons., King Fahd University of Petroleum and Minerals, 2004
M.Sc., Dalhousie University, 2011

A THESIS SUBMITTED IN PARTIAL FULFILLMENT OF
THE REQUIREMENTS FOR THE DEGREE OF

DOCTOR OF PHILOSOPHY

in

The College of Graduate Studies

(Electrical Engineering)

THE UNIVERSITY OF BRITISH COLUMBIA

(Okanagan)

August 2017

The undersigned certify that they have read, and recommend to the College of Graduate Studies for acceptance, a thesis entitled: Engineering Optical Properties Using Layered Metamaterials submitted by Mohammed Hashim Al Shakhs in partial fulfilment of the requirements of the degree of Doctor of Philosophy

Dr. Kenneth Chau, School of Engineering

Supervisor, Professor

Dr. Loïc Markley, School of Engineering

Supervisory Committee Member, Professor

Dr. André Phillion, School of Engineering

Supervisory Committee Member, Professor

Dr. Murray Neuman, School of Arts and Sciences

University Examiner, Professor (please print name and faculty/school above the line)

Dr. Lora Ramunno, Department of Physics, University of Ottawa

External Examiner, Professor (please print name and faculty/school above the line)

(Date Submitted to Grad Studies)

Abstract

This thesis explores the concept of metamaterials; a fairly recent concept in the literature which has attracted the attention of researchers due to their abnormal electromagnetic properties. We will particularly consider one dimensional version of a metamaterial made of layers. At the first glance, layered metamaterials are simply multi-layer thin films. The distinguishing feature of layered metamaterials is that they usually incorporate metals whereas most thin film structures in the past have only incorporated dielectrics. The immense interest in certain layered configurations of metals and dielectrics, particularly when the thicknesses are really thin compared to the wavelength, is due to their exhibition of seemingly counter-intuitive or impossible properties such as refraction to the same side of normal (negative refraction), evanescent wave amplification, or light focusing with a flat interface (flat lensing). The simple configuration of layered metamaterials and their interesting properties are the prime motivations of this work. In this thesis, we first start with a very generic electromagnetic description of the optical properties of layered structures. This general description appears to be novel due to presenting theory in new form. We use this understanding to explain how and why certain layered structures can exhibit negative refraction or flat lensing. This investigation has also led to several new predictions of new optical properties of layered metamaterial structures. We conclude this work by various experimental studies which validate the predictions of the work and also explore fabrication challenges in the making of layered metamaterials.

Preface

This work has been done under the guidance of Dr. Kenneth Chau at the School of Engineering in The University of British Columbia. Portions of my thesis have been published in four journal articles:

- Al Shakhs, Mohammed, Lucian Augusto, Loïc Markley, and Kenneth J. Chau. "Boosting the Transparency of Thin Layers by Coatings of Opposing Susceptibility: How Metals Help See Through Dielectrics." Scientific reports, vol. 6 (2016).
- Ott, Peter, Mohammed H. Al Shakhs, Henri J. Lezec, and Kenneth J. Chau. "Flat lens criterion by small-angle phase." Optics express, vol. 22, pp. 29340-29355 (2014).
- Al Shakhs, Mohammed H., Peter Ott, and Kenneth J. Chau. "Band diagrams of layered plasmonic metamaterials." Journal of Applied Physics, vol. 116, pp. 173101 (2014).
- Kenneth J. Chau, Mohammed H. Al Shakhs, and Peter Ott, Fourier-Domain Electromagnetic Wave Theory for Layered Metamaterials of Finite Extent, Progress In Electromagnetics Research M, vol. 40, pp. 45-56 (2014).

Portions of my thesis have also been presented at the following conferences:

- Mohammed Al Shakhs, Lucian Augusto, Loïc Markley, and Kenneth Chau, Light Transmission Enhancement through a Thin Layer by a Coating of Opposing Susceptibility: How Metals Help See Through Dielectrics?, APS/IEEE International Symposium, Fajardo, Puerto Rico (2016).
- Mohammed H. Al Shakhs, Peter Ott, Henri J. Lezec, and Kenneth J. Chau, A General Flat-Lens Criterion, APS/IEEE International Symposium, Vancouver, Canada (2015).

– Mohammed H. Al Shakhs, Peter Ott, Henri J. Lezec, and Kenneth J. Chau, A General Flat-Lens Criterion, Photonics North, Ottawa, Canada (2015).

Table of Contents

List of Tables

List of Figures

Acknowledgements

It was certainly the blessing of God to be surrounded by many wonderful people throughout my Doctoral studies. I would like to take this opportunity to thank them all for their support. First of all, I would like to express my sincere gratitude to my PhD advisor, Dr. Kenneth Chau, for his unlimited support, guidance and encouragement throughout my PhD studies. Without his continuous support and confidence in my abilities conducting this work would not be possible. Working with him was a great opportunity. His words and attitude will be forever a source of inspiration.

I would like to sincerely thank Dr. Peter Ott from Heilbronn University and Dr. Loïc Markley from the University of British Columbia (UBC) for their significant contributions in this work. My sincere thanks also goes to Dr. Andre Phillion, the PhD committee member, for his valuable comments and suggestions that enriched my work. I am thankful to Dr. Thomas Johnson, Dr. Stephen OLeary and Cassidy Northway from UBC for their helpful discussions. I am grateful to Dr. Amit Agrawal from Syracuse University, and Dr. Henri Lezec, Dr. Vladimir Aksyuk and Dr. Alex Liddle from the National Institute of Standards and Technology for their helpful comments.

I would like to thank Dr. Deborah Roberts from UBC for giving me access to her microscope facility. I am grateful to Mark Nadeau and David Zinz for assisting me working on the nano-film deposition station at UBC. I am thankful to David Arkinstall for assisting me working on the Scanning Electron Microscope at UBC. I would like to thank Mario Beaudoin for his assistance with measurements made at the AMPEL Facility at UBC. I am also thankful to YaTung Cherng and Nathanael Sieb for taking the Atomic Force Microscopy images using the 4D LABS facilities at Simon Fraser University (SFU).

I would like to thank all my exceptional friends and research colleagues. Working beside Samuel Schaefer, Max Bethune-Waddell, Iman Aghanejad, Asif Alnoor, Masoud Ahmadi, and Vincent Loi was a great experience. I am especially thankful to Reyad Mehfuz, Lucian Augusto, and Cailan Libby for all the wonderful moments throughout our collaborative works.

Finally, I would like to thank each individual of my big family. My special thanks and appreciation to my parents, in-laws, sister, wife and kids for their sincere love and continuous encouragement. Words cannot express my appreciation...

Dedication

To the hidden sun behind the clouds

Chapter 1

Introduction

Controlling light requires rigorous understanding of the behaviour of electromagnetic waves in different media. In this thesis, we will study the interaction between electromagnetic waves and layered metamaterials, a simple thin film structure that uses thin metal layers to achieve abnormal light behaviour. The thickness of these layers is typically one tenth or less of wavelength of light. In the first part of the thesis, we focus our attention to the negative refraction property of such layered systems at optical frequencies. We start by examining the fundamental principles of electromagnetics to explain why and when a layered metamaterial can perform negative refraction. We develop explicit wave equations that describe electromagnetic wave propagation through thin film structures. The derived explicit solutions provide clear physical insights and shed the light on the correlation between the intrinsic electromagnetic properties and the external light behaviours. Based on this study, we develop two distinct methods to predict the imaging capability of layered metamaterials. In the second part of the thesis, we conclude the research with two experimental works. The first explores spectral light filtering and light transmission enhancement using bi-layer thin films of metal and dielectrics, and the second examines the influence of nano-film fabrication parameters on the surface optical resonances of thin metal films. The outcomes of this thesis work are explicit analytical solutions of the electromagnetic fields propagating through layered metamaterials, new design methods for layered metamaterials, and experimental investigations of enhancing light transmission and surface optical resonance of layered metamaterials.

1.1 Electromagnetic Wave Theory

The electromagnetic wave theory of light was established in 1873 by James Clerk Maxwell. In three dimensional vector notation, Maxwell's equations relate six real functions dependent on the position vector ($\vec{r}$) and the time variable (t); the electric field, $\vec{E}$, the magnetic field, $\vec{H}$, the electric displacement, $\vec{D}$, the magnetic flux density, $\vec{B}$, the electric current density, $\vec{J}$,

and the electric charge density, ρ. Maxwell's equations in their differential forms are given by

$$\vec{\nabla} \cdot \vec{D}(\vec{r},t) = \rho, \tag{1.1}$$

$$\vec{\nabla} \cdot \vec{B}(\vec{r},t) = 0, \tag{1.2}$$

$$\vec{\nabla} \times \vec{E}(\vec{r},t) = -\frac{\partial \vec{B}(\vec{r},t)}{\partial t}, \tag{1.3}$$

and

$$\vec{\nabla} \times \vec{H}(\vec{r},t) = \vec{J}(\vec{r},t) + \frac{\partial \vec{D}(\vec{r},t)}{\partial t}. \tag{1.4}$$

To solve for Maxwell's equations, typically we assume to have a charge free region where ρ is zero. However, still we have two independent equations and five unknowns. To overcome this problem, we need more relations. The two electric field vectors, $\vec{E}$ and $\vec{D}$, and the two magnetic field vectors, $\vec{H}$ and $\vec{B}$, can be often related to each other based on the electric and the magnetic properties, ϵ and μ, of the medium. Moreover, the electric field ($\vec{E}$) and the electric current density ($\vec{J}$) can be related to each other based on the conductivity (σ) of the medium. These relations, known as the constitutive relations, provide the required missing equations to solve for the electric and magnetic fields in Maxwell's equations.

In linear, isotropic, homogeneous and dispersionless media, the constitutive relations are:

$$\vec{D}(\vec{r},t) = \epsilon_r \epsilon_o \vec{E}(\vec{r},t), \tag{1.5}$$

$$\vec{B}(\vec{r},t) = \mu_r \mu_o \vec{H}(\vec{r},t), \tag{1.6}$$

and

$$\vec{J}(\vec{r},t) = \sigma \vec{E}(\vec{r},t), \tag{1.7}$$

where ϵ and σ are the constant electric properties of the medium, and μ represents the medium's constant magnetic property. These material properties will be discussed in details over the next section. Using the constitutive relation equations and assuming the region of interest is a charge free region ($\rho = 0$), Maxwell's equations can be re-written as:

$$\vec{\nabla} \cdot \vec{E}(\vec{r},t) = 0, \tag{1.8}$$

$$\vec{\nabla} \cdot \vec{H}(\vec{r},t) = 0, \tag{1.9}$$

$$\vec{\nabla} \times \vec{E}(\vec{r},t) = -\mu_r\mu_o \frac{\partial \vec{H}(\vec{r},t)}{\partial t}, \tag{1.10}$$

and

$$\vec{\nabla} \times \vec{H}(\vec{r},t) = \sigma\vec{E}(\vec{r},t) + \epsilon_r\epsilon_o \frac{\partial \vec{E}(\vec{r},t)}{\partial t}. \tag{1.11}$$

The wave nature of light is not explicitly shown in Maxwell's equations. After few lines of manipulation, it can be shown that the electric field obeys the wave equation

$$\vec{\nabla}^2\vec{E}(\vec{r},t) - \frac{\mu_r\epsilon_r}{c^2}\frac{\partial^2\vec{E}(\vec{r},t)}{\partial t^2} = \sigma\mu_0\mu_r\frac{\partial\vec{E}(\vec{r},t)}{\partial t}, \tag{1.12}$$

where $c = \frac{1}{\sqrt{\mu_o\epsilon_o}}$ is the free-space speed of light. For complex electric fields under the plane wave assumption, the general solution to the electric field is

$$\underline{\vec{E}}(\vec{r},t) = \underline{E}_0\, e^{i(\underline{\vec{k}}.\vec{r}-\omega t)}, \tag{1.13}$$

where $\underline{\vec{k}}$ is the complex wave vector.

The magnetic field wave equation can be derived using a similar approach where

$$\vec{\nabla}^2\vec{H}(\vec{r},t) - \frac{\mu_r\epsilon_r}{c^2}\frac{\partial^2\vec{H}(\vec{r},t)}{\partial t^2} = \sigma\mu_0\mu_r\frac{\partial\vec{H}(\vec{r},t)}{\partial t}. \tag{1.14}$$

1.2 Electromagnetic Wave Propagation

The propagation of electromagnetic waves through matter is governed by three parameters: the conductivity, the permittivity, and the permeability. Conductivity (σ) is the measure of material's ability to conduct electric currents and it can be approximated as a function of the current density and the applied electric field ($\vec{J}/\vec{E}$). Materials are classified based on their conductivity as metals, semiconductors or dielectrics. The conductivity of a material usually depends on temperature and frequency.

Permittivity (ϵ) is the measure of material's ability to resist an electric field. It describes how much electric flux, electric field flow through a given area, is generated per unit charge of a medium. The absolute permittivity of a medium is defined as

$$\epsilon = \epsilon_0 \epsilon_r = \epsilon_0(1 + \chi_e), \tag{1.15}$$

where ϵ_0 is the permittivity in free-space, ϵ_r is the relative permittivity of the medium, and χ_e is the electric susceptibility which indicates the degree of polarization of the electric dipoles in response to an applied electric field.

As opposed to the constant electric field response of free-space, materials are usually dispersive and their associated permittivities are dependant on the frequency of the applied electric field. The frequency dependency of permittivity indicates that the polarization response of dispersive materials to an applied field is not instantaneous. To represent this response, permittivity is defined as a complex function of the angular frequency (ω) of the applied field

$$\underline{\epsilon}(\omega) = \epsilon^{'}(\omega) + i\epsilon^{''}(\omega). \tag{1.16}$$

To simplify the atomic-scale description of permittivity in dispersive materials, a classical kinetic model has shown to provide satisfactory results. This simple model is based on describing the electromagnetic properties of a material by considering the motion of its constituent atoms, electrons and molecules using a harmonic oscillator model. In dielectrics, the total forces acting on electrons can be written as

$$F_{total} = F_{binding} + F_{damping} + F_{driving}, \tag{1.17}$$

where $F_{binding}$ is the binding forces between electrons and molecules, $F_{damping}$ is the force associated with the radiation of oscillating charges, and $F_{driving}$ is the force due to an applied electromagnetic wave.

Eliminating the contributions of the binding forces on electrons yields a very similar model that can be used for metals. This model, known as Drude model, was originated in 1900 by Paul Drude [15, 16] and described the electromagnetic properties of metals by considering a density of unbounded motion-free electrons. Under the influence of a time-varying electric field, the equation of motion of free electrons can be written as

$$q\bar{E}_0 e^{-i\omega t} = m\gamma \frac{d\bar{x}}{dt} + m\frac{d^2\bar{x}}{dt^2}, \tag{1.18}$$

where m and q are the effective mass and the charge of the electron, respectively, $\bar{x}$ is the electron displacement, and γ is the damping constant. The electron displacement is a time harmonic vector ($\bar{x} = \bar{x}_0 e^{-i\omega t}$), and Eq. 1.18

can be re-written as

$$q\bar{E}_0 = m\gamma(-i\omega\bar{x}_0) + m(-\omega^2\bar{x}_0). \tag{1.19}$$

Solving for $\bar{x}_0$, we get

$$\bar{x}_0 = \frac{-q\bar{E}_0}{m\omega(\omega + i\gamma)}. \tag{1.20}$$

Then, the electric dipole moment can be defined as

$$\bar{p} = q\bar{x}_0 = \frac{-q^2\bar{E}_0}{m\omega(\omega + i\gamma)}. \tag{1.21}$$

The polarization density, which is the density of permanent or induced electric dipole moments, is defined in general as

$$\bar{P} = N\bar{p} = \lim_{\Delta v \to 0} \frac{\sum_{n=1}^{N} Q_n d_n}{\Delta v}, \tag{1.22}$$

where d is the distance vector from negative to positive charge Q of the dipole and N is the total number of dipoles in a volume Δv. Invoking the electric dipole moment definition (Eq. 1.21), the polarization can be re-written as

$$\bar{P} = \frac{-Nq^2\bar{E}_0}{m\omega(\omega + i\gamma)}. \tag{1.23}$$

In linear, isotropic, and homogeneous media, the polarization is related to electric field by

$$\bar{P} = \epsilon_0(\epsilon_r - 1)\bar{E} = \epsilon_0\chi_e\bar{E}. \tag{1.24}$$

Solving for ϵ_r by substituting Eq. 1.23 in Eq. 1.24, we get

$$\epsilon_r = 1 - \frac{-\omega_p^2}{\omega(\omega + i\gamma)}, \tag{1.25}$$

where ω_p is the plasma frequency and it is defined as

$$\omega_p = \sqrt{\frac{-Nq^2}{m\epsilon_0}}. \tag{1.26}$$

Solving for the real and imaginary components of permittivity, we get

$$\underline{\epsilon}(\omega) = 1 - \frac{\omega_p^2}{(\omega^2 + \gamma^2)} + i\frac{\omega_p^2}{\omega\gamma(1 + \omega^2/\gamma^2)}. \tag{1.27}$$

Assuming $\gamma \simeq 0$, the permittivity can be simplified to

$$\epsilon(\omega) = 1 - \frac{\omega_p^2}{\omega^2}, \tag{1.28}$$

which will be negative when the frequency (ω) is less than the plasma frequency (ω_p), like silver and gold at visible frequencies. The plasma frequency (ω_p) and the damping constant (γ) of selected noble metals are shown in Table 1.1. A common feature of these metals is their relatively low loss, where damping constants are several orders of magnitude less than the plasma frequency. Although Drude model showed to provide fairly accurate permittivity values for metals when compared to the experimentally-measured values, its predictions are found to be limited especially for the imaginary parts of permittivity. To demonstrate such limitations, the Drude model of silver (based on the parameters in Table 1.1) is plotted against its experimental data [17] (Fig. 1.1). These discrepancies in the Drude model predictions can be attributed to the interband transitions which are not considered in the Drude model.

Table 1.1: Plasma frequency ω_p and damping constant (γ) of selected noble metals [1]

Metal	$\omega_p(\times 10^{15} Hz)$	$\gamma\ (\times 10^{12} s^{-1})$
Silver (Ag)	2.186	5.14
Gold (Au)	2.15	17.14
Copper (Cu)	2.12	23.09

Permeability (μ) is the measure of material's ability to support the magnetic field formation within itself. In other words, it is the material's degree of magnetization in response to an applied magnetic field. The absolute permeability of a medium is defined as

$$\mu = \mu_0\,\mu_r = \mu_0(1 + \chi_m), \tag{1.29}$$

where μ_0 is the permeability in free-space, μ_r is the relative permeability, and χ_m is the magnetic susceptibility which indicates whether a material is attracted into or repelled out of an external magnetic field.

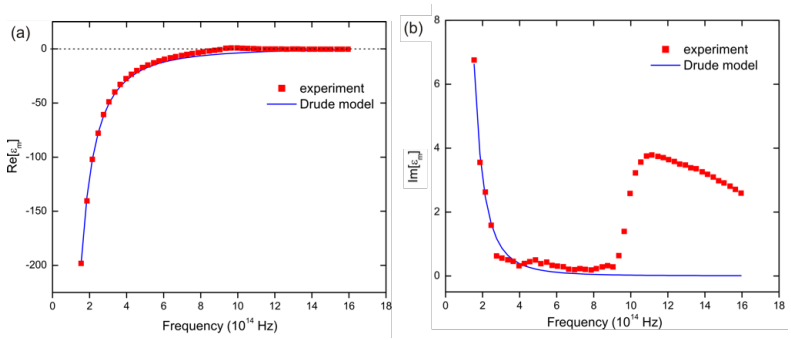

Figure 1.1: Real and imaginary components of the permittivity values of silver predicted by the Drude model (blue) and obtained from measurements (red). This Figure is published by permission from [2].

The combination of relative permittivity and permeability yields the refractive index

$$n = \sqrt{\epsilon_r \mu_r}, \tag{1.30}$$

which is a dimensionless number used in optics to describe how light propagates through different media. It determines how much light is reflected or transmitted (Fresnel equations), and the angle of refraction (Snell's law) at the interface between two media of different refractive indices. It also relates the speed and the wavelength of light in vacuum (c, λ_0) to the corresponding ones in a different medium where $v = c/n$, and $\lambda = \lambda_0/n$. For complex permittivity and permeability, the resultant refractive index will be a complex value where the sign of the refractive index can be determined according to this equation [18]

$$\underline{n} = \text{sgn}(\Re[\underline{\epsilon}]|\underline{\mu}| + \Re[\underline{\mu}]|\underline{\epsilon}|)\sqrt{\underline{\epsilon}\underline{\mu}}. \tag{1.31}$$

Across the electromagnetic parameter space where the permittivity (ϵ) is the x-axis and the permeability (μ) is the y-axis (Fig. 1.2), each quadrant represents a different set of materials based on their electromagnetic responses. Simultaneously positive ϵ and μ results in having positive refractive index and consequently positive refraction. These materials are represented by the first quadrant. At the plasma frequency which was discussed in the Drude model, the permittivity sign of metals switch from positive to negative. Negative permittivity and positive permeability materials which have complex refractive index are illustrated by the second quadrant. The

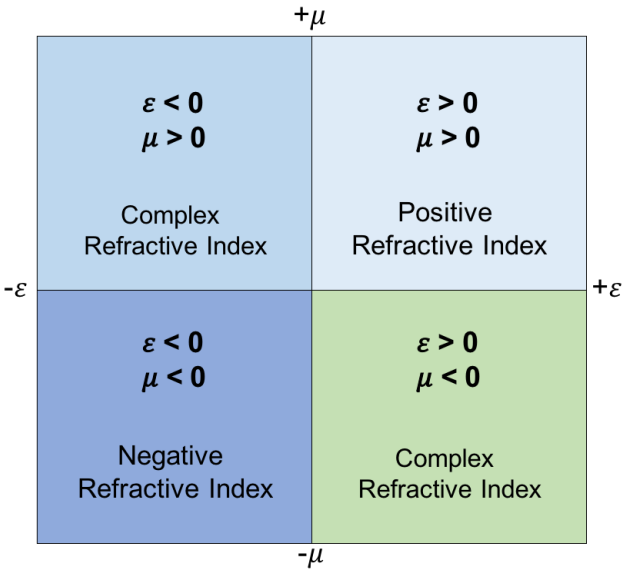

Figure 1.2: Parameter space of ϵ and μ.

plasma frequency of most metals reside over the ultraviolet and the visible part of the electromagnetic spectrum. Metals with negative permittivity can sustain an interesting phenomenon known as surface plasmon resonance (SPR). The surface plasmon resonance occurs due to the rapid oscillation of the electron densities at the surface of metals when they are exited by electromagnetic waves at their resonance frequency (Fig. 1.3). The detailed theoretical concept of SPR will be discussed in the Appendix. This phenomenon allows to store energy and also manipulate the stored energy in the form of surface waves, which has been proven to be the key ingredient for realizing unusual optical properties.

Usually natural materials have neutral magnetic responses. However, there are few materials that exhibit magnetic responses when they are exposed to electromagnetic waves as in the third quadrant ($\epsilon > 0$, $\mu < 0$). The fourth quadrant represents the most interesting and challenging case where ϵ and μ are both negative resulting in a medium with negative refractive index. In normal circumstances, most materials refract light positively (to the opposite side of normal) and support forward waves defined by right hand rule, where the phase velocity (directed along the wave vector) and the group velocity (directed along the time averaged Poynting vector) point

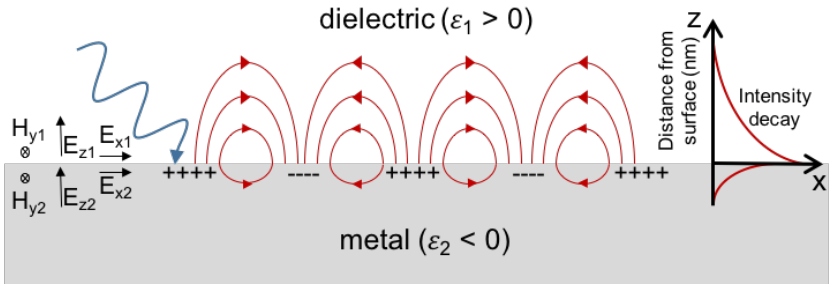

Figure 1.3: Schematic of the charge density oscillations and associated electromagnetic fields in the SPR phenomenon at the interface of a metal and dielectric.

to the same direction. In the double negative media ($\epsilon < 0$, $\mu < 0$), on the other hand, it has been shown that light can be refracted negatively (to the same side of normal) and backward waves described by left hand rule (phase velocity and group velocity pointing in opposite directions) can be sustained (Fig. 1.4). Although such media possess interesting unusual properties [19], they are not naturally available. Therefore, artificial structures known as metamaterials have been fabricated to imitate abnormal properties like double negative property.

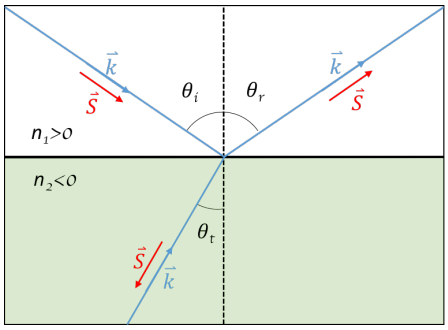

Figure 1.4: The schematic of negative refraction.

1.3 Metamaterials

Metamaterials are generally defined as materials with properties that are not achievable with natural materials. In the field of electromagnetics, metamaterials are engineered structures with inhomogeneity scale smaller than the operational wavelength (sub-wavelength). They are designed to realize electromagnetic behaviours that are not possible using bulk natural materials [20–23]. For instance, metamaterials can imitate the electromagnetic properties of the double negative media and they can be effectively characterized by negative refractive index. Some of the explored metamaterial structures in the literature are shown in Figure 1.5.

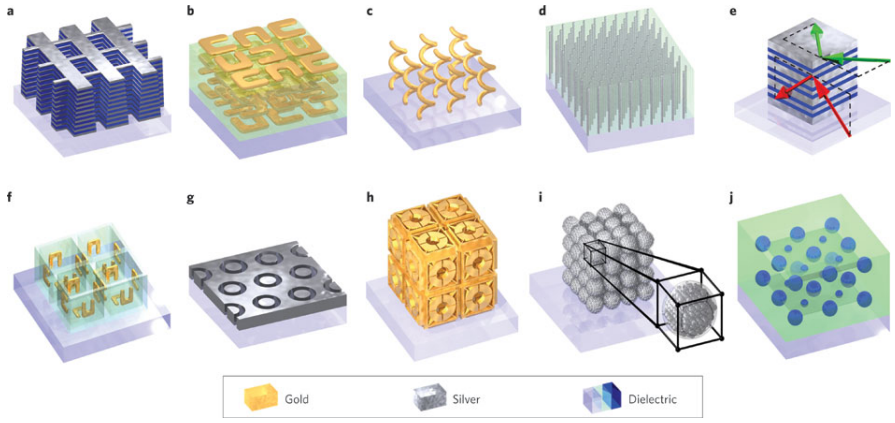

Figure 1.5: Different metamaterial structures. a) double-fishnet negative-index metamaterial with several layers, b) stereo or chiral metamaterial fabricated through stacked electron-beam lithography. c) chiral metamaterial made using direct-laser writing and electroplating, d) hyperbolic (or indefinite) metamaterial, e) metaldielectric layered metamaterial composed of coupled plasmonic waveguides, enabling angle-independent negative n for particular frequencies, f) split ring resonators oriented in all three dimensions, g) wide-angle visible negative-index metamaterial based on a coaxial design, h) connected cubic-symmetry negative-index metamaterial structure, i) metal cluster-of-clusters visible-frequency magnetic metamaterial, j) all-dielectric negative-index metamaterial composed of two sets of high-refractive-index dielectric spheres arranged on a simple-cubic lattice. This Figure is published by permission from [3]

Metamaterials were first proposed by Bose in 1898 to achieve an artificial

chiral effect [24]. However, the term metamaterial first appeared in 1999 by Rodger M. Walser [25], a physics professor from the University of Texas. Few months later, the term metamaterial became more popular through the pioneering work of Smith et al. [26] on materials with simultaneously negative permeability and permittivity at microwave frequencies.

There are three ground-breaking works that can be counted as milestones in the area of modern metamaterials. The first one is the Veselago's paper which conceptually laid down the theory of left-handed metamaterials, materials in which the wave vector $\vec{k}$ and the field vectors $\vec{E}$, $\vec{H}$ form a left-handed system [19]. The next outstanding work is the first experimental realization of Veselago's left-handed medium by Smith et al. [26]. The third exceptional work is Pendry's work on perfect lensing, perfect imaging beyond the conventional resolution limit, with a layered metamaterial composed of a single layer of silver [27]. This single layer structure represents the only route to realize artificial magnetism and left-handed behavior at visible and UV frequencies.

Based on the targeted frequency range, the size and the achievable electromagnetic properties of metamaterials can be vastly different. While the size of metamaterial structures will be centimeter-scale for microwave frequencies, their size can drop down to nanometer-scale for optical frequencies. In this thesis, we examine nano-scale metamterials that work over the ultraviolet and visible frequencies. Metals are the main building elements for making such optical metamaterials. This is due to the interesting properties associated with metals around the optical range such as negative permittivity and surface plasmon resonance. It has been shown that these properties can contribute significantly towards realizing the unusual properties of optical metamaterials [27–29].

The heterogeneity in metamaterials could be along one [7, 30, 31], two [32, 33], or three [3, 34, 35] directions (Fig. 1.6), and it could be periodic [7, 36, 37], or non-periodic [38–40]. Making optical metamaterials with nano-scale inhomogeneity requires sophisticated nano-fabrication methods. Currently, nano-fabrication methods are mainly limited to one dimensional and two dimensional fabrication techniques. Three dimensional nano-structure fabrication with heterogeneity in three directions is possible by methods like focused ion beam (FIB) and electron beam lithography (EBL). However, such 3-D fabrication methods require very delicate experimental setup and alignment, which make them quite difficult and costly [20, 41]. In this thesis, we restricted our work to the one dimensional nano-structure because it can be easily modeled, and its fabrication requires tools which are well-controllable and accessible to our research group.

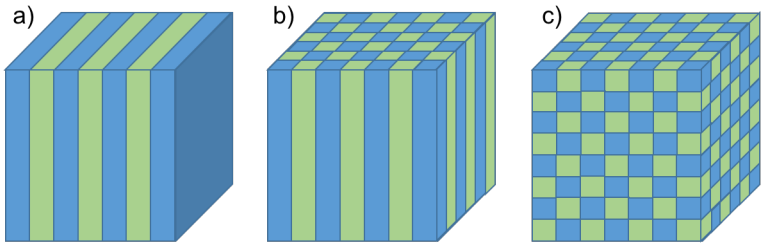

Figure 1.6: The schematic depiction of metamaterials with heterogeneity along a) one, b) two, and c) three directions.

1.4 Layered Metamaterials

Materials with sub-wavelength one-dimensional heterogeneity can be achieved by fabricating a structure made of a multitude of thin films. There is a lot of overlap between layered optical metamaterial and classical thin film structures [42]. Both systems are composed of thin films of metal and dielectric. However, the design purposes and the complexity in terms of thickness and number of layers are different. Layered optical metamaterials are usually more complex and designed to exhibit abnormal properties. Over the last two decades, a vast variety of applications for layered metamaterials have been proposed and implemented[20, 41]. In this thesis, we particularly consider flat lens imaging [27], spectral light transmission [43], and surface plasmon resonance sensing [44] applications. Here, we discuss the recent achievements in the designated research fields, and we will thoroughly examine different methods to engineer and improve the performance of these applications in the next chapters.

1.4.1 Flat Lens Imaging

Lenses are optical transmissive devices that are capable of reassembling electromagnetic fields to a focus by correcting the phase of each Fourier component of the fields. This phase correction feature is due to the curvature shapes of the entrance and exit faces of conventional glass lenses (Fig. 1.7 a)). Flat lenses, on the other hand, are perfectly flat slabs with imaging capabilities as a result of the optical properties of their material composition. Flat lenses can be made of materials with gradual variation of the refractive index (graded-index lenses) [45], or artificially structured sheet of materials with subwavelength-scaled patterns in the horizontal dimen-

sions (electromagnetic metasurfaces) [46], or ultra-thin metasurfaces with balanced loss and gain [47], or layered metamaterials [11, 13, 27, 48]. The main distinguishing feature of layered metamaterial flat lenses is their perfect homogeneity along the front and back surfaces. This implies that the imaging process is not associated with a principle optical axis which results in the abnormal possibility of imaging with an infinite aperture if we assume to have infinitely long flat lens [49].

In theory, imaging with a planar homogeneous slab (Fig. 1.7) is possible if the flat slab is constructed from either isotropic and negative index medium, first proposed by Veselago [19], or anisotropic medium with a constitutive tensor having diagonal components of opposite sign [23, 48, 49]. In the absence of naturally-occurring negative-index or anisotropic materials, a thin layer of silver (Fig. 1.7(d)) has been suggested by Pendry to work as flat lens based on the electrostatic limit approximation. Pendry's flat lens can form a real image at a distance less than a wavelength from the lens (near-field) using a transverse-magnetic (TM) polarized wave [27]. What makes Pendry's flat lens very interesting is the capability of this lens to perform super-resolution imaging. The imaging resolution of traditional glass lenses is limited by the applied wavelength since the produced images comprise only the propagating waves. This image resolution limit is known as the diffraction limit. To break this barrier and achieve super-resolution, evanescent waves, which exponentially decay, should be restored alongside propagating waves at the image location. Unlike propagating waves restoration, which is possible by phase correction, evanescent waves restoration requires amplitude amplification. Pendry showed that a solution to Maxwell's equations demonstrates that ideal negative index slabs (Veselago lens) as well as thin silver slabs can amplify evanescent waves by restoring wave amplitudes in the image region and enable super-resolution imaging. He interestingly showed that the condition required for super-resolution imaging ($\epsilon < 0$) is exactly the same condition needed for the existence of surface plasmon polaritons. This implies that these two phenomena are inherently interrelated. The mathematical proof of evanescent wave amplification using a thin layer of silver is discussed in the Appendix.

Since the first practical flat lens proposal (Pendry's thin silver layer) [27], several research works have been published investigating this phenomena both numerically [6, 9] and experimentally [10, 50]. These works include research on near-field [28] and far-field [7] flat lens imaging, where the far-field flat lens can project the image apart from the lens at a distance greater than the wavelength in the hosting medium. The introduced flat lenses are composed of a single metallic layer [9–12, 50–54] and metal-dielectric multi-

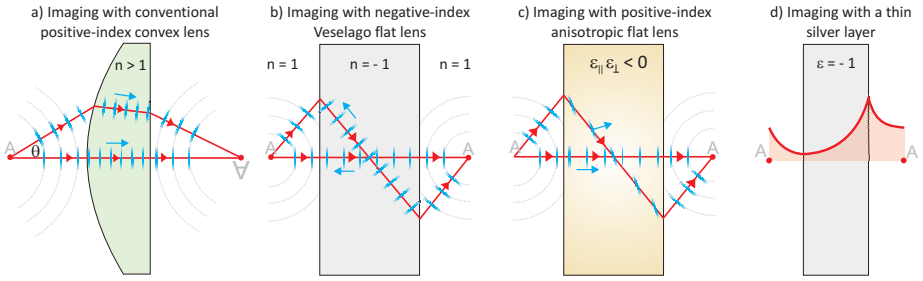

Figure 1.7: Optical ray visualization of imaging in (a) a standard plano-convex lens, (b) a planar negative-index slab, and (c) a planar anisotropic slab where the perpindicular permittivity value is negative. The red lines and blue arrows respectively indicate the local power and phase flow. (d) Imaging in a thin silver layer by evanescent wave amplification. [4]

layers [6, 7, 13, 28, 29, 55–63]. A variety of methods have been used to design these systems. Some past flat lens designs are based on imitating physical processes, such as evanescent wave amplification [10–12, 50, 54], or electromagnetic properties, such as anisotropy [6, 28, 29, 56] or negative index [7]. Some others employ transfer function calculations [57, 58, 60, 61] or simulations [13, 59, 62]. In this thesis, we postulate a new criterion to design flat lenses based on transfer function calculations and ray optics, and then we investigate the proposed criterion numerically.

1.4.2 Spectral Light Transmission

Controlling and systematically manipulating light transmission through transparent, semi-transparent, and naturally opaque lossy materials was a subject of research since the early days of science. After the revolutionary advances in science and technology over the last century, the significance of engineering light transmission became more prominent due to its high potential in various energy and optical applications. Metals are the basic building block in making layered metamaterials, flat lenses and many light-transmission-based implementations. Though metals have valuable properties such as conductivity, they are naturally opaque when they are thick and semi-transparent when they are sufficiently thin. Therefore, researchers since 1950s examined the possibility of boosting light transmission through low-loss metallic films and they reported that such a light transparency enhancement can be possible by coating the metallic film with a thin, high-

index dielectric layer [64–68].

The investigations of thin film coating led to the next research on energy-efficient heat-reflecting windows [69–73], cheap flexible transparent conductors [74–77] which are useful in making photovoltaics and displays, and nanophotonic devices such as spectrally selective transmission filters [36, 78–80], and flat lenses [6, 7, 81–83]. The applicability of the dielectric-coating method in flat lens fabrication steered our research towards several light transmission experiments that led to very interesting conclusions which will be discussed in Chapter 4.

1.4.3 Surface Plasmon Resonance Sensing

The surface plasmon resonance phenomenon is sensitive to the refractive index of the medium attached to the metal surface, which makes it appealing for a wide range of physio-chemical sensing applications [44, 84–89]. The best metals for SPR sensors are noble metals with low losses, such as silver, gold, and copper [90, 91]. Of these three, silver attains the least optical losses and the best SPR coupling [92]. Gold has an acceptable optical resonance and copper has the worst [93]. Though gold is the most expensive, gold SPR sensors are commercially preferred over silver ones due to the chemical inertness of gold [94].

To enhance SPR coupling, usually the thickness of metal or the thickness of the coating dielectric layer is optimized [95]. In more sophisticated works, silver islands were deposited on copper films [96], silver thin films are deposited on a glass substrate with some attached SiO_2 droplet residuals [97], gold nano-particles were prepared on a glass slide [98], microhole arrays with variable periodicity and diameter were fabricated [99], nano-textured metal was incorporated into the cathode structure of solar cells [100], or a polymer channel waveguide structure was coated by a passivated layer of copper [101] for the purpose of SPR enhancement.

In a different approach, depositing at various deposition rates using e-beam evaporation technique, the measured surface roughness and dielectric values of very thin Au films show that dielectric values, which play the major role in the SPR wave confinement and longer range SPR wave propagation, are dependent on their deposition rates [102]. A recent work emphasizes on the importance of deposition at the lowest possible vacuum pressure and the fastest deposition rates to avoid metal-oxide contamination [103]. Varying the deposition rate and the base vacuum pressure in the deposition chamber, they have been able to deposit high-quality plasmonic films of aluminum, copper, gold, and silver using thermal evaporation. Investigating

the influence of different deposition parameters on the SPR couplings of thin metal films, we will introduce a new deposition method using the sputter deposition in Chapter 5.

1.5 Homogenization Theory

Throughput the past years of metamaterial studies, two distinguishable research fields had the major impact on the advances in metamaterials. The first research field provided the technological platform for fabrication of complex nanostructure systems and the second approach theoretically characterized the consequences of having bulk materials with abnormal electromagnetic properties. Assigning effective material parameters to metamaterials can bridge the gap between both fields where theory can be linked to the real world implementations [104]. The process of defining the electromagnetic properties of inherently heterogeneous systems by invoking the properties of ideally homogeneous metamaterials, when the heterogeneity scales are one tenth or less than a wavelength of light, is known as homogenization.

Homogenization of artificially fabricated heterogeneous structures was a subject of research for several years and various approaches have been proposed and investigated in the literature. Mainly working with periodic systems, it has been shown that the elctromagnetic properties of the building blocks of metamaterials, the sub-wavelength periodic structures, can be homogenized to express the electromagnetic responses of the entire structure in terms of effective parameters [105].

The Nicholson-Ross-Weir (NRW) retrieval method or the scattering parameter extraction method (S-parameter) is one of the earliest and simplest effective parameter retrieval methods, where the metamaterial structure is homogenized by extracting its effective parameters from the experimentally measured external light scattering of the system [106–111]. This simple homogenization method yields an infinite branch of solutions which raises the concept of branch ambiguity as a clear disadvantage of this solution [112].

Other simple homogenization methods include assigning effective negative index parameter to a single thin layer of metal based on electrostatic approximation [27] and assigning the negative index parameter to a multi-layer metal-dielectric system based on the geometric optic visualization of light refraction and bulk propagation in the layered system [7]. These methods are based on unrealistic assumptions and are only applicable to particular layered metamaterials.

The more sophisticated homogenization methods are mainly based on

theoretical calculations and a variety of averaging techniques, such as field-averaging approaches [113–118], volumetric averaging of the local permittivity values based on the effective medium theory usually known as Maxwell-Garnett method [119–121], and averaging the energy densities [122]. The curve-fitting approach [123], and the dispersion equation method [33] have been also reported for homogenizing metamterials. These methods are not universal and they can lead to different solutions for the same heterogeneous system [124]. The detailed derivations of two common homogenization methods, the S-parameter and Maxwell-Garnett methods, are provided in the appendices.

One of the most rigorous homogenization methods is based on the Floquet-Bloch theorem, usually used in crystals, where the electromagnetic fields in a metamaterial is described by the dominant Floquet-Bloch harmonic [124–129]. Although, this method was used based on unpractical assumptions and suffers from branch ambiguities [31], we managed to circumvent the drawbacks and invoke this theorem in our work. Here, we provide a general introduction to this homogenization method and we will discuss the details of our work in the next chapter.

1.5.1 Floquet-Bloch Theory

In 1928, Felix Bloch studied the quantum mechanics of electrons in three dimensional periodic media [130] in which he unknowingly extended the one dimensional theorem of Gaston Floquet published in 1883 [131]. Bloch proved that wave functions of electrons in periodic media, e.g. crystals, are governed by a periodic envelop function multiplied by a plane wave. Interestingly, the first study of electromagnetic propagation in one dimensional periodic structures was presented by Lord Realeigh before Bloch's work in 1887, where he postulated the possibility of controlling light propagating through periodic media [132]. In 1972, Bykov proposed that periodic structures can be particularly used to control the spontaneous emission while the relation between the electromagnetic properties of periodic media and the Floquet-Bloch modes have not been addressed yet [133]. It was not until work by Pochi Yeh et. al. in 1977 that bridged the gap between classical electromagnetism and solid-state physics and showed that Floquet-Bloch method can be applied to electromagnetic waves propagating through crystals [37].

Although Floquet-Bloch's theorem is a solid state theorem for describing the energy states of electrons in natural crystals, it has been commonly used for characterizing the electromagnetic properties of artificial electro-

magnetic crystals, known as photonic crystals, since the photon behaviour in a photonic crystal is quite similar to electron and hole behaviour in an atomic lattice [134]. The term *photonic crystal* was first introduced in 1987 by Yablonovitch and John, where they expanded the concept of photonic band gaps in two and three dimensions [135, 136].

Beside photonic crystals, Floquet-Bloch's theorem has been also used to analyze the electromagnetic properties of periodic stratified metamaterials. Under the implicit assumptions of translational symmetry (infinite extent) and no loss, the discrete Floquet-Bloch modes of electromagnetic waves in periodic media were derived [37]. For lossy media, the Floquet-Bloch modes are complex-valued [137–139] and no longer discrete [125].

Periodic thin films became popular after the developments in the crystal-growing field in 1970s, especially with the advent of molecular beam technology. These fabrication methods enabled multilayer growing of very thin layers, down to 10 Å, with well-controlled periodicity [37, 140]. Periodic layered metamaterials and photonic crystals are both periodic thin films with abnormal electromagnetic properties, but they are fairly different. Photonic crystals are only made of dielectric materials with lattice periodicity comparable to the operation wavelength, while periodic layered metamaterials can be composed of metal or dielectric materials with lattice constant smaller than the wavelength. Over and above, the practical significance of photonic crystals is mainly due to their associated photonic bandgaps, frequency ranges where light cannot propagate through. This implies that the abnormal electromagnetic properties of photonic crystals can be attributed to the unusual refraction of light within their periodic lattices rather than the microscopic electromagnetic resonance effects which are associated with layered metamaterials. [134, 141, 142]

Considering a general periodic thin film system, the dielectric constant ϵ depends on the spatial coordinate $\vec{r}$ and the angular frequency ω. Since ϵ is a periodic function, Bloch's theorem will be applicable for the electromagnetic eigenmodes similar to electronic eigenstates in crystals. Hence, the eigenfunctions of electric and magnetic wave equations can be expressed as

$$\vec{E}_k(\vec{r}) = u_k(\vec{r})\, e^{i(\vec{k}.\vec{r})}, \tag{1.32}$$

$$\vec{H}_k(\vec{r}) = v_k(\vec{r})\, e^{i(\vec{k}.\vec{r})}, \tag{1.33}$$

where $u_k(\vec{r})$ and $v_k(\vec{r})$ are the periodic envelope functions of electric and magnetic fields respectively, and satisfy the following conditions:

$$u_k(\vec{r}+\vec{a}) = u_k(\vec{r}), \tag{1.34}$$

$$v_k(\vec{r}+\vec{a}) = v_k(\vec{r}), \tag{1.35}$$

where $\vec{a}$ is the elementary lattice vector and $\vec{k}$ is the Bloch wave vector. If the periodicity disappears, the periodic envelope functions $u_k(\vec{r})$ and $v_k(\vec{r})$ become constant and the Bloch wave vector equals to the wave vector of the plane wave of propagation. [140, 143]

1.6 Thesis Outline

The thesis presents rigorous electromagnetic solutions for practical implementations of layered metamaterials for the purpose of engineering their exotic electromagnetic properties. Chapter 1 discussed the fundamental concepts of the electromagnetic wave theory. We also presented some more advanced concepts like metamaterials, homogenization theory, and the Floquet-Bloch theory. Following the rapid pace of research on metamaterials, we highlighted some of the most influential research in the field of layered metamaterials focusing on three influential applications. Chapter 2 discusses the derived analytical solutions and the corresponding band diagrams as a practical design tool for engineering the refractive properties of layered metamaterials. The next three chapters then discuss three layered metamaterial applications. A flat lens criterion is proposed and validated in Chapter 3. The concept of spectral light transmission in bi-layer thin films and the general conditions for light transmission boost with a series of experimental investigations will be presented in Chapter 4. Chapter 5 discusses a new nano-film fabrication method for surface plasmon coupling enhancement. We conclude the thesis by summarizing the contributions, shedding the light on the limitations, and discussing the possible directions for future work.

Chapter 2

Electromagnetic Fields in Layered Metamaterials of Finite Extent

Layered structures are one of the simplest forms of a metamaterial, as it has heterogeneity along just one direction. Solving for the electromagnetic fields within and about a layered system is straightforward using methods like the transfer matrix method, a method used to analyze the propagation of electromagnetic waves through a stratified (layered) medium by accounting for all transmitted and reflected waves within the layers and formalizing the problem in matrix form. However, analyzing the intrinsic electromagnetic field interaction, which can provide physical insights and explain the associated abnormal optical properties such as super-resolution imaging, is fairly complex due to the contribution of surface plasmon modes in these systems. To provide a simple solution to this problem and to characterize the properties of layered metamaterials, various homogenization methods have been introduced. An overall view of these homogenization methods has been provided in the introduction, and it has been shown that they are generally either based on unpractical assumptions or encounter non-uniqueness. Even the Floquet-Bloch method, which is a widely used homogenization method in the literature, is limited to applications for lossless layered systems of infinite extent.

Numerical simulations of the electromagnetic fields can directly calculate the spatial fields and energy distributions based on Maxwell's equations. This is a commonly used approach to study light behavior in layered metamaterials [6, 9, 51]. The numerical simulation approach can be adapted to simulate the electromagnetic behaviour of any system. These simulations provide data on field and energy distributions of almost any configuration and graphically demonstrate the collective electromagnetic wave behaviour in complex structures. The major drawback of the numerical simulation methods in analyzing mutual multi-mode electromagnetic wave behaviours

is their incapability of accurately identifying the constituting modes and the influence of each mode.

As a compliment to these methods, we introduce a bottom-up approach that rigorously analyzes the intrinsic electromagnetic fields of lossy finite layered media in closed form. We start with the transfer matrix method using the fundamental Maxwell's equations with the least possible assumptions and without invoking any homogenization methods. Then, we apply Fourier transformation to find the Fourier domain representations of the transfer matrix method solutions. Through a series of mathematical manipulations, we manage to derive a field expression which is a product of three terms: a term explicitly dependent on the Floquet-Bloch modes, a term governed by reflections from the medium boundaries, and another term which is dependent on layer composition. We use the new field expression to decompose and analyze the wave function in single layer, bi-layer, and multi-layer systems.

Knowing the spatial-frequency representations of the electric and magnetic fields in a layered medium, the spectral time-average Poynting vector (the directional energy transfer rate of electromagnetic fields per unit area) and its associated equipotential contours (the real wave-vector coordinate contours at which the potential energy of the electromagnetic fields is constant) can be directly calculated. Plotting the derived equipotential contours (EPCs), we graphically describe a wide range of refractive properties associated with layered metamaterials. In this chapter, we will illustrate the EPC band diagrams of a wide range of layered metamaterials from simplest configuration of a thin silver layer to complex periodic systems composed of multi-layered unit cells. We will study some frequently reported abnormal optical properties associated with layered metamaterials such as negative phase velocity, super-resolution, canalization, and far-field imaging. We also utilize EPC band diagrams as standard gauge to validate some conventional homogenization methods.

2.1 Light Scattering at a Single Plane Boundary

We start with the simplest configuration of single interface where a plane boundary surface separating two isotropic homogeneous semi-infinite media. Assuming the boundary is at $z = 0$ and that it is infinite along positive and negative lateral directions, a plane wave is obliquely incident upon the boundary from the first medium ($z > 0$). The incident light will be partially reflected back to the first medium and partially transmitted through

the second medium ($z < 0$). The incident, reflected and transmitted wave vectors are all lie in the plane of incidence which is determined by the incident wave vector and the normal to the boundary surface (Fig. 2.1). In such configuration, the problem of solving for the reflected and the transmitted field coefficients is a boundary value problem which is solvable based on a set of constraints called boundary conditions. At $z = 0$, the boundary conditions insist on the continuity of the tangential electric ($\vec{E}$) and magnetic ($\vec{H}$) fields for all x and y.

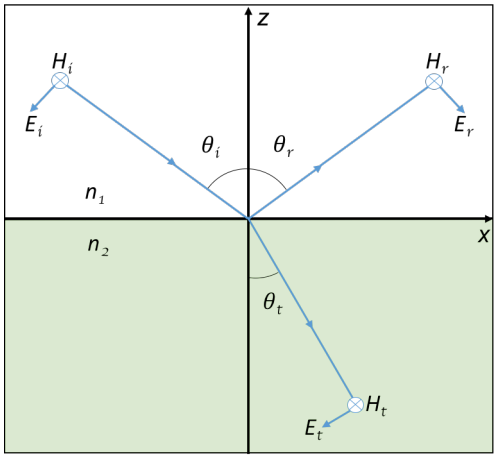

Figure 2.1: Light scattering of a TM wave at a plane boundary.

Invoking Maxwell's equations 1.10 and 1.11, we calculate the total electric and magnetic fields in the first medium as the sum of the reflected and incident components. Considering a TM-polarized plane wave incident at an angle θ from the upper semi-infinite half space onto the boundary surface, the incident time-harmonic magnetic field can be written as $\underline{\vec{H}} = H_0 e^{i(k_{x,0}x + k_{z,0}z)} e^{-i\omega t}\, \hat{y}$, where H_0 is the magnetic field amplitude, ω is the angular frequency, and the real-valued vectors $k_{x,0}$ and $k_{z,0}$ are the wave-vector components of k_0 along the x- and z-axes respectively, where $k_0 = \sqrt{k_{x,0}^2 + k_{z,0}^2}$. Solving for the fields at $t = 0$, the time-harmonic term can be suppressed and the magnetic field can be expressed as $\underline{\vec{H}} = H_0 e^{i(k_{x,0}x + k_{z,0}z)} \hat{y}$. Here, we are discussing the time-harmonic independent plane wave equations with TM polarization in frequency domain. In case of TE polarization, the principle of duality ($\underline{\vec{E}} \to -\underline{\vec{H}}$, $\underline{\vec{H}} \to \underline{\vec{E}}$, $\underline{\epsilon} \rightleftarrows \underline{\mu}$) can be applied to solve for the complimentary equations.

For a TM wave, where the magnetic field vector is normal to the plane of incidence (Fig. 2.1), the total magnetic and electric fields in the first medium can be written as

$$H_{1y} = (H_0 e^{-ik_{1z}z} + RH_0 e^{ik_{1z}z})e^{ik_x x}, \tag{2.1}$$

$$E_{1x} = \frac{-k_{1z}}{\omega\epsilon_1}(H_0 e^{-ik_{1z}z} - RH_0 e^{ik_{1z}z})e^{ik_x x}, \tag{2.2}$$

$$E_{1z} = \frac{-k_x}{\omega\epsilon_1}(H_0 e^{-ik_{1z}z} + RH_0 e^{ik_{1z}z})e^{ik_x x}, \tag{2.3}$$

where R is the reflection coefficient, and k_{1z} and ϵ_1 are the wave-vector component along z-axes and the permittivity in the first medium respectively. The opposite sign of the z component is an indication of opposite propagation in $\hat{z}$ direction. In the second medium, the electric and magnetic fields correspond only to the transmitted wave and they can be written as

$$H_{2y} = TH_0 e^{-ik_{2z}z} e^{ik_x x}, \tag{2.4}$$

$$E_{2x} = \frac{-k_{2z}}{\omega\epsilon_2} TH_0 e^{-ik_{2z}z} e^{ik_x x}, \tag{2.5}$$

$$E_{2z} = \frac{-k_x}{\omega\epsilon_2} TH_0 e^{-ik_{2z}z} e^{ik_x x}, \tag{2.6}$$

where T is the transmission coefficient of the electric field. Based on the boundary conditions of E and H fields, we can obtain the relations between reflection and transmission coefficients as

$$R + 1 = T, \tag{2.7}$$

and

$$\frac{k_{1z}}{\epsilon_1}(R - 1) = -\frac{k_{2z}}{\epsilon_2} T. \tag{2.8}$$

Solving for R and T coefficients, we get

$$R = \frac{1 - p}{1 + p}, \tag{2.9}$$

and

$$T = \frac{2}{1 + p}, \tag{2.10}$$

where $p = \frac{\epsilon_1 k_{2z}}{\epsilon_2 k_{1z}}$. For TE wave, where the electric field vector is normal to the plane of incidence, we have the same solutions for R and T coefficients where p should be replaced by $p = \frac{\mu_1 k_{2z}}{\mu_2 k_{1z}}$. The derived reflection and transmission coefficients are equivalent to the Fresnel coefficients for normal incidence.

2.2 Transfer-Matrix Representation of the Electromagnetic Field in a Layered Medium

We consider the general one-dimensional configuration of a layered periodic media bounded by two semi-infinite half spaces (Figure 2.2). The infinitely long layered system is aligned parallel to the xy plane with heterogeneity along z direction. It is composed of M repeated unit cells of J layers where the total number of layers is MJ. The layers within a unit cell are referenced by the small letter j, where $j = 1, ..., J$, and the unit cells are referenced by the small letter m, where $m = 0, ..., M-1$. Consequently, the label reference of any layer ℓ will be a function of m and j, where $\ell = mJ+j$. We label the half space before the first layer as $\ell = 0$ and the half space after the last layer as $\ell = MJ+1$. With layer thickness of d_ℓ for layer ℓ, the total thickness of the layered medium will be $L = \sum_{\ell=1}^{MJ} d_\ell$. The interface plane location between layer ℓ and $\ell+1$ is denoted by z_ℓ. Accordingly, if the plane of the first interface is at $z_0 = 0$, the plane of the last interface will be at $z_{MJ} = L$.

The associated dispersive electromagnetic properties of each layer are the complex-valued relative permittivity $\underline{\epsilon}_\ell$, the complex-valued relative permeability $\underline{\mu}_\ell$, and consequently the complex-valued refractive index $\underline{n}_\ell$. For the defined multi-layer structure where the heterogeneity is just along one direction, the electromagnetic fields in each layer are the result of the interference between the infinite reflected and transmitted waves bouncing back and forth between the two consecutive interfaces. The convenient way to account for all reflected and transmitted waves and the boundary conditions is through the matrix form representation of the aggregated reflected and transmitted coefficients. The transfer matrix representation was first introduced in optics by Jones' and Abels in 1950 [144]. Later, this method has been extensively used to solve for light propagation in stratified media [81, 119, 140, 145–149].

Here, we consider a TM-polarized plane wave incident at an angle θ from the semi-infinite left half space ($\ell = 0$) onto the layered medium. Using the transfer matrix method, the magnetic field in an arbitrary layer ℓ is the sum of two counter-propagating waves, a forward wave and a backward wave.

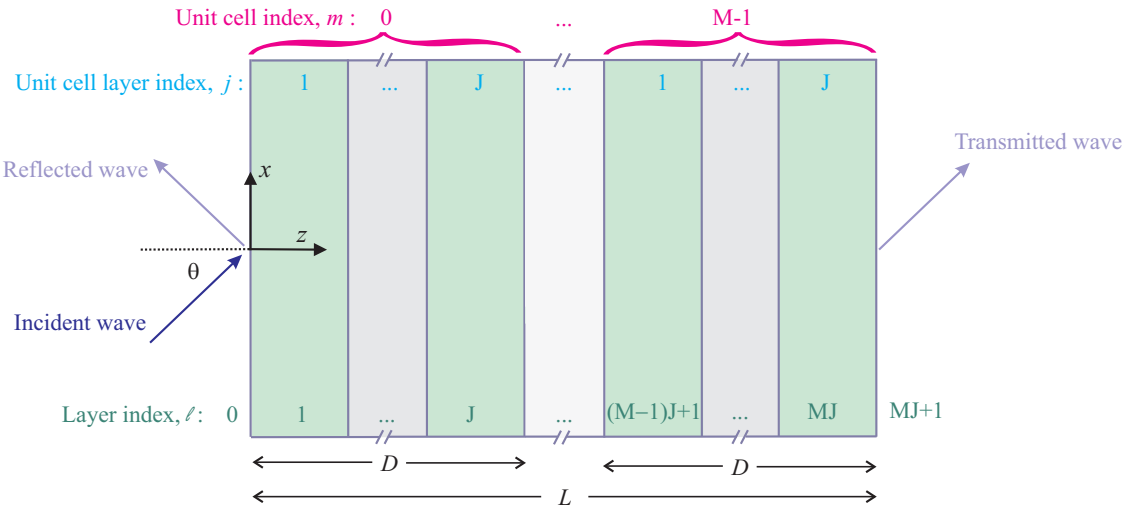

Figure 2.2: Geometry under consideration consisting of a one-dimensional periodic layered medium bounded by two semi-infinite half spaces and composed of M repeated unit cells, each consisting of J layers. The medium is excited from one half-space by an incident plane inclined at an arbitrary angle θ in the xz plane. [5]

The matrix form representation of the magnetic field in an arbitrary layer ℓ can be written as

$$\begin{aligned}\vec{\underline{H}}_\ell(x,z) &= \underline{H}_\ell(x,z)\hat{y} \\ &= e^{ik_{x,0}x}\begin{pmatrix} e^{i\underline{k}_{z,\ell}(z-z_\ell)} \\ e^{-i\underline{k}_{z,\ell}(z-z_\ell)} \end{pmatrix}^T \begin{pmatrix} \underline{A}_\ell \\ \underline{B}_\ell \end{pmatrix} \hat{y},\end{aligned} \tag{2.11}$$

where $\underline{A}_\ell$ and $\underline{B}_\ell$ are the wave coefficients of the forward and backward waves in layer ℓ. The wave-vector component $\underline{k}_{z,\ell}$ in layer ℓ can be related to the layer refractive index $\underline{n}_\ell$, and the tangential wave-vector component $k_{x,0}$ by

$$\underline{k}_{z,\ell} = \underline{n}_\ell\sqrt{k_0^2 - \left(\frac{k_{x,0}}{\underline{n}_\ell}\right)^2}. \tag{2.12}$$

Using the boundary conditions at the interfaces, the wave coefficients $\underline{A}_\ell$ and $\underline{B}_\ell$ in layer ℓ and the wave coefficients $\underline{A}_{\ell+1}$ and $\underline{B}_{\ell+1}$ in the adjacent

layer $\ell + 1$ can be related by

$$\begin{pmatrix} \underline{A}_{\ell+1} \\ \underline{B}_{\ell+1} \end{pmatrix} = \underline{\mathbf{T}}_\ell \underline{\mathbf{P}}_\ell \begin{pmatrix} \underline{A}_\ell \\ \underline{B}_\ell \end{pmatrix}, \tag{2.13}$$

where $\underline{\mathbf{P}}_\ell$ is the propagation matrix corresponding to layer ℓ, and $\underline{\mathbf{T}}_\ell$ is the transmission matrix corresponding to the interface between layer ℓ and $\ell+1$. The propagation matrix $\underline{\mathbf{P}}_\ell$ is given by

$$\underline{\mathbf{P}}_\ell = \begin{pmatrix} e^{i\underline{k}_{z,\ell} d_\ell} & 0 \\ 0 & e^{-i\underline{k}_{z,\ell} d_\ell} \end{pmatrix}, \tag{2.14}$$

and the transmission matrix $\underline{\mathbf{T}}_\ell$ is given by

$$\underline{\mathbf{T}}_\ell = \frac{1}{2} \begin{pmatrix} 1 + \underline{p}_\ell & 1 - \underline{p}_\ell \\ 1 - \underline{p}_\ell & 1 + \underline{p}_\ell \end{pmatrix}, \tag{2.15}$$

with $\underline{p}_\ell = (\underline{\epsilon}_{\ell+1} \underline{k}_{z,\ell})/(\underline{\epsilon}_\ell \underline{k}_{z,\ell+1})$. Eq. 2.13 implies that the wave coefficients within a layer can be calculated knowing the wave coefficients of the previous layer.

Wave coefficients across a single layer can be related by

$$\begin{pmatrix} \underline{t} \\ 0 \end{pmatrix} = \underline{\mathbf{T}}_1 \underline{\mathbf{P}}_1 \underline{\mathbf{T}}_0 \begin{pmatrix} 1 \\ \underline{r} \end{pmatrix}, \tag{2.16}$$

and wave coefficients across an arbitrary multi-layer system can be related by

$$\begin{pmatrix} \underline{t} \\ 0 \end{pmatrix} = \underline{\mathbf{T}}_\ell \underline{\mathbf{P}}_\ell \underline{\mathbf{T}}_{\ell-1} \cdots \underline{\mathbf{T}}_1 \underline{\mathbf{P}}_1 \underline{\mathbf{T}}_0 \begin{pmatrix} 1 \\ \underline{r} \end{pmatrix}. \tag{2.17}$$

This matrix yields two equations and two unknowns ($\underline{t}$, $\underline{r}$), since the normal wave-vector component $\underline{k}_z$, the layer thickness d, and the permittivity ϵ of each layer are known. This enable us to solve for the magnetic field $\underline{\vec{H}}_\ell$ in each layer ℓ of the layered system. The total field distribution in the spatial domain can be expressed as a piece-wise function subdivided into spatial intervals corresponding to the layer regions

$$\underline{\vec{H}}(x,z) = \underline{H}(x,z)\hat{y} = \sum_{\ell=1}^{MJ} \mathrm{rect}\left(\frac{z - z_{c,\ell}}{d_\ell}\right) \underline{H}_\ell(x,z)\hat{y}, \tag{2.18}$$

where $z_{c,\ell}$ is the location of the center of layer ℓ. The rect function is defined

as

$$\text{rect}\left(\frac{z-z_{c,\ell}}{d_\ell}\right)=\begin{cases}1 & z_{c,\ell}-d_\ell/2\leq z\leq z_{c,\ell}+d_\ell/2\\ 0 & \text{otherwise.}\end{cases}$$

Equation (2.18) works well solving for sets of linear equations using numerical routines, but there are at least two disadvantages that should be taken in consideration. First, this form of solution does not provide physical insight into the overall behavior of the repeated sets of layers. Second, the right and left-handed propagating modes cannot be distinctly identified and analyzed using this time domain solution. To account for these concerns, Fourier transformation is applied to the piece-wise wave solution in the next section.

2.3 Isolating Floquet-Bloch Modes by Fourier Transformation

We solved for the electromagnetic fields everywhere using the transfer matrix method. Since we are interested in analyzing the electromagnetic modes within the layered medium, here we apply Fourier transformation to the obtained electromagnetic solutions within the layers only. Applying Fourier transformation, the magnetic field distribution in the spatial-frequency domain will be

$$\underline{H}(\kappa_x,\kappa_z)=\int_0^{z_{MJ}}\int_{-\infty}^{\infty}\underline{H}(x,z)e^{-i\kappa_x x}e^{-i\kappa_z z}dxdz, \tag{2.19}$$

where κ_x and κ_z are the spatial-frequency variables along the respective x and z directions. Using the well-known Fourier theorems and substituting (2.18) into (2.19), the integrand yields

$$\begin{aligned}\underline{H}(\kappa_x,\kappa_z)=&(2\pi)^2\delta(\kappa_x-k_{x,0})\sum_{\ell=1}^{MJ}d_\ell\,\text{sinc}\left(\frac{\kappa_z d_\ell}{2\pi}\right)e^{-i\kappa_z z_{c,\ell}}\\ &*\begin{pmatrix}e^{-i\underline{k}_{z,\ell}z_{\ell-1}}\delta(\kappa_z-\underline{k}_{z,\ell})\\ e^{i\underline{k}_{z,\ell}z_{\ell-1}}\delta(\kappa_z+\underline{k}_{z,\ell})\end{pmatrix}^T\begin{pmatrix}\underline{A}_\ell\\ \underline{B}_\ell\end{pmatrix},\end{aligned} \tag{2.20}$$

where δ is the Dirac delta function, the symbol $*$ indicates having a convolution, and the matrix superscript T denotes matrix transposition.

To produce a physically insightful Fourier-domain wave solution, we apply a series of mathematical manipulations to Equation (2.20). We start by

re-writing Equation (2.20) as a nested double summation over the number of layers in a unit cell and the number of unit cells in the layered system

$$\begin{aligned}\underline{H}(\kappa_x,\kappa_z) = (2\pi)^2\delta(\kappa_x-k_{x,0})\sum_{m=0}^{M-1}\sum_{j=1}^{J} d_j\,\mathrm{sinc}\left(\frac{\kappa_z d_j}{2\pi}\right)e^{-i\kappa_z z_{c,mJ+j}} \\ * \begin{pmatrix} e^{-i\underline{k}_{z,j}z_{mJ+j-1}}\delta(\kappa_z-\underline{k}_{z,j}) \\ e^{i\underline{k}_{z,j}z_{mJ+j-1}}\delta(\kappa_z+\underline{k}_{z,j})\end{pmatrix}^T \begin{pmatrix}\underline{A}_{mJ+j}\\ \underline{B}_{mJ+j}\end{pmatrix}.\end{aligned} \tag{2.21}$$

In equation (2.21), we substitute the variables d_ℓ with d_j, and $\underline{k}_{z,\ell}$ with $\underline{k}_{z,j}$, and replace the index ℓ by $mJ+j$. Solving the convolution yields

$$\begin{aligned}\underline{H}(\kappa_x,\kappa_z) =&(2\pi)^2\delta(\kappa_x-k_{x,0})\sum_{m=0}^{M-1}\sum_{j=1}^{J} d_j e^{-i\kappa_z z_{c,mJ+j}} \\ &\begin{pmatrix} e^{i\underline{k}_{z,j}d_j/2}\,\mathrm{sinc}[(\kappa_z-\underline{k}_{z,j})d_j/2\pi] \\ e^{-i\underline{k}_{z,j}d_j/2}\,\mathrm{sinc}[(\kappa_z+\underline{k}_{z,j})d_j/2\pi]\end{pmatrix}^T \begin{pmatrix}\underline{A}_{mJ+j}\\ \underline{B}_{mJ+j}\end{pmatrix},\end{aligned} \tag{2.22}$$

where $z_{c,mJ+j} - z_{mJ+j-1} = d_j/2$. If the discrete summation form for the central position within the layer $mJ+j$ is given by

$$z_{c,mJ+j} = mD + z_{j-1} + d_j/2, \tag{2.23}$$

where $D = \sum_{j=1}^{J} d_j$ is the thickness of the unit cell and z_{j-1} is the position of the interface between layer $j-1$ and j within unit cell $m=0$, Equation (2.22) can be simplified as

$$\begin{aligned}\underline{H}(\kappa_x,\kappa_z) = (2\pi)^2\delta(\kappa_x-k_{x,0})\sum_{j=1}^{J} d_j e^{-i\kappa_z z_{j-1}} \\ \begin{pmatrix} e^{-i(\kappa_z-\underline{k}_{z,j})d_j/2}\,\mathrm{sinc}[(\kappa_z-\underline{k}_{z,j})d_j/2\pi] \\ e^{-i(\kappa_z+\underline{k}_{z,j})d_j/2}\,\mathrm{sinc}[(\kappa_z+\underline{k}_{z,j})d_j/2\pi]\end{pmatrix}^T \\ \sum_{m=0}^{M-1} e^{-i\kappa_z mD}\begin{pmatrix}\underline{A}_{mJ+j}\\ \underline{B}_{mJ+j}\end{pmatrix}.\end{aligned} \tag{2.24}$$

The spatial-frequency domain representation of the electromagnetic wave solution in (2.24) provides little more physical insight over the spatial-domain representation of the wave solution in (2.18). However, we can further factorize and simplify the wave solution (2.24) knowing that the ma-

trix relation between the wave coefficients in an arbitrary unit cell ($\underline{A}_{mJ+j}$, $\underline{B}_{mJ+j}$), and the wave coefficients in the first unit cell ($\underline{A}_j$, $\underline{B}_j$) is given by

$$\begin{pmatrix} \underline{A}_{mJ+j} \\ \underline{B}_{mJ+j} \end{pmatrix} = \underline{U}_j^m \begin{pmatrix} \underline{A}_j \\ \underline{B}_j \end{pmatrix}, \tag{2.25}$$

where $\underline{U}_j^m$ is the unit cell transfer matrix from layer j to $mJ + j$ and is determined from the transmission and propagation matrices by

$$\underline{U}_j^m = \prod_{q=j}^{mJ+j-1} \underline{T}_q \underline{P}_q. \tag{2.26}$$

Substituting (2.25) into (2.24), we get the wave solution in terms of $\underline{A}_j$ and $\underline{B}_j$ wave coefficients

$$\begin{aligned} \underline{H}(\kappa_x, \kappa_z) = (2\pi)^2 \delta(\kappa_x - k_{x,0}) \sum_{j=1}^{J} d_j e^{-i\kappa_z z_{j-1}} \\ \begin{pmatrix} e^{-i(\kappa_z - \underline{k}_{z,j})d_j/2} \operatorname{sinc}[(\kappa_z - \underline{k}_{z,j})d_j/2\pi] \\ e^{-i(\kappa_z + \underline{k}_{z,j})d_j/2} \operatorname{sinc}[(\kappa_z + \underline{k}_{z,j})d_j/2\pi] \end{pmatrix}^T \\ \left(\sum_{m=0}^{M-1} \left(e^{-i\kappa_z D} \underline{U}_j \right)^m \right) \begin{pmatrix} \underline{A}_j \\ \underline{B}_j \end{pmatrix}. \end{aligned} \tag{2.27}$$

By matrix decomposition, the unit cell transfer matrix referenced from layer 1, $\underline{U}_1$, will be

$$\underline{U}_1 = \underline{Q}\, \underline{\lambda}\, \underline{Q}^{-1} \tag{2.28}$$

where $\underline{Q}$ is the eigenvector of $\underline{U}_1$ and $\underline{\lambda}$ is the eigenvalue of $\underline{U}_1$ whose diagonal elements are the corresponding eigenvalues $\underline{\lambda}_1$ and $\underline{\lambda}_2$. $\underline{U}_1$ can be related to the referenced unit cell transfer matrix from layer j, $\underline{U}_j$, using the relation

$$\begin{aligned} \underline{U}_j^m &= \underline{W}_{j,1}\, \underline{U}_1^m\, \underline{W}_{j,1}^{-1} \\ &= \underline{W}_{j,1}\, \underline{Q}\, \underline{\lambda}\, \underline{Q}^{-1}\, \underline{W}_{j,1}^{-1}. \end{aligned} \tag{2.29}$$

Since the determinant of $\underline{U}_1$ is unity, the eigenvalues are inverses of each other, $\underline{\lambda}_2 = 1/\underline{\lambda}_1$. These eigenvalues can be related to the Floquet-Bloch mode, $\underline{k}_{FB}$, by

$$\underline{\lambda} = \begin{pmatrix} \underline{\lambda}_1 & 0 \\ 0 & \underline{\lambda}_2 \end{pmatrix} = \begin{pmatrix} e^{+i\underline{k}_{FB}D} & 0 \\ 0 & e^{-i\underline{k}_{FB}D} \end{pmatrix}. \tag{2.30}$$

Substituting (2.29) into (2.27) and relating the wave coefficients in layer j to the wave coefficients in the left half space, we arrive at the final form of the magnetic field solution

$$\begin{aligned} \underline{H}(\kappa_x, \kappa_z) =& (2\pi)^2 \delta(\kappa_x - k_{x,0}) \\ & \underbrace{\sum_{j=1}^{J} d_j e^{-i\kappa_z z_{j-1}} \begin{pmatrix} e^{-i(\kappa_z - \underline{k}_{z,j})d_j/2} \operatorname{sinc}[(\kappa_z - \underline{k}_{z,j})d_j/2\pi] \\ e^{-i(\kappa_z + \underline{k}_{z,j})d_j/2} \operatorname{sinc}[(\kappa_z + \underline{k}_{z,j})d_j/2\pi] \end{pmatrix}^T \underline{W}_{j,1}\underline{Q}}_{\underline{L}_j} \\ & \underbrace{\sum_{m=0}^{M-1} \left(e^{-i\kappa_z D}\underline{\lambda}\right)^m}_{\underline{FB}} \underbrace{\underline{Q}^{-1}\underline{\mathbf{T}}_0 \begin{pmatrix} 1 \\ \underline{r} \end{pmatrix}}_{\underline{C}}, \end{aligned} \tag{2.31}$$

where three distinctive matrix factors are highlighted - a layer matrix $\underline{L}_j$ dependent on the thickness and wave vector in the jth layer of the unit cell, a Floquet-Bloch matrix $\underline{FB}$ dependent on the eigenvalues of the unit cell, and a weighting matrix $\underline{C}$ dependent on the reflection coefficient.

Deriving the factorized form of the magnetic field solution in equation (2.31) is the major contribution of this work. It shows how the Floquet-Bloch modes and the electromagnetic field in a lossy layered medium of finite extent are inherently related. If the general magnetic field form (2.31), the three factors can be simply re-written as

$$\underline{L}_j = \begin{pmatrix} \underline{L}_j^+ & \underline{L}_j^- \end{pmatrix}, \; \underline{FB} = \begin{pmatrix} \underline{FB}^+ & 0 \\ 0 & \underline{FB}^- \end{pmatrix}, \; \underline{C} = \begin{pmatrix} \underline{C}^+ \\ \underline{C}^- \end{pmatrix}, \tag{2.32}$$

where the "forward" and "backward" elements of each matrix factor are distinguished by the superscript "+" and "−", respectively, the magnetic

field solution can be written in a compact form as

$$\begin{aligned}\underline{H}(\kappa_x,\kappa_z) &= (2\pi)^2\delta(\kappa_x-k_{x,0})\sum_{j=1}^{J}\underline{L}_j\,\underline{FB}\,\underline{C}\\ &= (2\pi)^2\delta(\kappa_x-k_{x,0})\sum_{j=1}^{J}\begin{pmatrix}\underline{L}_j^+\\ \underline{L}_j^-\end{pmatrix}^T\begin{pmatrix}\underline{FB}^+\underline{C}^+\\ \underline{FB}^-\underline{C}^-\end{pmatrix}.\end{aligned} \tag{2.33}$$

Compared to the spatial-domain solution in (2.18), which does not include any clue to the Floquet-Bloch modes, the spatial-frequency domain solution in (2.31) can distinctively describe the collective wave behavior across repeated sets of unit cells through the elements of the Floquet-Bloch matrix. For a medium of finite extent ($M<\infty$), the $\underline{FB}$ matrix elements are given by

$$\begin{aligned}\underline{FB}^{\pm} =& e^{-i(\kappa_z\pm\underline{k}_{FB})\frac{M-1}{2}D}M\Delta_{\frac{2\pi}{D}}[\kappa_z\pm\Re(\underline{k}_{FB})]\\ &*\operatorname{sinc}\left(\frac{M[\kappa_z\pm i\Im(\underline{k}_{FB})]D/2}{2\pi}\right),\end{aligned} \tag{2.34}$$

where $\Im(\underline{k}_{FB})$ is the material loss, $\pm\Re(\underline{k}_{FB})$ is the principal harmonic center, and the Dirac comb $\Delta_{\frac{2\pi}{D}}[\kappa_z\pm\Re(\underline{k}_{FB})]$ is describing an infinite comb of discrete spatial-frequency harmonics spaced by $2\pi/D$ and it is defined as

$$\Delta_{\frac{2\pi}{D}}[\kappa_z\pm\Re(\underline{k}_{FB})]=\sum_{N=-\infty}^{\infty}\delta\left[\kappa_z-2\pi N/D\pm\Re(\underline{k}_{FB})\right]. \tag{2.35}$$

In equation 2.34, the principal Floquet-Bloch harmonics of the forward element $\underline{FB}^+$ and the backward element $\underline{FB}^-$ are centered at $\Re(\underline{k}_{FB})$ and $-\Re(\underline{k}_{FB})$, respectively. Due to the convolution of the Dirac comb and the sinc function, the harmonic elements $\underline{FB}^{\pm}$ are widened through the combined effects of finite extent ($M<\infty$) and material loss ($\Im(\underline{k}_{FB})\neq 0$).

For a medium of infinite extent ($M\to\infty$), the elements of the $\underline{FB}$ matrix approach

$$\lim_{M\to\infty}\underline{FB}^{\pm}=\begin{cases}M\Delta_{\frac{2\pi}{D}}(\kappa_z\pm\Re(\underline{k}_{FB})) & \Im(\underline{k}_{FB})=0\\ \Delta_{\frac{2\pi}{D}}[\kappa_z\pm\Re(\underline{k}_{FB})]*\frac{2}{D\sqrt{\kappa_z^2+\Im(\underline{k}_{FB})^2}} & \Im(\underline{k}_{FB})\neq 0.\end{cases} \tag{2.36}$$

In the case of lossless materials ($\Im(\underline{k}_{FB})=0$), the $\underline{FB}^{\pm}$ elements are discrete spectra with peaks at harmonics of $\pm\Re(\underline{k}_{FB})$. The resulting magnetic field

solution will be equivalent to the classical Floquet-Bloch solution where the field solution consists of discrete forward and backward Floquet-Bloch modes with amplitudes that can be explicitly determined by $(2\pi)^2 \sum_{j=1}^{J} \underline{L}_j^+ \underline{C}^+$ and $(2\pi)^2 \sum_{j=1}^{J} \underline{L}_j^- \underline{C}^-$, respectively. In the case of lossy materials ($\Im(\underline{k}_{FB}) \neq 0$), the $\underline{FB}^{\pm}$ elements are continuous spectra with peaks centered about the principal harmonics of $\pm\Re(\underline{k}_{FB})$ and broadened due to the effect of $\Im(\underline{k}_{FB})$.

2.4 Analysis of Electromagnetic Fields in Layered Metamaterials

We study the electromagnetic fields in a typical metal-dielectric layered metamaterial structure illuminated by a normal-incidence TM-polarized plane wave ($k_{x,0} = 0$). For a bi-layer unit cell system, the factorized Fourier-domain magnetic field solution takes the form

$$\underline{H}(\kappa_z) = (2\pi)^2 \delta(\kappa_x - k_{x,0}) \begin{pmatrix} \underline{L}_1^+ + \underline{L}_2^+ \\ \underline{L}_1^- + \underline{L}_2^- \end{pmatrix}^T \begin{pmatrix} \underline{FB}^+ \underline{C}^+ \\ \underline{FB}^- \underline{C}^- \end{pmatrix}, \tag{2.37}$$

where $\underline{L}_1^+$, $\underline{L}_2^+$ and $\underline{L}_1^-$, $\underline{L}_2^-$ are the forward and backward elements of layer matrices, respectively. Applying the Fourier-domain solution in (2.37) to analyze a practical design of layered metamaterial, we assume the layered system is bounded by free-space and the bi-layer unit cell consists of a 30-nm-thick Ag layer and a 30-nm-thick TiO_2 layer. A layered combination of these two materials has been modeled as a homogeneous left-handed medium [7]. We analyzed two distinct Ag-TiO_2 bi-layer systems, a system composed of two unit cells ($M = 2$) and another composed of ten unit cells ($M = 10$). Exciting each system by a plane wave with the free-space wavelength of $\lambda_0 = 365\,\text{nm}$, Ag is assigned the complex refractive index of $0.076 + 1.605i$ (interpolated from experimental data [17]), and TiO_2 is assigned the real refractive index of 2.80 [7].

For the unit cell cases $M = 2$ and $M = 10$, the matrix elements of the magnetic field solution and its modulus squared, besides the z-component of the time-averaged spectral Poynting vector are highlighted in Figure 2.3. The concourse of broad spectral envelopes defined by $\underline{L}_1^{\pm}$ (Ag layer) and $\underline{L}_2^{\pm}$ (TiO_2 layer), and finer spectral combs defined by $\underline{FB}^+ \underline{C}^+$ and $\underline{FB}^- \underline{C}^-$ results in the magnetic field spectrum. The Floquet-Bloch mode of the unit cell is $\underline{k}_{FB} = 32.5 + 0.4i\,\mu\text{m}^{-1}$, corresponding to a Floquet-Bloch refractive index $\underline{n}_{FB} = 1.89 + 0.02i$. In Figure 2.3 c) and f), $\underline{FB}^+ \underline{C}^+$ and $\underline{FB}^- \underline{C}^-$ combs are offset; the former with a principal peak located at $\Re(\underline{k}_{FB})$ and

the latter with a principal peak located at $-\Re(\underline{k}_{FB})$. Increasing number of unit cells M from 2 to 10 narrows the peaks of the combs and consequently narrows the peaks in the magnetic field spectrum. As a result, we will have better defined wavevectors for additional number of unit cells.

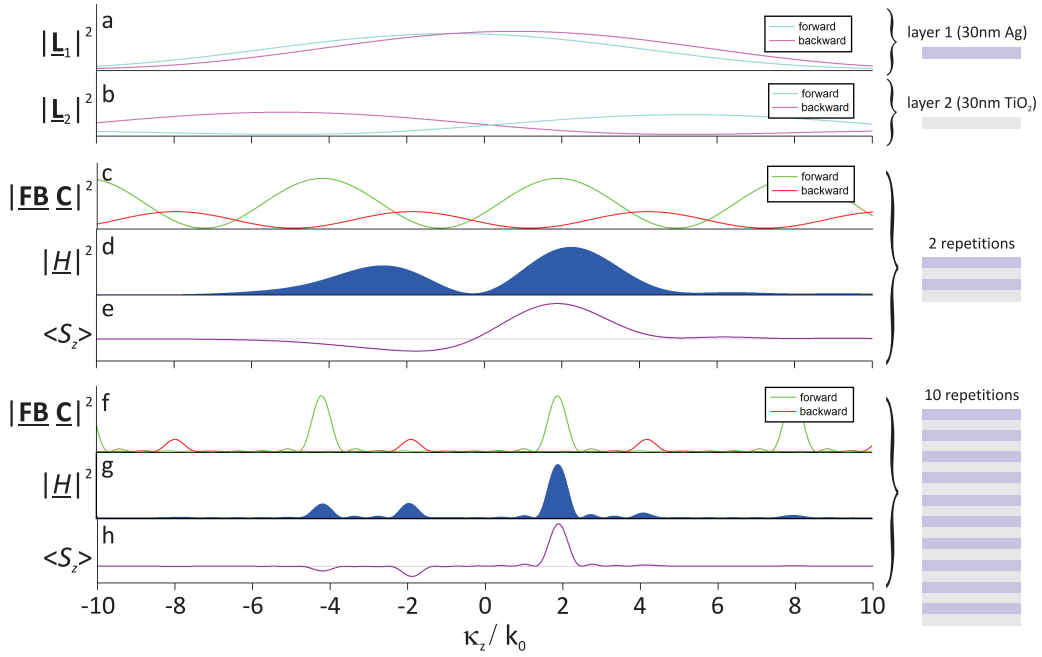

Figure 2.3: Decomposition of the wave solution in a metal-dielectric bi-layer system consisting of alternating layers of 30- nm-thick Ag and 30- nm-thick TiO_2, assuming a normally incident TM-polarized wave with a free-space wavelength of $\lambda_0 = 365\,\text{nm}$. a) The forward and backward components of the layer matrix $|\underline{\mathbf{L}}_1|^2$ corresponding to the 30- nm-thick Ag layer. b) The forward and backward components of the layer matrix $|\underline{\mathbf{L}}_2|^2$ corresponding to the 30- nm-thick TiO_2 layer. c), d), and e) depict the forward and backward components of $|\underline{FB}\,\underline{C}|^2$, the magnetic field spectrum $|\underline{H}|^2$, and the z-component of the time-averaged spectral Poynting vector, respectively, for the case of 2 unit cells; f), g), and h) depict the same set of information for the case of 10 unit cells. The horizontal gray lines in e) and h) correspond to zero values of the spectral Poynting vector . [5]

Comparing the forward and backward magnitudes of $\underline{FB}$ for the $M = 2$

and $M = 10$ cases, it can be noticed that the magnitude of $\underline{FB}^{+}\ \underline{C}^{+}$ is larger than that of $\underline{FB}^{-}\ \underline{C}^{-}$ in both cases. This indicates that the forward propagating components in the medium outweigh the backward propagating components. Carefully considering the z-component of the time-averaged spectral Poynting vector $< S_z >$ shown in Figure 2.3 e) and h), it is remarkable that these negative spatial-frequency components are forward-propagating waves since they are characterized by a negative time-averaged spectral Poynting vector. Plotting the forward and backward components of the weighting matrix $|\underline{C}|^2$ versus the number of repetitions in Figure 2.4, we show that forward propagating waves $|\underline{C}^{+}|^2$ generally exceeds backward propagating waves $|\underline{C}^{-}|^2$ and as the number of repetitions increases the backward component gradually approaching zero. To achieve negative refraction, the system should support backward waves. Figure 2.4 shows that the examined layered system is mainly supporting forward waves which means most of the waves will be refracted positively.

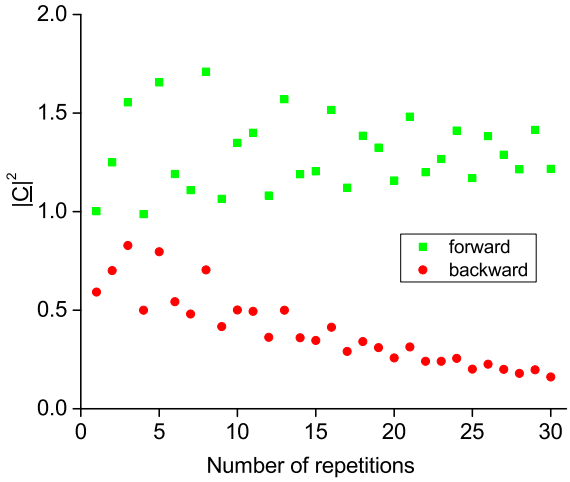

Figure 2.4: Forward and backward components of the weighting matrix $|\underline{C}|^2$ versus the number of repetitions. Here, we have assumed a metal-dielectric bi-layer system with a unit-cell made from a 30- nm-thick Ag layer and 30-nm-thick TiO_2 layer, assuming a normally incident TM-polarized wave with a free-space wavelength of $\lambda_0 = 365\,\text{nm}$. [5]

At frequencies near the bulk plasma frequency of metal, the real parts

of the Floquet-Bloch refractive index in finely layered structures composed of metal turn to be negative, particularly for TM-polarized illumination [7, 150]. Mimicking the refractive properties associated with negative-index media, these finely layered media are shown to be capable of imaging with a planar slab (flat lensing) [4, 7]. As a continuation of this work, different metamaterial configurations composed of right-handed materials have been analyzed and the right-handedness of these systems has been consistently observed, where the positive and negative spatial-frequency components of the wave are found to be both forward-propagating waves [151].

2.5 Elecromagnetic Field Band Diagrams in Layered Metamaterials

Band diagrams are necessary for illustrating refractive properties. They are usually obtained by leveraging the Floquet-Bloch theorem [130, 131] to isolate discrete sets of real-valued wave vectors $\vec{k}$ and then use a linear eigenvalue equation derived from the Helmholtz equation [143] to solve for the corresponding frequencies $\omega(\vec{k})$. To provide graphical information on phase and group velocity in the medium, equi-frequency contours (EFCs) are then displayed as a function of real-valued wave-vector coordinates. This way of solving for band diagrams is usually applied to photonic crystals and it is based on Floquet-Bloch theorem and Helmholtz equation. However, the application of Floquet-Bloch theorem is limited to lossless infinite systems, and in case of dispersion the Helmholtz equation turns into a non-linear eigenvalue equation, which requires time-consuming iterative algorithms that are sensitive to initial guesses. As a result, EFC band diagrams are rarely used to describe the electromagnetic properties of layered metamaterials [152]. Recently, a finite-element method has been proposed to solve for complex-valued wave vectors $\underline{\vec{k}}$ as a function of frequency $\omega(\underline{\vec{k}})$ in order to derive band diagrams for layered metamaterials [138, 139, 152, 153].

In this thesis, we present a new approach to obtain band diagrams for any layered metamaterial. Using the derived spatial Fourier magnetic field in Eq. 2.33, we solve for the corresponding x and z electric field components. The factorized Fourier-domain electric field components can be consequently written as

$$\underline{E}_x(\kappa_x, \kappa_z) = (2\pi)^2 \delta(\kappa_x - k_{x,0}) \sum_{j=1}^{J} \frac{1}{\underline{\epsilon}_j \epsilon_0 \omega} \begin{pmatrix} \underline{k}_{z,j} \\ -\underline{k}_{z,j} \end{pmatrix} \underline{L}_j \, \underline{FB} \, \underline{C} \qquad (2.38)$$

and

$$\underline{E}_z(\kappa_x, \kappa_z) = (2\pi)^2 \delta(\kappa_x - k_{x,0}) \sum_{j=1}^{J} \frac{1}{\underline{\epsilon}_j \epsilon_0 \omega} \begin{pmatrix} k_{x,0} \\ -k_{x,0} \end{pmatrix} \underline{L}_j \, \underline{FB} \, \underline{C}, \tag{2.39}$$

respectively. The spectral electric fields, as well as magnetic fields, are defined as functions of k_z, the spatial frequency along z, which exist for a fixed k_x. Varying θ results in sweeping over different values of k_x and consequently having a two-dimensional k-space distributions of the electric $\underline{\vec{E}}(\vec{k})$ and magnetic $\underline{\vec{H}}(\vec{k})$ fields as a function of the spatial-frequency variable $\vec{k} = k_x\hat{x} + k_z\hat{z}$.

The electric and magnetic field distributions define a plane-wave completely described by the triad $\vec{k}$-$\underline{\vec{E}}(\vec{k})$-$\underline{\vec{H}}(\vec{k})$ [154–156]. For each plane wave component, the time-averaged power flow is given by the spectral Poynting vector

$$\langle \underline{\vec{S}}(\kappa_x, \kappa_z) \rangle = \frac{1}{2} \Re \left[\underline{\vec{E}}(\kappa_x, \kappa_z) \times \underline{\vec{H}}^*(\kappa_x, \kappa_z) \right]. \tag{2.40}$$

The scalar potential of the spectral Poynting vector is defined by

$$\Phi(\vec{k}) = \frac{1}{4\pi} \int \frac{\nabla_{\vec{k}'} \cdot \langle \underline{\vec{S}}(\vec{k}') \rangle d\vec{k}'}{|\vec{k} - \vec{k}'|}. \tag{2.41}$$

Describing scalar potential as contour lines will form a diagram of bands in k-space. In general, the spectral Poynting vector can be defined as

$$\langle \underline{\vec{S}}(\vec{k}) \rangle = \nabla\Phi + \nabla \times \vec{R}. \tag{2.42}$$

where $\vec{R}$ is the rotational component of the spectral Poynting vector. Based on our observations working with layered systems, we found that solenoidal components of $\langle \underline{\vec{S}}(\vec{k}) \rangle$ are negligible. In this case the second term of Eq. 2.42 will be almost zero ($\nabla \times \vec{R} \approx 0$) and the direction of the spectral Poynting vector will be the gradient of the scalar potential (contour lines).

Based on the fundamental relationship of group velocity [157, 158]

$$\vec{v}_g = \frac{\langle \underline{\vec{S}}(\vec{k}) \rangle}{\langle U(\vec{k}) \rangle}, \tag{2.43}$$

the spectral Poynting vector have the same direction of the group velocity. Here, $\langle U(\vec{k}) \rangle$ is the time-averaged energy density which is the amount of

energy stored in the system per unit volume and it is generally defined by

$$\langle U(\vec{k})\rangle = \frac{1}{2}(\epsilon|E(\vec{k})|^2 + \mu|H(\vec{k})|^2). \tag{2.44}$$

It can be noticed that the conventional EFC band diagrams defined by frequency $\omega(\vec{k})$ are similar to the EPC band diagrams defined by $\Phi(\vec{k})$ since both have gradients along the group velocity pointing to the direction of the time-averaged power flow. However, EPC band diagrams are unique for several reasons. First, like the optical density of states, the k-space energy density distribution can be inferred from the density of EPCs, where a high EPC density indicates high energy density. Second, unlike the EFCs which are limited to the Floquet-Bloch theorem assumptions of periodic, lossless, and infinite media, EPCs are applicable to any layered system since they can be derived without invoking the Floquet-Bloch theorem.

Third, as opposed to discrete modes with complex wave vectors for lossy materials, the material loss effect using EPCs can be captured by a continuum of plane-wave modes with real wave vectors endorsing EPCs to be plotted as a function of real wave-vector coordinates. Here we have to acknowledge that the presented EPC approach builds on the past studies of the anomalous refraction in infinite, lossless photonic crystals [154–156]. These efforts are based on spatial-frequency decomposition of electric and magnetic fields to examine phase and group velocity. In this work, we have generalized the theory by incorporating finite, lossy media and introducing a new method to extract EPCs.

To demonstrate the refraction consistency of the derived EPCs with geometric optics, we examine a positive and a negative index homogeneous, isotropic slabs, whose interface are aligned along the z plane. For homogeneous slabs, the EPCs are semi-circular bands as shown in Figs. 2.5 (a) and (b). When the slabs are lossless and infinite, the EPC bands collapse to a semi-circular line emulating the plane-wave mode in a homogeneous medium ($\omega = ck/n$). The homogeneous, lossy and finite slab is illuminated by an obliquely incident plane wave from free-space at an angle θ where the plane wave can be described in k-space by a wave-vector $\vec{k}_0 = k_{x,0}\hat{x} + k_{z,0}\hat{z}$. The wave vector component parallel to the interface ($k_{x,0}$), visualized by the vertical lines in Figs. 2.5 (a) and (b), is conserved based on the principal of tangential field continuity.

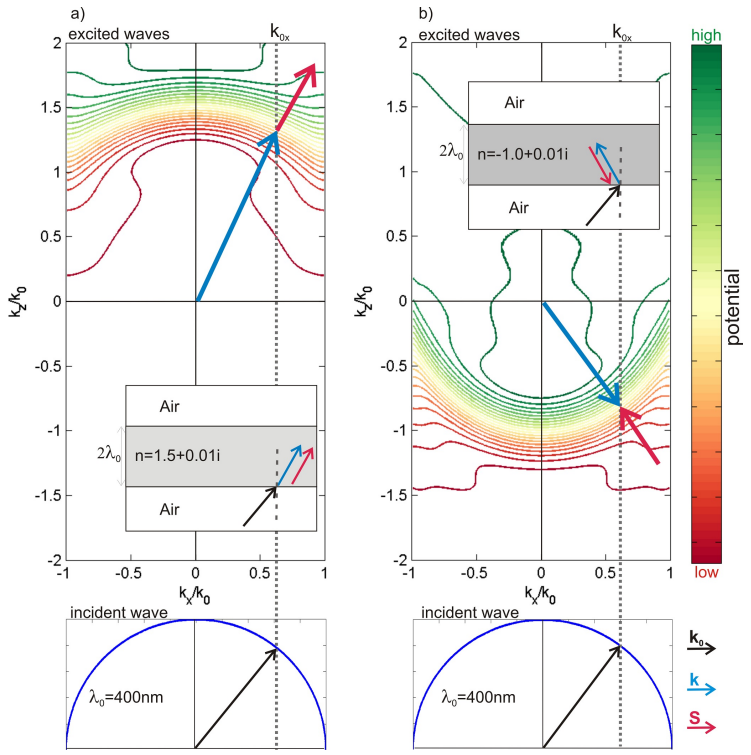

Figure 2.5: Light refraction at an interface described by EPCs. EPCs for finite, lossy slabs of thickness $2\lambda_0$ having either (a) a positive refractive index $\underline{n} = 1.5 + 0.1i$ or (b) a negative refractive index $\underline{n} = -1 + 0.1i$. The bottom panels depict the EPCs of an incident plane wave ($\lambda_0 = 400$ nm) impinging on the slab. The resulting phase (blue arrow) and time-averaged Poynting vector (red arrow) are graphically derived in k-space from the EPCs and then depicted in real-space in the insets. [8]

For the positive-index slab, the excited plane waves have parallel phase and group velocities along a direction consistent with Snell's law. For the negative-index slab, the incident wave excites planes waves with anti-parallel phase and group velocities, where the phase velocity is directed towards the interface and the group velocity is directed away from the interface. The anti-parallel phase and group velocities are hallmarks of a left-handed electromagnetic response and they impose negative refraction to the same side of the normal, as first presented by Veselago [19].

The spectral time-averaged Poynting vector in (2.40) is quite similar to

the one proposed in Ref. [154, 155] to analyze energy propagation of discrete Floquet-Bloch modes in infinite, lossless dielectric photonic crystals. However, now we have extended the work to accommodate a continuous range of Fourier field components in a finite, lossy periodic system. Moreover, the direction of the time-averaged power flow can be inferred based on the gradient of the equipotential contours. We applied this concept to derive band diagrams which can be used to distinguish forward- and backward-propagating components of the wave in a medium and provide intuitive visualization of phase and power flow [8].

2.6 Band Diagram Analysis of Layered Metamaterials

To evaluate the functionality of our proposed method, we will derive EPCs for a variety of layered metamaterials, including a thin silver layer sustaining surface plasmon polariton (SPP) mode, Pendry's silver slab lens, the Veselagos lens, and metal-dielectric multi-layered systems capable of canalization and far-field imaging. EPCs are calculated based on spatial-frequency representations for arbitrary lossy layered media of finite extent under plane-wave illumination [5]. For accurate solutions, we check that the solenoidal component of the spectral Poynting vector in each case is small compared to its ir-rotational component. Besides the numerical methods, such as the finite-element method, for analyzing the electric and magnetic field solutions in lossy finite layered media, our proposed analytical expressions yield an efficient analysis method and high-resolution solutions of the internal field modes (up to 500 unique solutions versus k_x).

To support the derived EPC predictions, Maxwell's equations are solved and the full-wave solutions are simulated using the finite-difference frequency-domain (FDFD), a numerical technique to solve the frequency domain harmonic form of Maxwell's curl equations [159, 160]. These simulations are suitable for laterally asymmetric two-dimensional geometries and they can visually provide the spatial distribution details of fields and energy density in and about the layered medium. The simulations are conducted using the FDFD technique due to its superiority over other methods like the finite-difference time-domain (FDTD) method in realistic modeling of lossy materials, where FDFD allows the direct use of tabulated complex permittivity values generally available in Refs. [17, 161]. The basic implementation of the FDFD simulation method starts with defining a spatial grid. Then, a plane wave source is placed in the simulation space, the boundary condi-

tions are defined, and the steady-state distribution of the fields at a single frequency are calculated everywhere [162, 163]. The FDFD simulations in this work are conducted over a discrete two-dimensional spatial grid with the minimal spatial resolution of 1 nm. Simulating layered configurations, the finite simulation spaces are defined wide enough to have laterally long layered media and to minimize boundary effects. The used FDFD MATLAB code is provided in the Appendix.

To excite the SPP modes, we utilize the standard prism configuration by illuminating the layered system with a plane wave source from a high-index dielectric medium to probe the surface plasmon modes of layered metamaterials at high lateral spatial frequencies (where $k_x >> k_0$). For the purpose of quantifying the imaging resolution of layered systems, an optically-thick chromium mask with two $\lambda_0/15$-wide openings and distance T apart is placed between the light source and the layered system. The minimum distance T between the two mask openings that can be clearly identified as two high energy density spots in the image region can be considered as the minimum resolvable feature by the layered system.

2.6.1 SPP Mode as a Window into the Negative-Index World

Considering the simplest layered system that can sustain SPP modes, we derive the EPCs of a thin silver layer under the Kretschmann configuration to investigate the correlation between SPP modes and left-handed electromagnetic behavior. The examined layered system consists of a 40-nm-thick silver layer placed between a semi-infinite dielectric medium (n = 2) and a semi-infinite free-space. The light source is placed in the dielectric medium where the thin silver layer is illuminated by a transverse-magnetic (TM) polarized plane wave with free-space wavelength of $\lambda_0 = 400$ nm where the silver permittivity is characterized by $\underline{\epsilon} = -4.4 + 0.2i$ [17].

Figure 2.6(a) shows the derived EPCs where the most prominent feature is the high density vertical line localized just beyond the free-space cutoff spatial frequency k_0, and it corresponds to the SPP mode, a sub-wavelength guided mode propagating along the surface. we draw a vertical line on the EPC diagram at $k_x \simeq 1.1k_0$ and a wave vector $\vec{k}$ from the origin to the point of highest line density along the vertical line to visualize the SPP mode plane-wave excitation. While the phase velocity along $\vec{k}$ points away from the origin, the group velocity along the spatial frequency gradient points towards the origin. The anti-parallel phase and group velocities relation is the distinct characteristic of a left-handed medium which is

achieved solely within the silver layer along the interface. The excited SPP mode is inherently dispersive due to its near-resonance operation, requires TM polarization, and occurs at a spatial-frequency that is inaccessible to free-space plane-wave illumination. To show the polarization effect, we use a transverse-electric (TE) polarized light source and we show the resulting EPCs in Figure 2.6(b) where the potential gradient has been inverted and the group velocity is generally directed away from the origin.

At surface plasmon resonance, an effective magnetic response is established in the 40-nm-thick silver layer by microscopic circulation of its electric field as illustrated in the FDFD simulation 2.6(c), where the electric fields are the blue arrows and the magnetic fields are the contour lines. This phenomenon leads to a light behaviour analogous to the behavior of a negative-index medium. The electric field circulation is coincided with the background magnetic field. At the silver-air interface where the SPP mode resides, this synchronization is more pronounced. Using homogenization methods, an effective magnetic flux density can be determined and the contributions from the in-plane electric field to the magnetic response can be described by a negative permeability [122, 164]. In contrast to the shaped split-ring resonators that can achieve artificial magnetism at microwave frequencies, the silver layer with a smooth surface can enable electric circulation and attain artificial magnetism and left-handed behavior at visible and UV frequencies over the smallest possible size scales.

In multi-layer metal-dielectric systems, if the fill fraction of the dielectric is sufficiently low, the SPP mode across the metal dielectric interfaces can still support the left-handed behavior. To show the effect of adding dielectric layers to the system, we use the plane wave illumination ($\lambda_0 = 400$ nm, TM-polarization) to excite a metal-dielectric five-layer waveguide made of three 40-nm-thick silver layers separated by two 10-nm-thick dielectric (n=2) layers where the dielectric fill fraction is 0.14. We then map out the derived EPCs where the concentric elliptical contours are increasing close to the origin as shown in Figure 2.6(d). It can be noticed that in this Figure phase and group velocities are nearly anti-parallel at the predetermined surface plasmon resonance spatial frequeny in Figure 2.6(a) $k_x = 1.1k_0$. This observed left-handed behavior is consistent with the theoretical investigations of backward-propagating SPP modes [122, 164], as well as the experimental results of in-plane negative refraction of visible light in metal-dielectric waveguides with fairly thin dielectric cores [165]. The FDFD simulation of the electric and magnetic fields in the multi-layer metal-dielectric system at the surface plasmon resonance shows that the left-handed response arises from microscopic electric field circulation similar to the case of the single

silver layer (Fig. 2.6(f)).

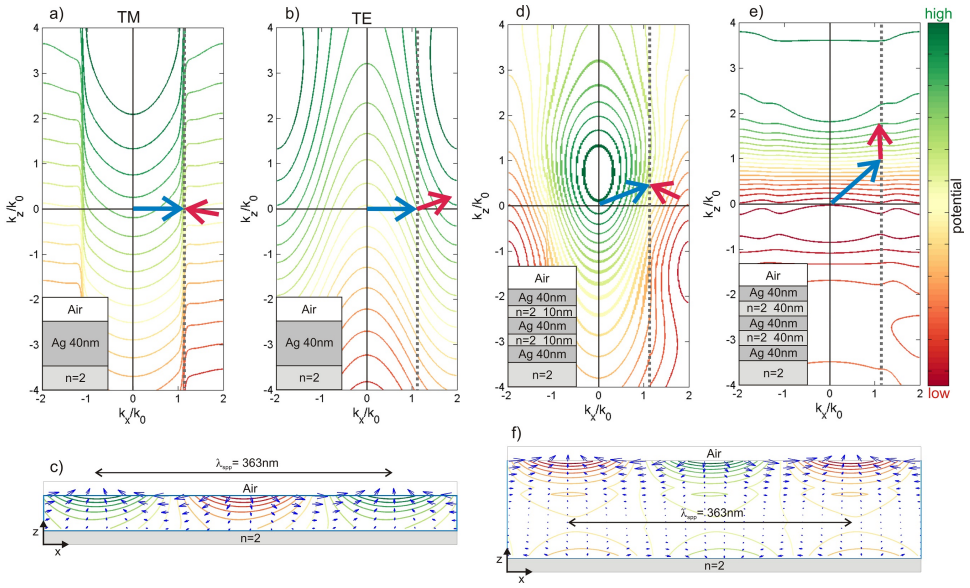

Figure 2.6: Band diagrams reveal interesting propagation characteristics of the SPP mode. We first examine EPCs for a single 40-nm-thick silver layer illuminated by a plane wave ($\lambda_0 = 400$ nm) incident from a dielectric ($n = 2$) prism for either (a) TM or (b) TE polarization. (c) depicts the electric (blue arrows) and magnetic (contour lines) fields in the 40-nm-thick silver layer at the surface plasmon resonance. The x and z scales are the same. Under TM-polarized illumination at the same wavelength, we next examine EPCs for a 5-layer stack of silver and silicon nitride ($n = 2$) layers, where the silver layer thickness is fixed at 40 nm and the thickness of the silicon nitride is either (d) 10 nm or (e) 40 nm. (f) depicts the electric (blue arrows) and magnetic (contour lines) fields in the multi-layer structure at the surface plasmon resonance for the case of dielectric thickness 10 nm. The insets in the EPCs depict the geometrical configuration for each case. The blue and red arrows describe the phase and time-averaged Poynting vector, respectively, of the most dominant mode excited at the spatial frequency $k_x \simeq 1.1k_0$. The location of the dominant mode corresponds to the highest density of contour lines intersected by the vertical line describing the conserved wave-vector component of an incident plane wave.[8]

Investigating the sensitivity of left-handedness response to the dielectric

fill fraction, we increase the thickness of the dielectric layers to 40 nm (dielectric fill fraction of 0.40) where we observe that the EPCs dramatically change and flatten out into a series of horizontal lines with an upward potential gradient as shown in Figure 2.6(e). This is an indication that the system is now supporting bulk mode propagation through the medium as opposed to guided mode propagation along the surface.

2.6.2 Super-Resolving Silver Slab Lens and the Veselago Lens

The capability of a thin silver layer for imaging beyond the diffraction limit, which was first proposed by Pendry, has been demonstrated theoretically and experimentally in the literature. As in the Veselago lens, the perfect resolution capability of Pendry's silver slab is considered to emerge from the amplitude amplification of evanescent waves [27]. To excite evanescent waves at special frequencies beyond the free-space cutoff, a thin planar air region is adopted between the prism and the Pendry's silver slab lens, as well as the Veselago lens. Deriving the EPCs under evanescent wave illumination conditions, we attempt to understand the origins of their resolving power. Beyond the considerable studies in this field, our presented EPC approach offers two novelties. First, the evanescent wave coupling into the lenses is conducted using a realistic laboratory implementable prism-coupling configuration. Second, using the EPC diagrams an intuitive imaging analysis based on phase and power flow in the lens, similar to the classical imaging analysis, is provided.

In Figures 2.7 and 2.8, we map out the EPCs for a Pendry's silver lens and a Veselago lens with equivalent thicknesses of 40 nm. The object plane is placed close to the interface, 20 nm apart from the entrance of the lens, between a dielectric prism and air. For high-k mode plane-wave excitation with large lateral spatial frequencies, a prism with an unusually high refractive index ($n = 5$) is used. Such prism configuration is a realistic emulation of the evanescent wave illumination conditions used in Ref. [27], the first propose of super-resolution imaging in these systems. The comparable EPCs of the two lenses justifies their analogy under near-field conditions. At large spatial frequencies, the behavior of both lenses is governed by the dense vertical lines outside the free-space cutoff (surface modes) and potential gradients directed towards the origin (left-handed response).

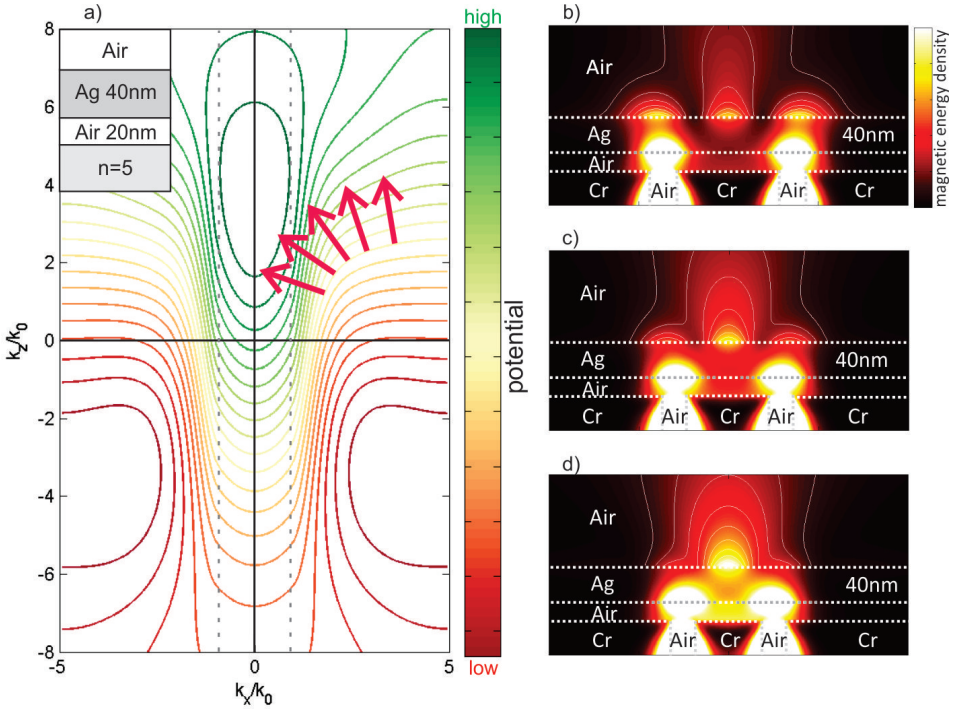

Figure 2.7: Band diagram analysis of Pendry's super-resolving layer. EPCs for (a) Pendry's 40-nm-thick silver slab lens for TM-polarized illumination at the wavelength of $\lambda_0 = 357$ nm. The inset describes the geometrical configuration. The red arrows trace out the time-averaged Poynting vector along a frequency contour. Simulations of a test object imaged by Pendry's silver slab lens when the two point-like features of the object are spaced by (b) $\lambda_0/2.5$, (c) $\lambda_0/3.0$ and (d) $\lambda_0/3.5$. [8]

.

Examining the mapped out EPCs, several observations can be made. First, more modes are supported by the single layers beyond the free-space cutoff spatial frequency compared to the below cutoff. These modes are the high-k modes which are the source of their super-resolution capabilities. Second, the time-averaged Poynting vectors of the high-k modes along a potential contour (group velocities) are mostly directed towards the normal line $k_x = 0$. This emphasizes the capability of these lenses to collect and concentrate light across their extent. Third, the density of modes gradually diminishes as k increases. This is an explicit indication that there is a finite

limit to resolving capabilities of any layered system excited by the realistic prism configuration, even the Veselago lens.

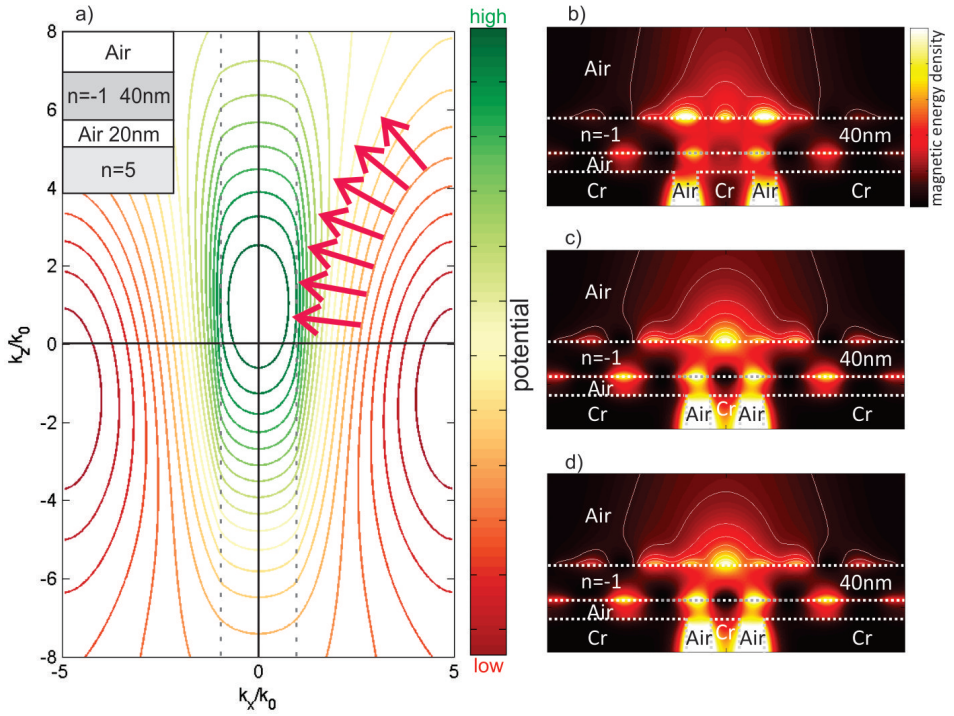

Figure 2.8: Band diagram analysis of Veselago super-resolving layer. EPCs for (a) a Veselago lens ($\epsilon = \mu = -1$) of equivalent thickness for TM-polarized illumination at the wavelength of $\lambda_0 = 357$ nm. The inset describes the geometrical configuration. The red arrows trace out the time-averaged Poynting vector along a frequency contour. Simulations of a test object imaged by the Veselago lens when the two point-like features of the object are spaced by (b) $\lambda_0/4$, (c) $\lambda_0/5$, and (d) $\lambda_0/6$. [8]

.

It is quite evident that the common EPC feature of Pendry's silver lens and Veselago lens is the left-handed guided modes, the prime cause of sub-wavelength imaging. Here, we show how the resolution limits can be quantified by estimating the spatial-frequency bandwidth over which the left-handed modes exist. In Pendry's silver slab, the EPC lines are dense vertical lines just outside the free-space cutoff up to a spatial frequency between $1.5k_0$ to $2.0k_0$. This implies that the minimum resolvable feature

by Pendry's silver lens can be just less than double the free-space diffraction limit ($\lambda/2$). The FDFD simulations of the lens (Figs. 2.7(b)-(d)) show gradual disappearance of discrete lobes in the image region. This suggest that the two objects become indiscernible and result in $T = \lambda/3$ as the minimum resolution, which is consistent with the EPC estimations. On the other hand, the left-handed modes in the Veselago lens stretch up to around double the bandwidth of Pendry's silver lens, between $3k_0$ to $4k_0$. This estimation is supported by FDFD simulations (Figs. 2.8(b)-(d)) which show that the Veselago lens's minimum resolvable feature is about twice smaller than that for Pendry's silver lens ($T_{VL} = \lambda/6$). The arguable results of finite resolution for Veselago lens, which is theoretically shown to have perfect resolution, can be attributed to the use of a lossy, two-dimensional object in the simulation. These structural parameters are adequate to violate the required subtle conditions for perfect imaging.

2.6.3 Canalization in Multi-Layered Structures

Metal-dielectric multi-layer systems can work as canal for light where the light can pass across their extent with little to no diffraction as shown by the simulations in the literature [6, 166]. Due to the complexity of multi-layer systems, which can be made of 40 alternating layers, their electromagnetic properties are commonly described by an effective permittivity tensor of anisotropic form which is modeled based on the effective medium theory (EMT). We nominate the configuration proposed in Ref. [6] as a case study, where the layered system consists of 20 repetitions of a bi-layer unit cell composed of a 7.2-nm-thick silver layer ($\epsilon = -15$) and a 7.8-nm-thick silicon layer ($\epsilon = 14$), at the wavelength $\lambda_0 = 600$ nm. In Figure 2.9(a), we show the band diagram or the EPCs of this configuration derived from the internal electric and magnetic fields besides the volumetric averaging of the local permittivity using EMT which basically extracts an effective refractive index for the metamterial configuration and yields a single horizontal line located at $k_z \simeq 0$.

The band diagram consists of flat elliptical contours which are roughly symmetric about $k_z \simeq 0$, with two distinguished bands of horizontal lines, one centered at $k_z \simeq k_0$ (forward- propagating mode) and another centered at $k_z \simeq -k_0$ (backward-propagating mode). Since the contours remain flat beyond the free-space cutoff spatial frequency, an incident plane wave at any angle of incidence can excite modes that pass energy across layers' extent in either forward or backward direction. Considering the EMT method, the plotted EMT line show that EMT can precisely predict the dominant flat

horizontal contours of EPC, particularly those ones below the free-space cutoff frequency, but it shows to be unsuccessful to predict their locations in k-space.

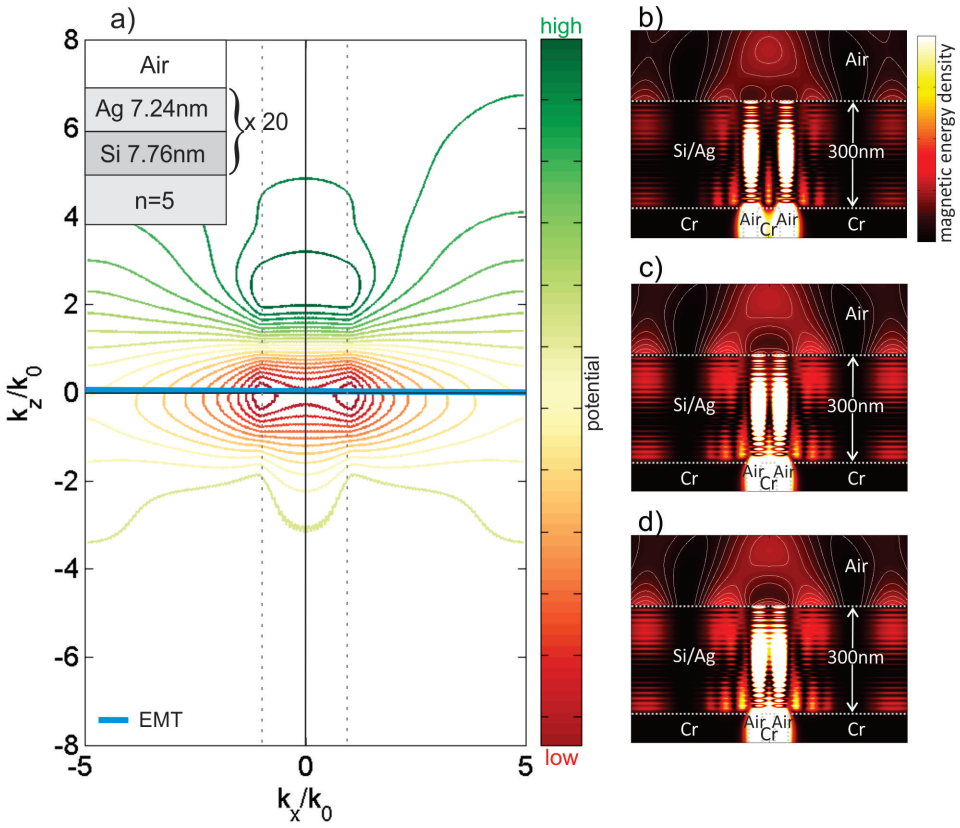

Figure 2.9: Band diagram for the metal-dielectric multi-layer systems studied in Ref. [6] for the case of TM-polarized plane-wave ($\lambda_0 = 600$ nm) illumination from a high-index dielectric ($n = 5$) prism. The blue line depicts the simplified EPC predicted from effective medium theory (namely, Maxwell-Garnett theory). FDFD simulations of the multi-layers imaging a test object when the two point-like features of the object are spaced by (b) $\lambda_0/8$, (c) $\lambda_0/9$, and (d) $\lambda_0/10$. [8]

.

This reveals the limitations associated with EMT compared to the rigorously derived EPC values. The FDFD simulations shown in Figures 2.9(b)-(d) visually illustrate the ability of the examined multi-layer system to chan-

nel light straight through the medium even with light streams spaced $\lambda/10$ apart from each other. The high resolving power observed in the simulations is due to employing the ideal lossless material parameters originally used in Ref. [6]. In case of simulating light propagation through materials with realistic losses, the resulting resolving power is expected to be reduced.

2.6.4 Far-Field Flat Lens Imaging

For better understanding of the electromagnetic field interactions that enable far-field imaging (flat lensing) in a recently presented layered system [7], we apply the introduced EPC as the fundamental field analysis technique. The reported far-field flat lens is designed to work in free-space and it is made of three repetitions of a five-layer unit cell with the layer sequence Ag (33 nm) - TiO_2 (28 nm) - Ag (30 nm) - TiO_2 (28 nm) - Ag (33 nm). To understand the external optical properties of this structure by simple geometrical optics, it has been modeled as a homogeneous, isotropic, negative-index medium. This model works for describing the structure's external optical properties, but does not provide insight into the dynamic behaviour of the internal fields. This insight can be gained by analyzing EPCs of the internal fields. The EPCs of the structure beside the derived band diagrams using two homogenization methods (S-parameter method [167] and Floquet-Bloch modes [125]) are shown in Figure 2.10. The EPC has a prominent upward concavity band feature similar to the observed band curvature in the EPC of the negative-index slab in Figure 2.5(b). Such upward EPC curvature in the medium opposes the downward wavefront curvature in free-space and forces the exiting wavefront to re-form into a real image in the transmitted region. Furthermore, the associated internal fields' group velocity is directed towards the normal $k_x = 0$ line, a feature that is important for collecting and concentrating light to form a real image. Consistent with past experiments, the imaging capability of this structure is fundamentally limited to the free-space diffraction limit due to the absence of the EPC upward concavity feature beyond the free-space cutoff.

S-parameter method and the Floquet-Bloch theorem are two of the widely used homogenization methods for modeling metamaterials. They yield an infinite number of potential solutions in k space (Fig. 2.10(b)), but the position and concavity of the dominant EPC band can be accurately described by only one of the solutions. It can be noticed that the best matching solution from the S-parameter method is at the $m = 2$ branch and the best one from the Floquet-Bloch theorem is at the $m = 1$ branch. In this section, we show that EPCs are useful for linking internal and external

light behaviors of layered structures as well as determining the best effective medium model [168] through recognizing the one that most accurately describes EPC features.

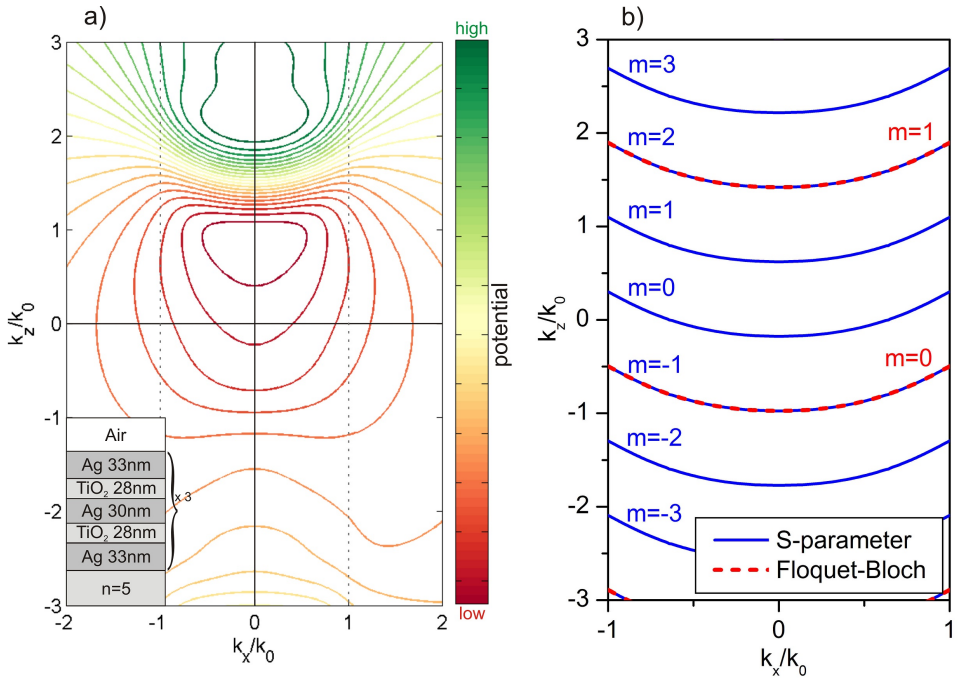

Figure 2.10: (a) EPC for the flat lens structure shown in Ref. [7] to be capable of far-field imaging in the UV. The EPC is derived for TM-polarized plane-wave ($\lambda_0 = 365$ nm) illumination from a dielectric ($n = 5$) prism. The inset depicts the geometrical configuration of the flat lens. (b) shows the simplified EPCs derived using two common homogenization techniques: S-parameter method (blue solid) and Floquet-Bloch modes (red dashed). [8]

.

2.6.5 Far-Field Flat Lens with Less Metal

Using the EPC concept and considering the absorption losses, we manage to engineer and design a metal-dielectric layered system that is capable of far-field imaging with minimal use of metal. We begin with a tri-layer unit cell template composed of a single TiO_2 layer sandwiched by two silver layers of identical thickness. While using the thinnest silver layers possible, we design a far-field imaging layered system with the essential phase and

power flow key features where the associated EPC should consist of a single dominant band with an upward concavity.

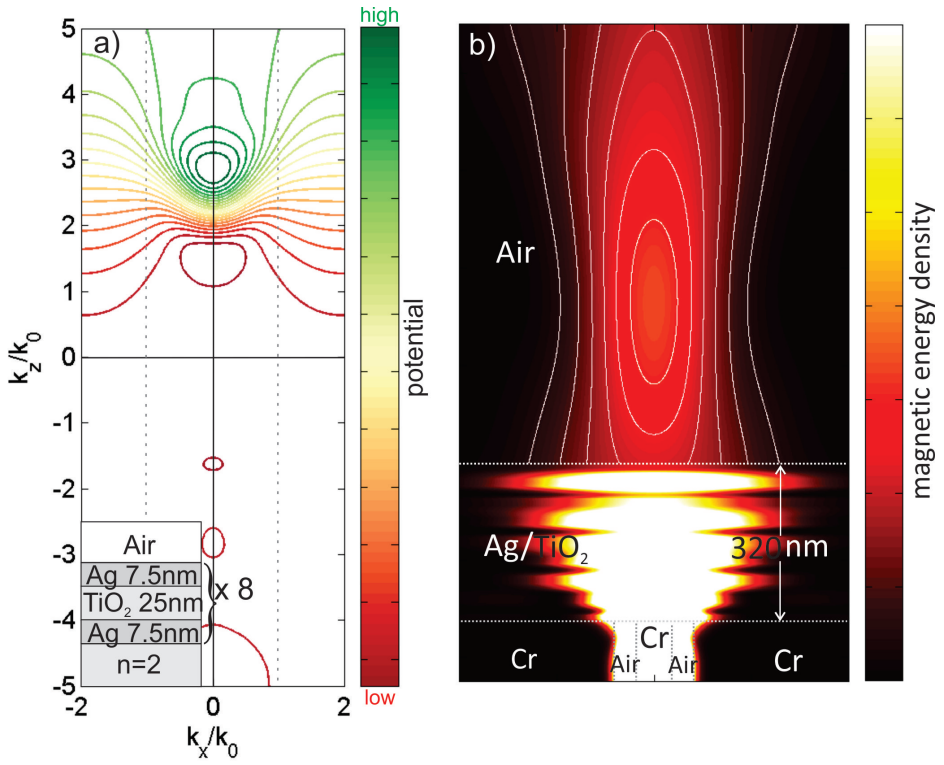

Figure 2.11: (a) EPC of a new layered flat lens structure that is capable of far-field imaging, yet possesses about half the metallic fill fraction of the flat lens presented in Ref. [7]. The proposed structure consists of 8 repetitions of a unit cell with the layer sequence Ag (7.5 nm) - TiO_2 (25 nm) - Ag (7.5 nm). The EPC is derived assuming TM-polarized plane-wave ($\lambda_0 = 330$ nm) illumination from a dielectric ($n = 2$) prism. (b) shows an FDFD simulation of the proposed flat lens imaging a test object placed on its surface. Tapering of the magnetic energy density in the image region at a location spaced about a wavelength from the exit surface confirms that the structure is capable of forming real images in the far field. [8]

Optimization of the layered system according to the specified design objective and constraint yields an optimal design consisting of 8 repetitions of the seed tri-layer unit cell with the sequence and thicknesses of Ag (7.5

nm) - TiO_2 (25 nm) - Ag (7.5 nm). The proposed far-field flat lens design is operational at the UV wavelength of $\lambda_0 = 330$ nm. Using less metals, we fulfill the set design constraint where the metal fill fraction of the new design (0.38) is about half the metal fill fraction of the structure discussed in the previous section (0.63). The new flat lens design achieves a prominent upward concavity EPC band feature as shown in Figure 2.11(a), the required EPC feature for far-field imaging. The FDFD simulations of this system in Figure 2.11(b) confirm its far-field imaging performance where a real image of the apertures, though not distinct, is formed about a wavelength apart from the exit surface. The introduced less metal far-field flat lens possesses less internal losses due to lower metallic content and this yields a boost in light transmission. Therefore, this flat lens design can be considered as a small step towards more practical flat lenses that work for real-world applications such as UV microscopy.

2.7 Summary

Considering a general layered system configuration with practical constrains of loss and finite extent, we developed a new representation of the electromagnetic field solutions in the Fourier domain. We then used the new field representation to derive and plot the band diagrams. The developed Fourier domain solution is a compact product of three terms where each term is dependent on a distinctive physical parameter of the layered system. There are two main contributions in this work. The first is the manifestation of the Floquet-Bloch modes as one of the explicit terms of the Fourier domain solution using only Maxwell's equation and without invoking the Floquet-Bloch theorem. This work shows the functionality of representing the electromagnetic field solutions of a layered system in Fourier domain to analyze its complex electromagnetic properties. The promising conclusions of this work suggest that the Fourier domain analysis method can be applied to analyze the electromagnetic properties of more complex geometries. The second is the introduction of band diagrams as useful tool for designing practical layered systems as well as validating conventional homogenization methods. We have used EPCs to design a layered system that mimic the left-handed electromagnetic response, an anisotropic metamaterial that is capable of canalization, and a far-field highly transmissive flat lens which incorporates the minimum amount of metal.

Chapter 3

Flat Lens Criterion by Small-angle Phase

In this chapter, we introduce a quantitative method based on the classical ray optics to analyze the imaging capability of any ultra-thin planar slab made of homogeneous isotropic layers. Unlike the band diagram method proposed in the previous chapter, this method use the small-angle phase behavior as a criterion to predict the imaging capability of any planar slab and to estimate the image plane location.

Here, we only consider the small-angle phase behavior and neglect the large angle and evanescent plane wave components to develop a simple, general and instant flat lens metric that can provide acceptable but not very accurate estimations before conducting any extensive analysis. To validate this method, we applied the flat lens criterion to some of the already studied structures of near-field and far-field flat-lenses. Using this criterion, we derive approximate analytical expressions to show when a single layer or a multi-layer system can act as a flat lens. We ultimately demonstrate how the introduced flat lens criterion is practical by effectively designing three distinct flat lenses with novel functionalities.

3.1 Flat Lens Criterion

The imaging response of a flat lens can be described by the classical ray optics using the concept of point spread function (PSF) and paraxial approximation. Flat lens analysis based on the PSF amplitude is a standard approach [9, 28, 55, 58]. For a complete analysis, we also analyze the PSF phase and we underline its potential as a flat lens indicator. Considering a planar medium with the same geometry of the layered system illustrated in chapter 2 (Fig. 2.2), we place a point source in the object region directly on the entrance face of the medium at $z = -d$. We assume that the object region ($z < -d$) and the image region ($z > 0$) are composed of generally dissimilar, isotropic and homogeneous media. The transmitted light source

in the image region can be decomposed in the xz plane as a uniform plane-wave spectrum parameterized by the wave vector $\vec{k}_t = k_{t,x}\hat{x} + k_{t,z}\hat{z}$. Along the z axis, we only need to evaluate the phase of the plane-wave components (Φ_z) due to translational symmetry. The phase of the plane-wave components exiting the slab $\Phi_z(z = 0)$, referenced to a common initial value at the source, can trace out the wavefront and map out the loci of equi-phase points in the image region.

At an arbitrary point z_0, the phase of the PSF can be written as $\Phi_z(z_0) = \Phi_z(z = 0) + k_{t,z} z_0$. In case of ideal image formation at z_0, the phase is invariant for all plane-wave components at z_0 based on Fermat's principle, $\partial\,\Phi_z(z_0)/\partial\,k_{t,z} = 0$. The image formation will suffer from spherical abberations and we will not have an ideal image since the monochromatic light phase is not invariant for all plane-wave components at any point.

Applying the concept of phase invariance on the small-angle plane-wave components ($k_{t,x} << k_{t,z} \simeq k_t$), the paraxial image location in terms of the PSF phase can be defined by

$$s = z_0 \equiv -\frac{\partial\,\Phi_z(z = 0)}{\partial\,k_{t,z}}\Big|_{k_{t,z}=k_t} \quad , \tag{3.1}$$

where image plane location s is the maximum working distance of the flat lens and it can be positive for a real image in the image region or negative for a virtual image in the slab or object regions. Hence, a planar medium can be defined as flat lens if it is capable of producing a real paraxial image ($s > 0$) of a point source located on its entrance face. The flat lens criterion is defined for near zero numerical aperture (NA), the range of angles over which the system can accept light. Usually, this criterion has been used to describe conventional optical systems. However, we show that this condition is applicable to any flat lens since it depends only on the phase profile at the slab exit.

Considering the PSF interpretation as a transfer function relating the iso-planatic field quantities along object and image planes perpendicular to the optical axis, the amplitude of the PSF is commonly presented versus the normalized lateral wave vector $k_{t,x}/\,k_t$ [169]. On the other hand, the PSF phase is associated with spherical wavefront curvature and spherical aberrations mapping onto high order terms which are difficult to distinguish on a graph and eventually makes the PSF phase inconvenient to be displayed versus $k_{t,x}/\,k_t$. Knowing that $\Phi_z(z = 0)$ is dependant on $k_{t,z}$ in Eq. (3.1), here we suggest to plot the PSF phase as a function of $q_t = 1 - k_{t,z}/\,k_t = 1 - \cos\theta_t$, where θ_t is the angle of the transmitted light at the exit surface.

Over the range $0 \leq q_t \leq 1$, q_t describes propagating waves. Plotting the PSF phase versus q_t, several observations can be evolved (Fig. 3.1). Positive slope will be an indication of flat lens behavior, the slope at the y-intercept $(\partial\,\Phi_z(z\,=\,0)/\partial q_t|_{q_t=0})$ can be counted as an estimation for the paraxial image location, and the departure from linearity will imply the occurrence of spherical aberrations.

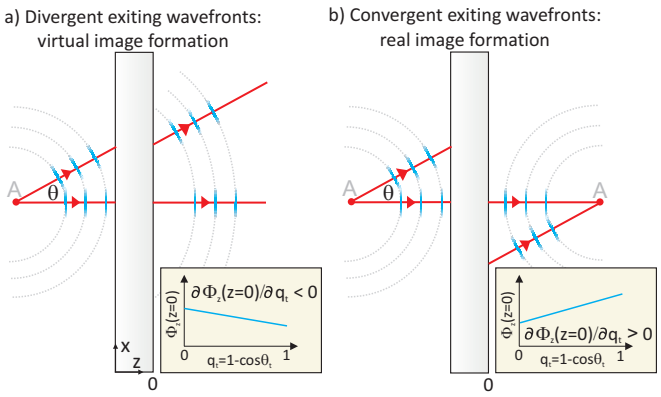

Figure 3.1: Curvature of the wavefronts exiting a planar slab for the cases of (a) virtual and (b) real image formation. By plotting the phase $\Phi_z(z = 0)$ versus $q_t = 1 - \cos\theta_t$, the possibility of a flat lens can be determined by inspection from a positive slope. [4]

In this work, we have applied the flat lens criterion to analyze the imaging of a point source located on the entrance face of the slab. Such analysis is extendable to volumetric objects which can be treated as collections of point sources along the lateral and longitudinal directions. As we scan over the lateral direction along the translational symmetry of the slab, we will have a shift in the image point towards the same lateral direction with no effect on the location of the image plane. Contrary, the imaging capability of the slab will distinctly change as we scan over the longitudinal direction along the normal line to the slab. As long as the depth of an object is less than the characterized image plane location s of a flat lens, a real image of the object placed perfectly against the entrance face of the flat lens can be created.

3.2 Methodology

Validating the proposed flat lens criterion as a general criterion to predict flat lens behavior, we first visit some past flat lens implementations operating in both the near- and far-fields and calculate the paraxial image location. Then, we use this criterion as a metric to design new flat lens configurations. The suggested flat lens criterion predict the paraxial image plane location using the PSF derived from the transfer matrix method [170, 171].

For past and new flat lens designs, the predictions of the image plane location have been compared with the full-wave electromagnetic simulations. These simulations display the solutions of Maxwell's equations over a two-dimensional grid with pixel size of at most 1 nm using the finite-difference frequency-domain (FDFD) technique. The utilized light source in simulations is a TM or TE polarized light source with normal incidence plane wave propagating along the $+z$ direction. Based on the use of TM or TE polarization, the simulation results are displayed in terms of the distribution of magnetic or electric energy density, respectively.

To conduct near diffraction limit imaging simulations, an opaque chromium masking layer with two $\lambda_0/10$-wide openings spaced by $\lambda_0/2.5$, which is slightly below the diffraction limit, is placed between the flat lens and the plane wave source. Such simulations reveal further information about the flat lens resolution capabilities near the diffraction limit which is one of the most appealing claimed features of metal-dielectric layered flat lenses. The used permittivity values in the transfer matrix method calculations and FDFD simulations are from [17] for silver and gold and from [161] for chromium. The used permittivity values in the calculations of past published flat lens implementations are taken from the original works.

3.3 Comparison with Past Flat Lens Results

3.3.1 Pendry's Silver Slab Lens

We use the single silver layer flat lens configuration as the first test platform for investigating the small-angle phase criterion. It has been shown that a thin silver layer (Pendry's silver slab) can work as a flat lens [27] mimicking the electromagnetic properties of a perfect negative refractive index slab (Veselago lens). Due to its evanescent wave amplification, this single layer flat lens was suggested as a feasible tool to image beyond the diffraction limit. Such super-resolution behavior is not directly predictable using the small-angle phase which can only predict the existence and location

of the paraxial image. Considering Pendry's setup, a 40-nm-thick silver layer with complex permittivity of $\underline{\epsilon} = -1.0 + 0.4i$ at wavelength of $\lambda_0 = 356.3\,\text{nm}$ is placed 20 nm apart from an object. Applying the flat lens criterion, the image plane location is predicted to be at $s = 36\,\text{nm}$, which is comparable to the reported image location of 20 nm in [27]. This disparity could be due to accounting for large angle plane-wave components and assuming ideal negative refraction in the reported image location by Pendry.

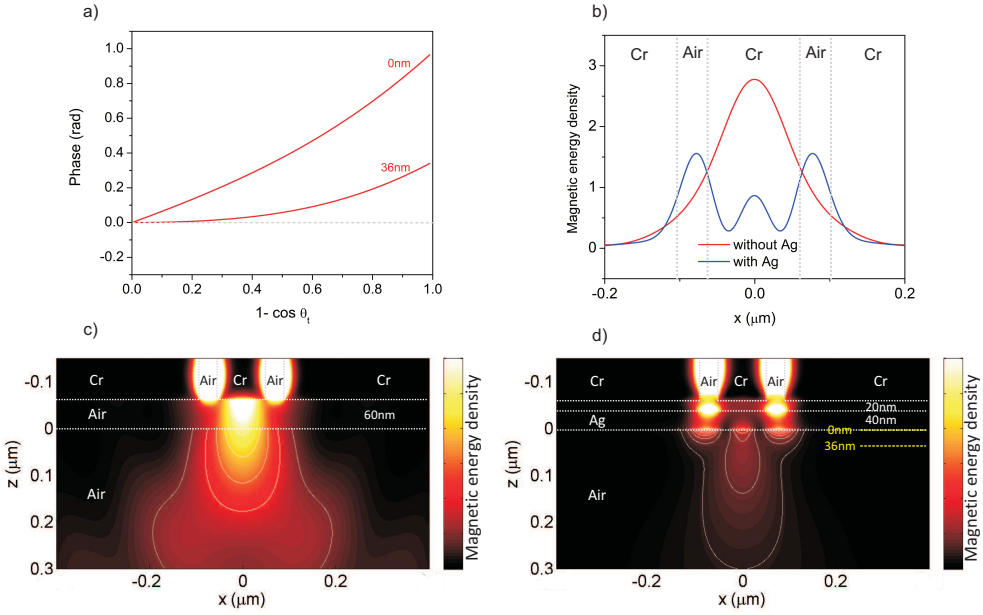

Figure 3.2: (a) PSF phase for Pendry's silver slab lens consisting of a 40-nm-thick Ag layer with a permittivity of $\underline{\epsilon} = -1.0 + 0.4i$ at a wavelength of $\lambda_0 = 356.3\,\text{nm}$, where the object is 20 nm away from the entrance of the slab. The phase has been calculated at the exit of the slab ($z = 0$ nm) and the paraxial image location has been predicted at $z = 36$ nm. (b) FDFD-simulated profile of the magnetic energy density at the image plane $z = 36$ nm for the cases where the near diffraction limit spaced objects are imaged without (blue) and with (red) the silver slab lens. Simulated time-averaged magnetic energy density distributions of the illuminated object are shown (c) without and (d) with the 40-nm-thick Ag layer. The yellow dashed lines in (d) show the positions where the PSF phase profiles have been calculated in (a). [4]

The phases of the transmitted light versus q_t at the exit interface of the silver layer, and at the paraxial image location are shown in Figure 3.2(a). The former phase profile at the exit interface is a clear indication of the existence of a real paraxial image due to its positive slope. The second phase profile at the image location of $s = 36\,\text{nm}$ shows to be consistent with the Fermat's principle of real image formation where the phase profile is flat at small angles. To investigate if the silver slab is capable of imaging slightly below the diffraction limit $\lambda/2$, a comparative simulation of the magnetic energy density at the image location (36 nm) is conducted using an almost diffraction limit spaced object ($\lambda/2.5$) with and without the silver slab (Fig. 3.2(b)).

For further highlight on imaging with resolution slightly below the diffraction limit using a thin silver layer, we show the spatial energy density distributions for the two cases of with and without the silver slab in Figs. 3.2(c) and 3.2(d) respectively. Although it is difficult to firmly locate the image plane location using the energy density simulations due to the decay of the energy density near the exit interface, the energy density profile at 36 nm (Fig. 3.2(b)) is shown to be consistent with the small-angle phase prediction.

3.3.2 Near-field Imaging with Silver Layers

Imaging with flat lenses is usually confined to near-field due to the difficulties associated with satisfying the physical conditions for real image formation at far-field using a flat slab. Here, we discuss the correlation between the predicted real paraxial image and the reported near-field super-resolution image in some of the past UV imaging experiments on photoresist using a silver layer.

Using the proposed flat lens criterion, we reasonably explain some of the observed near-field imaging behaviours of the past flat lens implementations by analyzing their paraxial image locations (Fig. 3.3). Imaging beyond the diffraction limit or super-resolution imaging using very thin silver layers of thicknesses down to 36 nm has been shown in several experiments [9, 10, 50, 54]. At UV wavelengths, the slope of the phase profiles of the past implemented flat lenses using a 36-nm-thick silver layer [9] and a 50-nm-thick silver layer [10] are both positive (Fig. 3.3(a)). The corresponding paraxial image locations have been predicted to be at $s = 10\,\text{nm}$ and $s = 22\,\text{nm}$, respectively. Comparing the imaging capability of a metal layer versus a dielectric layer of the same thickness, we examined the third [11, 53] and the forth [12] flat lens configurations illustrated in Figure 3.3.

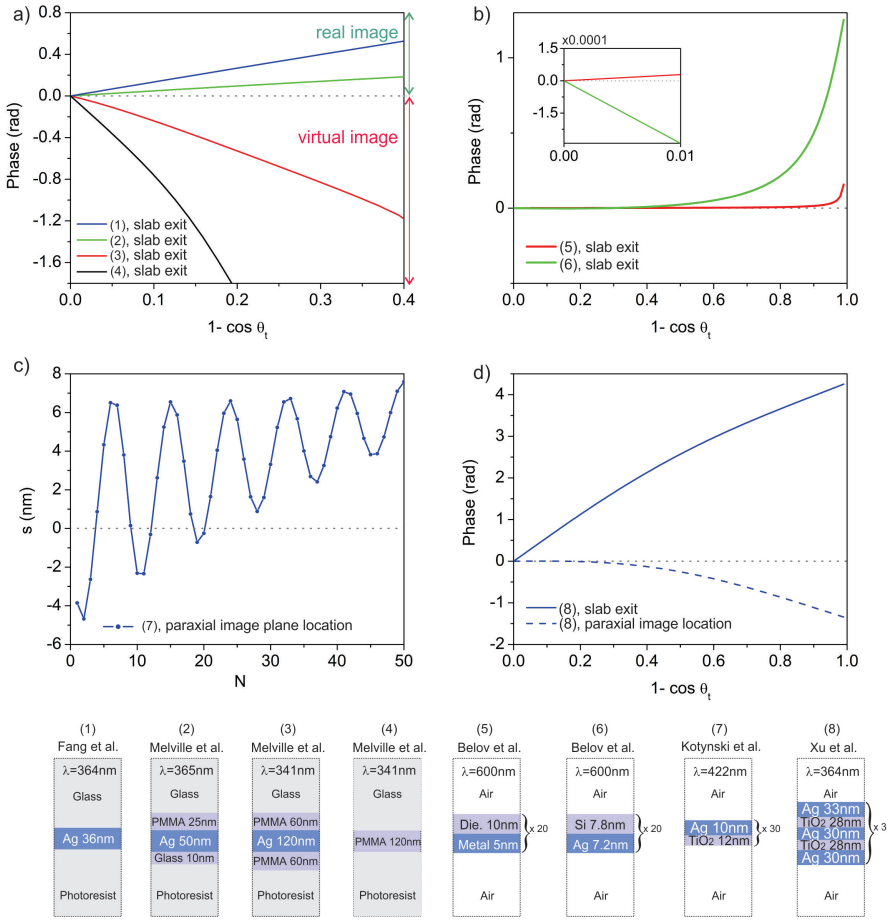

Figure 3.3: Flat lens criterion applied to past implementations. (a) PSF phase at the exit surface of lenses based on the 36-nm-thick silver layer studied in Fang et al. [9], the 50-nm-thick silver layer studied in Melville et al. [10], and the 120-nm-thick silver layer studied by Melville et al. in [11, 12], along with the control used in [12] of a 120-nm-thick PMMA layer. (b) PSF phase at the exit surface of lenses based on metal-dielectric multilayers studied by Belov et al. [6]. The inset in (b) shows a magnified view of the data near normal incidence. (c) Paraxial image location as a function of unit cell repetition for the periodic metal-dielectric layered system studied by Kotynski et al. [13]. (d) PSF phase at the exit surface of the geometry studied by Xu et al. [7] where the flat lens composed of metal and dielectric layers. [4]

At a wavelength of $\lambda_0 = 341\,\text{nm}$, the slope of the phase profile at the exit face of the 120-nm-thick silver layer sandwiched between two 60-nm-thick PMMA layers is negative, which is the sign of having a virtual paraxial image (Fig. 3.3(a)). As predicted by the slope of the phase, the flat lens criterion calculations located the image at $s = -40\,\text{nm}$ inside the flat lens region. On the other hand, the single 120-nm-thick PMMA layer configuration forms a virtual paraxial image at $s = -150\,\text{nm}$. This insists that silver layer has significantly improved the imaging performance bringing the image plane location closer to the image region ($s = -40\,\text{nm}$). The reported experimental results in the literature are consistent with our real and virtual paraxial image predictions.

The discussed comparative analysis results showed that the real paraxial image formation using a thin film is fully dependant on the film thickness. To form a real image, the film thickness should be sufficiently smaller than the wavelength as stated before by Pendry. It can be also concluded that having a real paraxial image within the image-capturing region is a prerequisite for near diffraction limit resolution imaging. However, understanding and affirming this postulation requires further work. In the next sections, we will analytically discuss the film thickness effect on flat lens imaging.

3.3.3 Anisotropic Metamaterial Lenses

The periodic metal-dielectric bi-layer implementations of flat lens have been proposed to mimic the properties of anisotropic metamaterial for the purpose of imaging as theorized in previous works [23, 49]. A metal-dielectric bi-layer system can be characterized by a flat wave vector diagram and described by a highly anisotropic permittivity tensor, if the permittivity and thickness values of the metal ($\epsilon_M,\ d_M$) and the dielectric ($\epsilon_D,\ d_D$) layers in the bi-layer composition satisfies the relations $\epsilon_M / \epsilon_D = -\,d_M / d_D$ and $\epsilon_M + \epsilon_D = 1$ [6, 57, 63]. The characterized flat wave vector relation in bi-layer metal-dielectric flat lenses enables the front to back direct image projection across the slab.

Considering three different multi-layer systems designed as anisotropic metamaterial lenses [6, 13], we examine the consistency of the reported imaging properties with the predicted paraxial image locations (Fig. 3.3(b)). At the wavelength of $\lambda_0 = 600\,\text{nm}$, the calculated PSF phase of two lossless 20-unit-cell systems presented in [6] have been analyzed and yield the respective paraxial image locations of $s = 0.2\,\text{nm}$ and $s = -3\,\text{nm}$, where the characterized unit cell parameters of the first layered system are $\epsilon_M = -1$, $\epsilon_D = 2$, and $d_M / d_D = 1/2$ and the second one are $\epsilon_M = -14,\ \epsilon_D = 15$,

and $d_M / d_D = 14/15$. The predicted paraxial image locations ($s = 0.2\,\text{nm}$, $s = -3\,\text{nm}$) are quite close to the exit interface of the slab as reported in the referred work [6]. At the wavelength of $\lambda_0 = 422\,\text{nm}$, a different study [13] provided the detailed simulation data for a lossy multi-layer system with unit cell parameters of $\epsilon_M = -5.637 + 0.214i$, $\epsilon_D = 2.6^2$ and $d_M / d_D = 10/12$. As the number of unit cell repetitions N increases from 1 to 50, the size of the spot light expands and shrinks at a fixed plane near the output face. Plotting the spot size versus N results in a consistently oscillating profile with 6 evenly spaced local minima. We obtain identical oscillatory dependence on N by calculating the paraxial image locations using the PSF phase (Fig. 3.3(c)). This implies that the observed spot size variation in [13] is partially due to image focusing and de-focusing at a fixed plane.

3.3.4 Negative-Index Metamaterial Lens

Emulating the perfect negative index flat lens proposed by Veselago [19], a recent pioneer work introduced a metal-dielectric multi-layer flat lens as an isotropic negative index metamaterial [7]. Operating at the wavelength of $\lambda_0 = 364\,\text{nm}$, a far-field image at 360 nm apart from the flat lens exit interface has been reported [7] which is found to be comparable to the predicted paraxial image location of $s = 370$ based on the PSF phase calculations (Fig. 3.3(d)). The deviations from unity for the phase profile at the paraxial image location can be attributed to the wavefront aberrations. The extrapolation of these deviations demonstrates the occurrence of wavefront aberrations lower than $\lambda_0/4$ up to about unity NA.

3.4 Validation of Flat Lens Criterion by Full-Wave Simulations

We use the electromagnetic full-wave FDFD simulations of past flat lens configurations to validate the introduced flat lens criterion. This comparison analysis shows moderate agreement between the simulated image locations and the paraxial image locations across near-field and eminent consistency across far-field regimes. We revisit four of the considered flat lenses in the previous sections: 1) the 120-nm-thick silver layer presented in [11, 12], 2) the 50-nm-thick silver layer presented in [10], 3) the metal-dielectric anisotropic metamaterial lens reported in [6], and 4) the metal-dielectric negative-index metamaterial lens reported in [7]. We then conduct the full-wave simulation for each flat lens system.

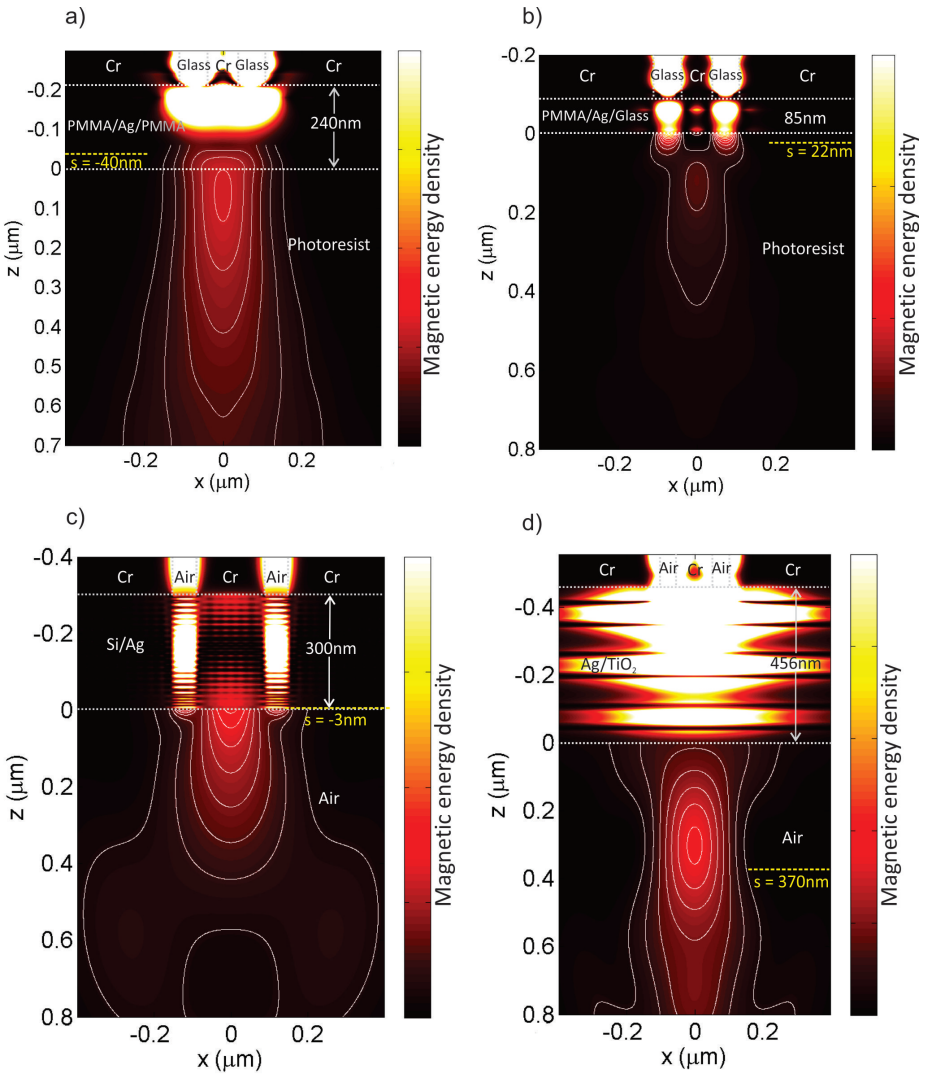

Figure 3.4: Comparison of paraxial image locations predicted by PSF phase and numerical simulations. FDFD-calculated time-averaged energy density distributions for flat lenses consisting of (a) a 120-nm-thick silver layer studied in [11, 12], (b) a 50-nm-thick silver layer studied in [10], (c) metal-dielectric multi-layers studied in [6], and (d) metal-dielectric multi-layers studied in [7]. In all cases, we use near diffraction limit spaced objects consisting of two, $\lambda_0/10$-wide openings spaced $\lambda_0/2.5$ apart in an opaque mask that is illuminated by a TM-polarized plane wave. The yellow dashed line in each panel shows the corresponding paraxial image location calculated from the slope of the output phase. [4]

The simulations and the paraxial image locations, depicted by dashed yellow lines, are shown in Figure 3.4. Except the first flat lens configuration with the 120-nm-thick silver layer where the simulation of the energy density distribution shows divergent behaviour in the image region (Fig. 3.4(a)), the simulations of the other three flat lens systems show convergent energy density distributions at certain spots in the image region (Fig. 3.4(b), (c), (d)). The narrowest plane in the simulation of the 120-nm-thick silver layer flat lens is located close to the predicted virtual paraxial image location $s = -40\,\text{nm}$ which implies that this system is not capable of forming an image of the object in the image region (Fig. 3.4(a)).

On the other hand, imaging by lenses made of 50-nm-thick silver layer and anisotropic metamaterial is quite evident to provide imaging resolutions slightly below the diffraction limit as it can be observed from the simulations. Two high energy density spots appear in the simulations near lenses' output faces at plane locations roughly match the estimated real paraxial image locations calculated by the phase of the PSF [Figs. 3.4(b) and 3.4(c)]. Even though the predicted paraxial image location is determined without accounting for the evanescent plane-wave components which are believed to be the main contributor in super-resolution imaging, surprisingly we found reasonable agreement between our predictions and the exact full-wave simulations.

Finally, a single high energy density spot well-separated from the output face is observable in the full-wave simulation of the negative-index metamaterial lens. This is a clear indication of having a diffraction-limited image at a position that is again quite consistent with the predicted real paraxial image location (Fig. 3.4(d)). Unlike the second and third considered lenses, the negative-index metamaterial lens cannot resolve the defined near diffraction limit spaced objects in the image region.

3.5 Flat Lens Condition for a Single Layer

To precisely determine when a single homogeneous layer can generate a real paraxial image based on the expression (3.1), we develop compact analytical expressions that can work as determinant conditions for imaging with a flat slab. First, we define the most generic configuration where a homogeneous, non-magnetic, isotropic layer of thickness d, characterized by a permittivity of $\underline{\epsilon} = \epsilon' + i\,\epsilon''$ and a permeability of $\mu = 1$, is placed in free-space. For a point source with a plane-wave spectrum parameterized by the wave vector $\vec{k}_o$ in the free-space object region where $\vec{k}_o = k_{o,x}\hat{x} + k_{o,z}\hat{z}$,

the transmitted plane waves through the single layer are modulated by a transmission coefficient $\underline{t}$ where

$$\underline{t} = \frac{4\,\underline{p}}{(1+\underline{p})^2 e^{-i\underline{k}_z d} - (1-\underline{p})^2 e^{i\underline{k}_z d}} \quad . \tag{3.2}$$

The parameter $\underline{p}$ is defined as $\underline{k}_z/(\underline{\epsilon}\, k_{o,z})$ for TM polarization and as $\underline{k}_z/\, k_{o,z}$ for TE polarization, $\underline{k}_z$ is the propagation constant within the layer where $\underline{k}_z = k_0\sqrt{\underline{n}^2 - \sin\theta^2}$, k_0 is the magnitude of the free-space wave vector, $\underline{n}$ is the layer refractive index where $\underline{n} = \sqrt{\underline{\epsilon}}$, and θ is the angle of incidence. The derived transmission coefficient $\underline{t}$ accounts for all included losses due to multiple reflection and propagation within the slab. The phase of $\underline{t}$ is equivalent to the phase of the PSF at $z = 0$ ($\Phi_z(z = 0)$) from which the paraxial image location can be calculated.

3.5.1 Flat Lens for TM Polarization

For TM polarization and under the thin-film and paraxial approximations, a lossy layer similar to Pendry's silver slab yields a first order expression of $k_0 d$ as

$$\frac{\partial\, \Phi_{z,TM}(z=0)}{\partial q_t}\Big|_{q_t=0} \doteq -k_0 d \left(\frac{1}{2}(\,\epsilon' - 1) + \frac{\epsilon'}{|\underline{\epsilon}|^2}\right) \quad , \tag{3.3}$$

which must be positive for real image formation. To keep the slope of the phase positive, a purely permittivity dependant condition must be satisfied ($\epsilon' < |\underline{\epsilon}|^2/(|\underline{\epsilon}|^2 + 2)$). Such condition can be fulfilled if the single layer is made of metals.

The derived expression in Eq. (3.3) predicts a paraxial image location of $s = 1.86d$ for Pendry's silver slab with $\underline{\epsilon} = -1 + 0.4i$ [27]. This prediction is almost double the theoretically expected image location for a Veselago lens of equivalent thickness $s = d$ [19]. Since the proposed method for prediction of the paraxial image location using Eq. (3.3) is a function of the flat lens thickness d, we investigate the dependence of the paraxial image location s on d by calculating s of a point source placed directly on the entrance of an ideal Veselago lens and Pendry's silver slab lens for different thicknesses. Figure 3.5 shows the thickness dependence of the paraxial image location. Although it has been assumed by Pendry that Veselago lens and thin silver slabs have identical paraxial image locations under electrostatic conditions, in contrary Figure 3.5 demonstrates the differences between the paraxial image locations of Veselago lens and Pendry's silver slab.

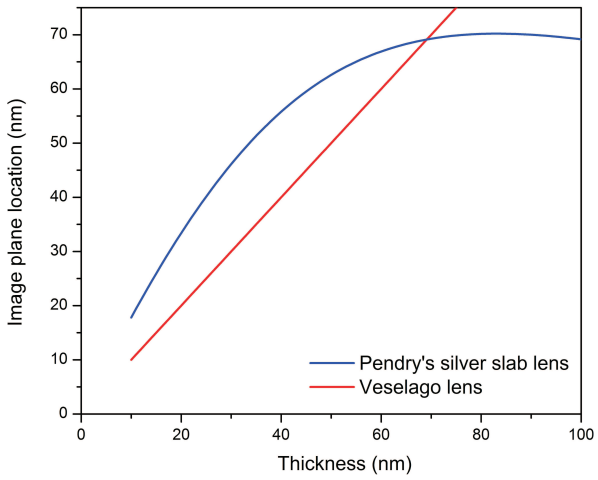

Figure 3.5: Paraxial image location versus thickness for an illuminated object located at the entrance of the ideal Veselago lens (red) and Pendry's silver slab lens (blue) when illuminated at the wavelength of $\lambda_0 = 356.3\,\text{nm}$. For the ideal Veselago lens, the image location is equivalent to the slab thickness, $s = d$. [4]

Ignoring the flat slab losses based on the thin-film and paraxial approximations, a more accurate flat lens criterion with higher order terms can be derived. For TM polarization, the flat lens criterion up to the third order of $k_0 d$ is given by

$$\begin{aligned}\frac{\partial\,\Phi_{z,TM}(z=0)}{\partial q_t}\Big|_{q_t=0} \doteq & -k_0 d\frac{\epsilon'^2-\epsilon'+2}{2\,\epsilon'} \\ & +(k_0 d)^3\frac{(\,\epsilon'-1)^2(3\,\epsilon'^2+5\,\epsilon'+6)}{24\,\epsilon'},\end{aligned} \tag{3.4}$$

which must be positive for real image formation. If we only consider the first term in Eq. (3.4), negative permittivity of the slab ($\epsilon' < 0$) will be the only prerequisite condition for real image formation, which is possible using metals such as silver at UV frequencies. However, considering the higher order term with opposite sign in Eq. (3.4) denotes that the thickness increase of a negative permittivity layer generally oppose the necessary phase condition for making a flat lens. This correlation between the layer thickness

and the real paraxial image formation explains why the thick silver layer in [11, 53] did not achieve super-resolution imaging, whereas the thinner silver layers in later attempts did [10, 50, 54].

3.5.2 Flat Lens for TE Polarization

Having the analytical expression of the transmission coefficient $\underline{t}$ for TE polarization enables the derivation of another general flat lens condition for a TE-polarized wave. Under the thin-film and paraxial approximations, the flat lens criterion of a lossless layer for TE polarization is given by

$$\frac{\partial\,\Phi_{z,TE}(z=0)}{\partial q_t}\Big|_{q_t=0} \doteq -k_0 d\frac{3-\epsilon'}{2} - (k_0 d)^3\frac{(\epsilon'-1)^2(3\,\epsilon'-1)}{24}. \tag{3.5}$$

If we only consider the first term of Eq. (3.5), imaging with a single flat layer would be possible when $\epsilon' > 3$, a condition that can be fulfilled by many types of glasses and semiconductors. As TM polarization, the higher order term for TE polarization (Eq. 3.5) plays a crucial role when the layer is not sufficiently thin.

To investigate the new flat lens condition for TE polarization, we study a high-index dielectric ($n = 4$) layer with the nominal thickness of 50 nm placed in air and illuminated by a TE-polarized wave of free-space wavelength $\lambda_0 = 365\,\text{nm}$. A real paraxial image location of $s = 2\,\text{nm}$ was predicted based on the PSF phase analysis. Figure 3.6(a) shows the phase at the image plane location.

We then conduct two distinct FDFD simulations with and without the dielectric layer for imaging near diffraction limit spaced objects. An image of these objects at the paraxial image location is formed by adding the dielectric layer as shown in Figure 3.6(b), where the electric energy density profile for both configurations at the image plane location are plotted. The full-wave FDFD simulations in Figs. 3.6(c) and (d) further demonstrate the capability of a dielectric layer to form a near-field image of near diffraction limit spaced objects in case of TE polarization. The yellow dashed line in Figure 3.6(d) shows the consistency between simulation and small-angle phase prediction.

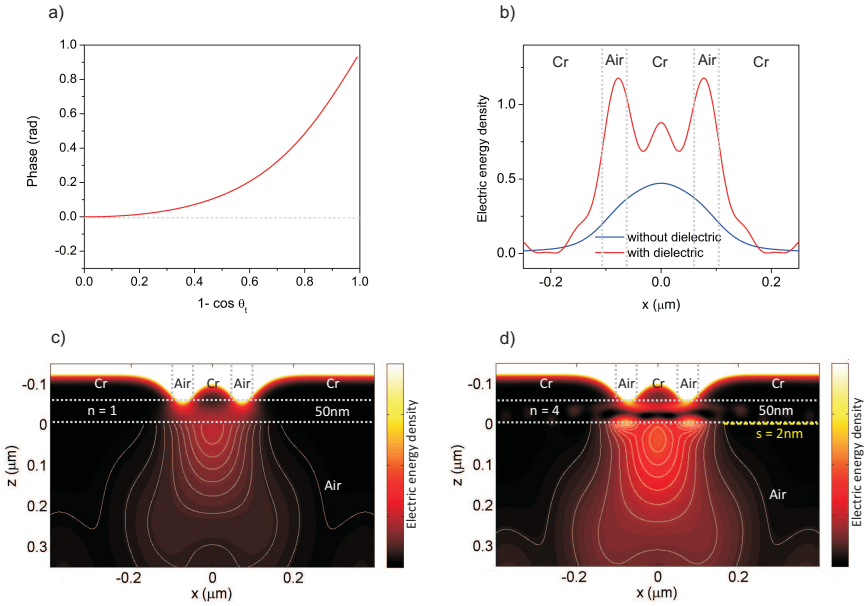

Figure 3.6: Flat lens for TE polarization based on a 50- nm-thick lossless dielectric ($n = 4$) layer immersed in air and illuminated at a wavelength $\lambda_0 = 365\,\text{nm}$. (a) PSF phase at the paraxial image location $s = 2\,\text{nm}$. (b) FDFD-simulated profile of the electric energy density at the paraxial image location for the cases where the object is imaged without (blue) and with (red) the dielectric slab. Simulated time-averaged electric energy density distributions of the illuminated object are shown (c) without and (d) with the 50-nm-thick dielectric layer. The yellow dashed line in each panel shows the paraxial image location calculated by the PSF phase. [4]

3.6 Flat Lens Condition for Multi-layers

For a more general case of multi-layer system, we derive the condition for flat lens imaging and we show that it is identical to the used condition for making bi-layer anisotropic metamaterial lenses. The flat lens criterion based on Eq. (3.3) for a multi-layer system using a TM-polarized wave is approximately

$$\frac{\partial\,\Phi_{z,TM}(z=0)}{\partial q_t}\Big|_{q_t=0} \doteq -k_0 \sum_i d_i \left(\frac{1}{2}(\,\epsilon_i' - 1) + \frac{\epsilon_i'}{|\,\underline{\epsilon}_i|^2}\right) \quad , \tag{3.6}$$

where d_i and $\underline{\epsilon}_i = \epsilon'_i + \epsilon''_i$ are respectively the thickness and the permittivity of the i^{th} layer.

We now consider the simplest multilayer system with a single bi-layer unit cell of metal and dielectric with dielectric parameters of d_D and ϵ_D, and metal parameters of d_M and $\underline{\epsilon}_M$. If the metal permittivity is complex where $\underline{\epsilon}_M = \epsilon'_M + \epsilon''_M$, the required dielectric permittivity condition for projecting a real image across the unit cell is given by

$$\epsilon_D = \frac{1}{2} - \frac{d_M\,\underline{\gamma}_M}{d_D} \pm \sqrt{\left(\frac{1}{2} - \frac{d_M\,\underline{\gamma}_M}{d_D}\right)^2 - 2} \quad , \tag{3.7}$$

where $\underline{\gamma}_M = (\epsilon'_M - 1)/2 + \epsilon'_M/|\underline{\epsilon}_M|^2$. Eq. (3.7) can be simplified to $\epsilon_M/\epsilon_D = -d_M/d_D$ and $\epsilon_M + \epsilon_D = 1$ when the metal permittivity is real and large ($\epsilon'_M >> 1$) and the thicknesses of the metal and dielectric layers are comparable ($d_M \approx d_D$). These simplified conditions are identical to the defined constraints based on the effective medium theory for designing a flat lens made of metamaterial with an anisotropic permittivity tensor [6].

3.7 Broadband Flat Lens Designed by Small-angle Phase

We systematically design a bi-layer system that can consistently project the image at particular location using a TM-ploarized wave with broadband wavelength spectrum of a large portion of the ultraviolet-visible. The design is based on using the paraxial image location in Eq. (3.1) as a merit function for an optimization routine.

Silver-gold bi-layer system is found to be a practical result of this design process, where the thicknesses are 28 nm and 29 nm respectively. Over a large spectral range ($365\,\text{nm} < \lambda_0 < 455\,\text{nm}$), the paraxial image location of the bi-layer flat lens stays comparatively stable between 35 nm and 37 nm (Fig. 3.7 (a)). The amplitude and phase of the PSF at the paraxial image location of $s = 37\,\text{nm}$ and for the wavelengths of $\lambda_0 = 365\,\text{nm}$ and $\lambda_0 = 455\,\text{nm}$ are shown in Figure 3.7(b). The response modeling of the bi-layer system at the lower and upper bounds of the considered wavelength range reveals the analogy between the energy density concentrations near the predicted paraxial image locations of 37 nm as shown by the full-wave electromagnetic simulations in Figure 3.7(c) and (d). Unlike other near-field flat lenses, the formed near-field image by the bimetallic broadband lens cannot resolve the two openings of the near diffraction limit spaced objects. This loss of reso-

lution can be attributed to the compounded light interference and metallic losses due to the addition of the gold layer.

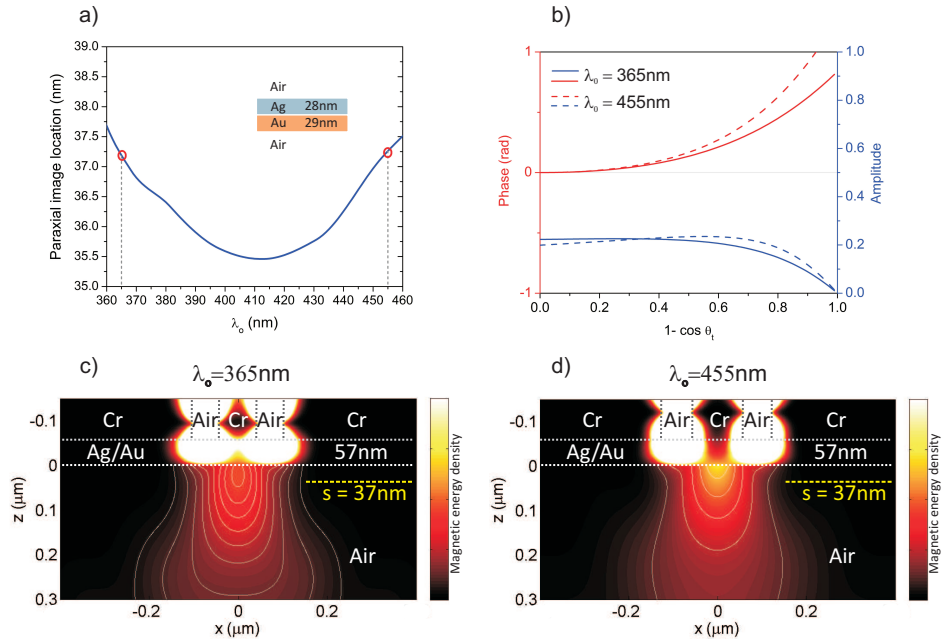

Figure 3.7: Engineering a broadband flat lens. (a) Paraxial image location over the ultraviolet-blue spectrum for a bi-layer flat lens consisting of a 28-nm-thick silver layer and a 29- nm-thick gold layer immersed in air. (b) PSF phase (red) and amplitude (blue) at the image plane location ($s = 37\,\text{nm}$) of the bi-layer flat lens at the wavelengths of $\lambda_0 = 365\,\text{nm}$ (solid lines) and $\lambda_0 = 455\,\text{nm}$ (dashed lines). Time-averaged energy density distributions for the bi-layer system under plane-wave illumination at (c) $\lambda_0 = 365\,\text{nm}$ and (d) $\lambda_0 = 455\,\text{nm}$. The yellow dashed line in each panel shows the paraxial image location calculated by PSF phase. [4]

3.8 Far-field Immersion Flat Lens

One of the most challenging tasks in designing flat lenses is boosting the paraxial image location and projecting the image at far-field, which is essential for imaging three-dimensional objects . Here, we apply a simple technique to further extend the image location of the multi-layer far-field flat lens studied in [7] by increasing the dielectric permittivity of the image

region material.

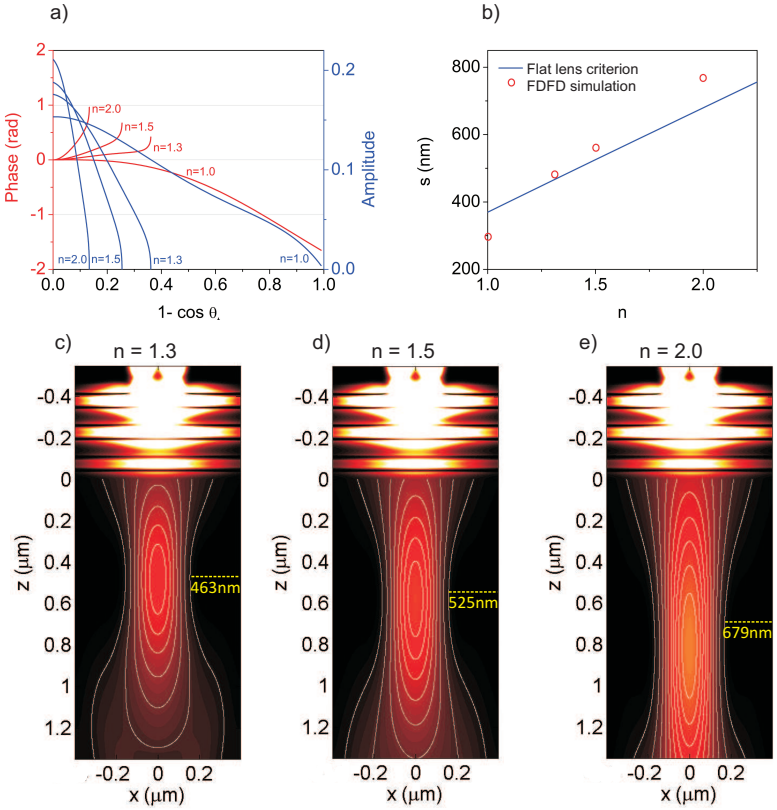

Figure 3.8: Enhancing the image plane location of the multi-layered flat lens system previously studied in [7] by immersion of the image region in a dielectric. (a) PSF phase (red) and amplitude (blue) at the paraxial image location for the cases where the dielectric medium has refractive index $n =$ 1.0, 1.3, 1.5, and 2.0. (b) Paraxial image location versus the refractive index of the dielectric medium predicted by PSF phase (blue line) and FDFD simulations (red circles). (c), (d), and (e) show FDFD-calculated magnetic energy density distributions of the immersed flat lens system for $n = 1.3$, 1.5, and 2.0, respectively. The yellow dashed lines in panels (c)-(e) show the paraxial image location calculated by PSF phase. [4]

As the dielectric permittivity or refractive index increases, the predicted paraxial image location of the far-field flat lens system linearly escalates as shown in Figure 3.8(b). The full-wave simulations in Figures 3.8(c), (d) and

(e) visually demonstrate this effect where the separation distance between the maximum energy density spot in the image region and the exit of the lens increases as the dielectric permittivity of the image region is augmented. The positions of the maximum energy density spot obtained from simulations are quite consistent with the paraxial image locations predicted by the phase of the PSF as shown in Figure 3.8(b). Although the dielectric immersion method provides a premium method to enhance the working distance of flat lenses, it increases abberations at the image plane location as shown by the plotted PSF phase and amplitude at the paraxial image location for various refractive index values (Fig. 3.8(a)).

3.9 Summary

We have promoted a general flat lens criterion based on the small-angle phase behaviour for flat lens structures that are composed of a single or multiple layers of homogeneous isotropic media. This criterion showed to be consistent with the far-field flat lens implementation studied in [7], and more interestingly the super resolution near-field flat lenses presented in [6, 10, 11, 13, 50]. The Analytical expressions of the flat lens criterion for single and multi-layer systems provide a single metric for predicting real image formation. Designing a flat lens for TE polarization which is capable of imaging slightly below the diffraction limit, a broadband flat lens that works over part of the UV-visible spectrum, and an immersion flat lens with an adjustable far-field paraxial image location up to several wavelengths from the exit surface are the novel outcomes of the proposed flat lens criterion.

Chapter 4

Transparency of Thin Layers: Light Transparency Boost by Opposite Susceptibility Coating

In this study, we examine optical light transmission through metal-dielectric bilayer systems. It has been shown before that dielectric coating of metallic films can enhance light transmission through metals. However, here we show that in theory the transmission enhancement phenomenon in metal-dielectric systems is reciprocal, where the transparency of a dielectric layer can be increased by adding a very thin metallic layer. In a general sense, coating a thin base layer with another thin layer of opposite susceptibility sign can make the base layer more transparent. To experimentally validate the proposed light transmission hypothesis, we measure the transmitted light through dielectric-coated silver films and silver-coated silicon nitride membranes and we found that experimental measurements are favorably comparable to the theoretical calculations. We particularly show that the optical transparency of a silicon nitride membrane can be enhanced over a narrow-band of the visible spectrum by the addition of a thin silver layer. This study can be considered as the first work that demonstrate the reciprocity concept with respect to light transmission enhancement in metal-dielectric bilayer systems.

4.1 Theory

Considering the bi-layer configuration in Figure 4.1(a) and based on the standard transfer matrix methods [42], the transmittance T of a normally incident monochromatic plane wave from the left half-space onto the bilayer at frequency ω has the general form

$$T = f(k, \underline{\epsilon}_i, \underline{\epsilon}_t, \underline{\epsilon}_1, \underline{\epsilon}_2, d_1, d_2), \tag{4.1}$$

where d_1, $\underline{\epsilon}_1$, $\underline{\chi}_1$, and $\underline{n}_1$ are respectively the thickness, the complex permittivity, the complex susceptibility, and the complex refractive index of the first layer or the base layer. In the case of oblique light incidence, light transmittance will be a function of the same parameters beside the angle of light incidence and we will not get the maximum light transmission due to the presence of surface waves.

Similarly, the properties of the second layer or the coating layer are denoted by d_2, $\underline{\epsilon}_2$, $\underline{\chi}_2$, and $\underline{n}_2$. The permittivity values of both layers are allowed to be complex where they have the general form of $\underline{\epsilon} = \epsilon^{'} + i\epsilon^{''}$. The left and right half-spaces have the dissimilar real permittivity values of ϵ_i and ϵ_t, respectively, and the free-space wave number is defined by $k = \omega/c$ where ω is the angular wave frequency and c is the speed of light.

In the limit where the thickness of the coating layer d_2 goes to zero, a simplified condition for transmission enhancement can be derived from the transmittance partial derivative with respect to d_2. Assuming high figures of merit for both base and coating layers where complex permittivities are predominantly real such that $\left|\frac{\epsilon_1^{'}}{\epsilon_1^{''}}\right| \gg 1$, and $\left|\frac{\epsilon_2^{'}}{\epsilon_2^{''}}\right| \gg 1$, the transmission enhancement condition will be given by

$$sgn\left(\frac{\partial T}{\partial d_2}|_{d_2=0}\right) \equiv sgn\Big(-(\epsilon_1^{'} - \epsilon_i)(\epsilon_2^{'} - \epsilon_t)\Big) > 0. \tag{4.2}$$

If the bi-layer is immersed in air ($\epsilon_i = \epsilon_t = 1$), the transmission enhancement condition can be simplified to a function of the real susceptibilities of the base and coating layers where $\chi_1\ \chi_2 < 0$.

This condition distinctly shows that independent of the layer ordering sufficiently thin bi-layers with opposite susceptibilities are more transparent than the individual layers alone. To achieve the highest light transmission, the optimal coating layer thickness should satisfy the following equation

$$tan(2\varphi_2) = \frac{2n_1n_2\ sin(2\varphi_1)(\epsilon_1^{'} - 1)}{(\epsilon_1^{'} - \epsilon_2^{'})(1 + \epsilon_1^{'}) + (1 - \epsilon_1^{'})(\epsilon_1^{'} + \epsilon_2^{'})\ cos(2\varphi_1)}, \tag{4.3}$$

where any permittivity that satisfies Eq. 4.2 is permissible to be used in Eq. 4.3, and the angle parameters φ_1 and φ_2 are defined as $\varphi_1 = n_1kd_1$ and $\varphi_2 = n_2kd_2$, respectively.

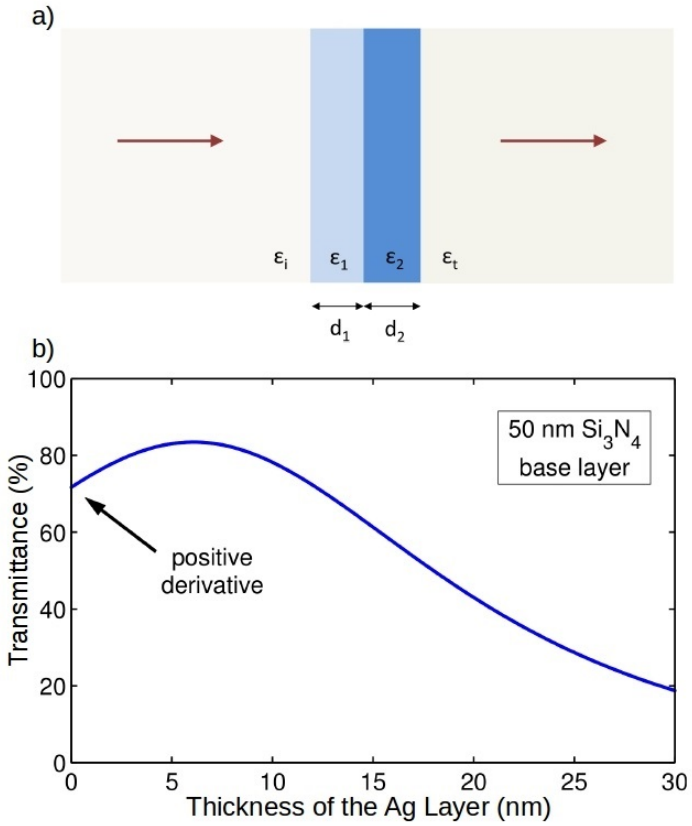

Figure 4.1: (a) Ideal configuration of a bi-layer immersed in two half-spaces, illuminated at normal incidence from the left half-space. (b) Predicted normal-incidence transmittance at a wavelength of 650 nm through a bi-layer composed of a 50-nm-thick base layer of silicon nitride and a coating layer of silver of variable thickness. A positive derivative of the transmittance in the limit of zero coating layer thickness can be used as an indicator of transmission enhancement. [14]

From Eq. 4.2, the permittivities of the base and coating layers should satisfy either of the following inequalities

$$\epsilon_1^{'} < 1 < \epsilon_2^{'} \quad or \quad \epsilon_1^{'} > 1 > \epsilon_2^{'} \tag{4.4}$$

The practical implementation of the first condition in (4.4) is the well-

examined configuration of a metallic layer coated with a dielectric layer. The second condition in (4.4) can be related to the configuration of a dielectric layer coated with a metallic layer, which has not been investigated yet.

Although the metal-coating dielectric layer configuration for the purpose of light transmission enhancement is counter-intuitive, here we show that it can be described by a full solution of Maxwell's equations. Assuming that the dielectric base layer is a 50-nm-thick silicon nitride and the metal coating layer is silver, we calculate and plot the percentage normal-incidence transmittance of the bi-layer system at a wavelength of 650 nm as the thickness of the silver coating layer is increased from 0 nm to 30 nm (Fig. 4.1(b)). According to this illustration, a maximum transmission boost of 10% can occur when the thickness of the silver layer is 6.1 nm.

In these calculations, the silicon nitride's optical constants are taken from [172]. Although the permittivity of very thin metals is affected by the electron scattering at the surface, we used the complex optical constants of bulk silver [17] in the illustrated calculations in Figure 4.1(b). For more accurate results, the optical constants of thin metal films should be measured and used in future works. The optimal silver layer thickness of 6.1 nm obtained from Figure 4.1(b) is comparable to the optimal thickness of 6.4 nm extracted from Eq. 4.3. The slight discrepancy is due to the neglect of silver layer losses in Eq.4.3.

In general, when we have a very thin dielectric layer with the base layer thickness less than a quarter of a wavelength, the transmissivity of light through the dielectric layer increases as we reduce the dielectric layer thickness. This work introduces another way for light transmission enhancement through thin positive susceptibility dielectric layers by addition of a negative susceptibility (NS) layer. Pairing a thin dielectric layer with a NS layer can reduce the effective optical path length of the dielectric layer and resulting in increased transmission as if the layer thickness were reduced.

4.2 Methodology

We examine the optical transmission enhancements due to combinations of metallic and dielectric layers by first fabricating thin film samples of different materials based on their properties in the visible region. We prepared metal, metal-oxide, and elemental semiconductors samples using the magnetron sputter deposition (Angstrom Engineering Nexdep). The metal films are made of silver with target purity of 99.99%, the metal-oxide films are sputtered from a titanium dioxide target (99.9%), and the elemental semi-

conductors are deposited using the targets of undoped silicon, boron-doped p-type silicon, and germanium, where all the semiconductor targets have the similar high purity of 99.999%. Silver has been selected among common metals due to its highest figure of merit as well as its real negative susceptibility. As for other materials, TiO_2 has a high figure of merit, a real, positive susceptibility, and high chemical stability; Si and Ge have modest figures of merit, real, positive susceptibilities, and can be tuned by impurity doping. All these materials are compatible with physical vapor deposition.

The films are made at room temperature when the base vacuum pressure of the deposition chamber reaches at least $\sim 5.0 \times 10^{-5}$ torr and the argon gas pressure is about 3.0×10^{-3} torr. Depositing at moderate rates, the dielectric and silver films are deposited at 1.0 $\mathring{A}/s$ and 2.0 $\mathring{A}/s$, respectively. The rotating platform that holds the substrates is spaced about 20 cm above the 5-cm-diameter targets.

To test transmission enhancement, two families of samples are made. One for testing the transparency enhancement by dielectric coating and the other one based on metallic coating. For the first family of samples, all samples are sputtered on borosilicate glass substrates. The sputtered base layers are made of silver and the sputtered coating layers are made of either TiO_2, Si, p-Si, or Ge. Five samples are made for each type of coating layer where the dielectric coating layer thickness varies from 18 nm to 60 nm while the silver base layer thickness is fixed. A well-established method for realizing transparent conductors is coating silver films with TiO_2 [69], which is considered as benchmark in this study. Although the effects of semiconductor coatings like Si or Ge on the transparency enhancement of silver films have yet to be investigated, relevant studies have examined substrates of optically-thick metals coated with very thin layers of Si and Ge from which a wide range of reflected colors is visible [173–176].

For the other family of samples where a dielectric layer is coated with metal, a free-standing silicon nitride membrane is used as the base layer because transmission enhancements in a metal-coated dielectric layer are estimated to be most prominent when it is bounded by air. The free-standing silicon nitride membrane is 50-nm-thick with the dimensions of 0.5 mm $\times$ 0.5 mm, manufactured by SPI Supplies. According to the manufacturers specifications, the surface roughnesses for all membrane samples are better than 0.5 nm root mean squared, and the thickness variation between different membrane samples is less than 5 nm. The silicon nitride membrane base layer is sputter-coated by a very thin silver layer.

The metal film growth process in general starts by the formation of small islands that overlap as deposition continues. For very thin metal films, when

the islands are just interfered, the metal films will have the maximum surface roughness and the utmost surface contact area with atmosphere which can significantly increase the oxidation rate of metals. Therefore, to prevent atmospheric corrosion, in some cases, the ultra-thin silver coating layer is passivated by an additional sputtered layer of TiO_2.

The quartz crystal monitoring system in the sputtering deposition station is calibrated and used to measure the thicknesses of the deposited films. The calibration was conducted by using the stylus-based profilometer (KLA Tencor Alphastep) to measure the thicknesses of a series of thin-film samples of different materials with variable deposition thicknesses.

The visible and infrared light transmission measurements (400 nm to 1800 nm) of the dielectric-coated silver films is conducted using a Filmetrics F20 analyzer system, while the visible spectrum transmission measurements (400 nm to 750 nm) of the silver-coated membranes is performed in a confocal setups to suit the small aperture of the membranes using a Schott-Fostec DDL fiber optic non-plane wave light source connected to an Ocean Optics USB4000 spectrometer. Under the coherent laser illumination of various wavelengths (365 nm, 470 nm, 590 nm), the microscopically zoomed in transmission images of silver-coated membranes are collected by a Zeiss Axioimager microscope and captured by a monochrome CCD camera.

4.3 Results and Discussion

Silver coated with a film of high-index, low-loss dielectric, such as TiO_2, have been shown to be the most pronounced recipe for light transmission enhancement through silver. The photographs and the normalized transmittance spectra of the TiO_2-coated silver films and the uncoated sample are shown in Figure 4.2(a). The measured spectral intensities transmitted through the sample $I(\lambda)$ are normalized to that of air $I_o(\lambda)$, where the normalized transmittance spectra can be expressed as $I(\lambda)/I_o(\lambda)$. While bare silver has the transmittance spectrum that consistently decays from blue to red, addition of a TiO_2 coating produce a transmittance peak within a band known as transparency band at a wavelength dependent on the coating thickness. Varying the coating thickness from 18 nm to 57 nm, the peak wavelengths of the transparency bands shift from $\sim$400 nm to $\sim$780 nm. The photographs of the fabricated samples visually exhibit group of colors including light blue, greenish blue, yellow, and brown. This range of colors is the consequence of the shift in the maximum light transmission peak along the visible wavelengths as we increase the coating layer thickness.

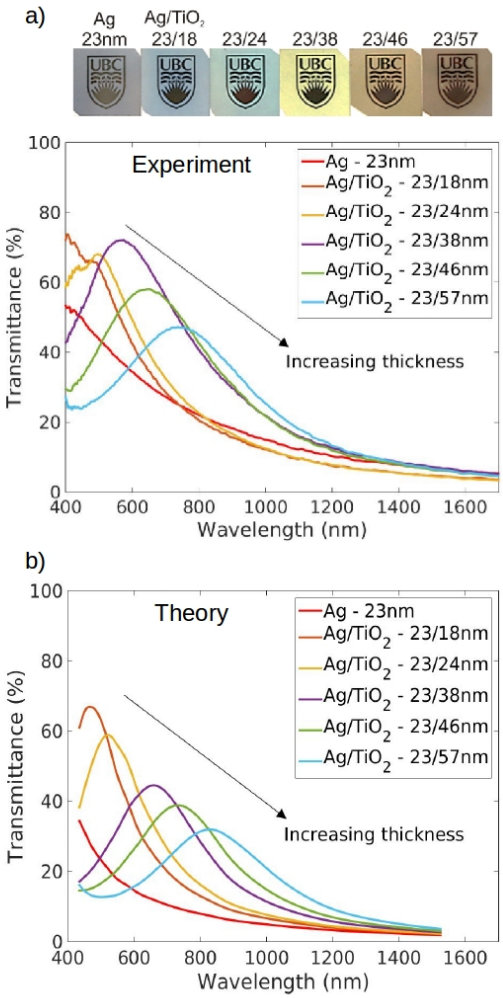

Figure 4.2: Changing the optical properties of semi-transparent silver by sputtered TiO_2 coatings. (a) Experimental and (b) calculated normal-incidence transmittance spectra for 23-nm-thick silver layers that are either uncoated or coated with a TiO_2 layer ranging in thickness from 18 nm to 57 nm. The experimental spectra are obtained from the average of 5 independent measurements, where each measurement is made from an average of 40 traces. Photographs of the samples placed on the printed UBC logo are shown at the top of panel (a) to highlight the visible appearance changes caused by the thin TiO_2 layer. The leftmost photograph is of uncoated silver and the adjacent images are of coated silver (in order of increasing coating layer thickness from left to right). [14]

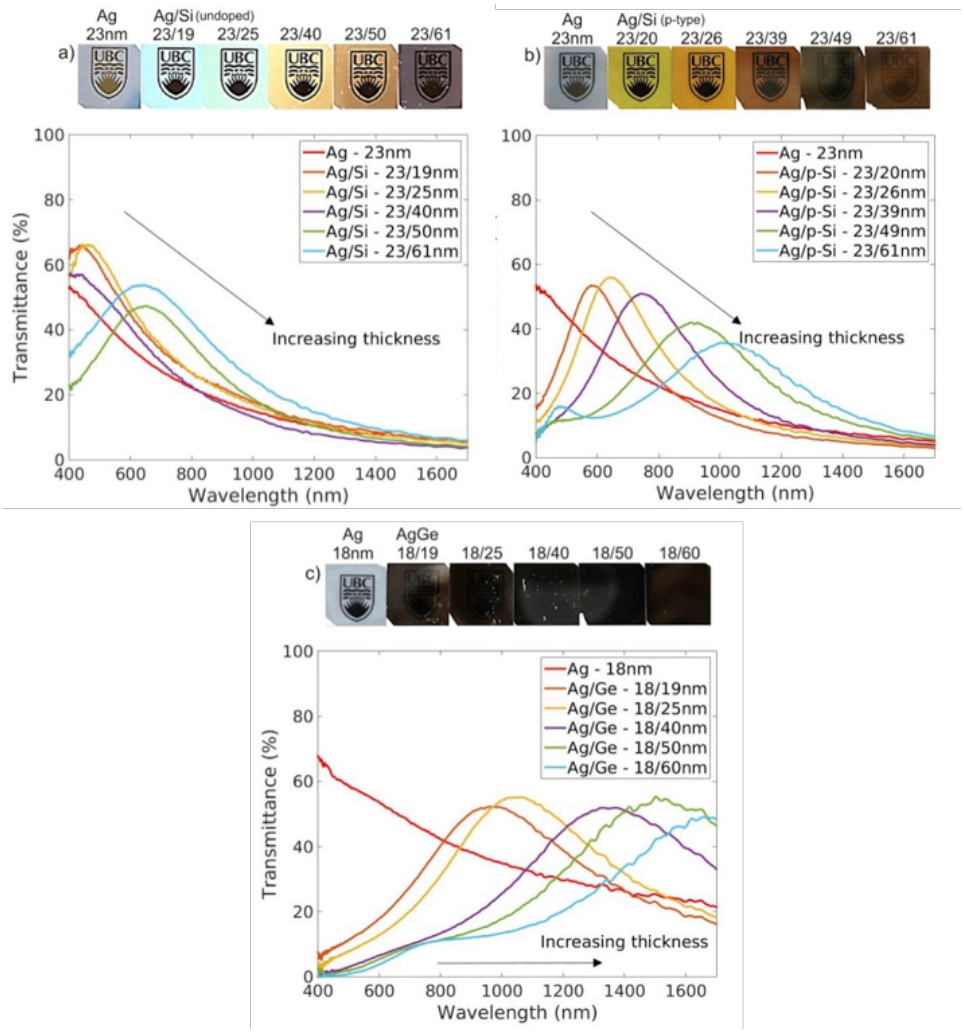

Figure 4.3: Changing the optical properties of semi-transparent silver by various sputtered elemental semiconductor coatings. Experimental normal-incidence transmittance spectra for (a) 23-nm-thick silver coated with sputtered silicon, (b) 23-nm-thick silver coated with sputtered p-type silicon, and (c) 18-nmthick silver coated with sputtered germanium. The experimental spectra are obtained from the average of 5 independent measurements, where each measurement is made from an average of 40 traces. Photographs of the samples placed on the printed UBC logo are shown at the top of each corresponding panel to highlight the visible appearance changes caused by the thin layers. [14]

a)

λ (nm)	Average normalized transmittance			
	Bare	Ag coated	Ag/TiO_2 coated	Ag/TiO_2 coated x2
400	81.8 ± 0.7	87.5 ± 0.4	86.2 ± 0.4	85.6 ± 0.4
420	72.0 ± 1.0	72.1 ± 1.4	74.4 ± 0.2	75.0 ± 0.4
440	67.6 ± 0.6	64.8 ± 2.4	68.3 ± 0.2	67.8 ± 0.3
460	63.0 ± 0.3	57.2 ± 3.4	61.9 ± 0.3	59.6 ± 0.2

b)

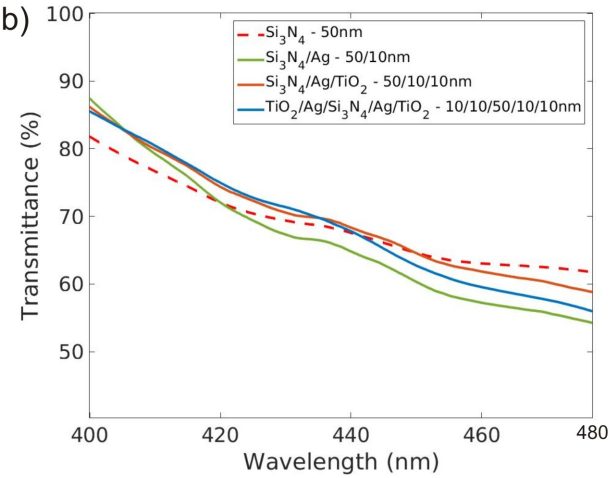

Figure 4.4: Experimental measurements of the transmission enhancement of a 50-nm-thick silicon nitride membrane conferred by coating the membrane with 10-nm-thick silver layers in three different configurations: single-sided coating with silver, single-sided coating with silver followed by a 10-nm-thick TiO_2 passivating layer, and double-sided coating with passivated silver. (a) shows tabulated the average normalized transmittance values for the bare membrane and the three silver-coated membranes at the wavelengths of 400 nm, 420 nm, 440 nm, and 460 nm. Cells in the table corresponding to transmission enhancement (beyond experiment error) are shaded green. (b) shows the average transmittance spectra for the bare membranes (red dashed), the membrane that is coated on a single side by silver (green line), the membrane that is coated on a single side by passivated silver (orange line) and the membrane that is coated on both sides by passivated silver (blue line). The error has a magnitude comparable to the line widths and has not been explicitly plotted for clarity of presentation. [14]

As shown in Figure 4.2(b), the experimental data are quite consistent with our theoretical calculations which are based on solving the transfer functions and calculating the transmitted light through ideally planar layered media with optical constants taken from [17] and [177] for silver and TiO_2, respectively. The nominal variations between the peaks of the measured and calculated transparency bands can be due to the discrepancies between the actual and assumed optical constants of silver and TiO_2, as well as the surface roughness of the films which is neglected in the model.

We show that coating silver with semiconductors can also boost transmission and form transparency bands. The photographs and the normalized transmittance spectra of bare silver films and coated ones with sputtered Si, p-Si, and Ge are shown in Figure 4.3. The induced visible-frequency transparency bands of the sputtered Si samples are interestingly analogous in magnitude and spectral position to those caused by sputtered TiO_2. Hence, in applications such as transparent conductors or metal-based heat-reflecting windows, sputtered Si coating can be proposed as an alternative to sputtered TiO_2. The transparency bands made by the sputtered p-Si samples lie over the visible range between the free-space wavelengths of ∼600 nm and ∼1100 nm, while those made of sputtered Ge spread completely outside the visible spectrum between ∼900 nm and ∼1800 nm. The distinct spectral variations between Si-coated and Ge-coated samples are due to the large index differences between bulk Si and Ge.

On the other hand, the evident spectral variations between Si-coated and p-Si-coated samples can be surprisingly attributed to the slight index differences between bulk Si and p-Si. This observation suggests further investigation on the authenticity of using the optical constants of bulk p-Si for the sputtered p-Si. The illustrated spectral transmittance in Figure 4.3 show the capability of tailoring the induced transparency bands of silver-coated films across the entire visible and near-infrared using three different types of semiconductors. Although this semiconductor coating method can be useful for fabricating absorbers, optical filters, or solar cell coatings, the accuracy of theoretically modeling such sputtered simiconductors (Si, p-Si, Ge) is limited by the high dependence of their optical properties on growth conditions [178, 179] which is not well-characterized.

In the next experimental part of this work, we examine the 50-nm-thick silicon nitride membrane samples to show the capability of transmission enhancement through membranes by sputtered silver coating. The table of average normalized transmittance of bare and coated silicon nitride membrane samples in the blue and green parts of the visible spectrum is shown in Figure 4.4. It includes the numerical transmittance of a bare membrane

as control spectra, a membrane with single-sided silver coating, a membrane with single-sided silver coating passivated by TiO_2, and a membrane with double-sided passivated silver. The thickness of the silver coating layer is chosen based on the deduced information from the scanning electron microscope images which characterizes the minimum thickness at which sputtered silver can form a continuous film around 10 nm.

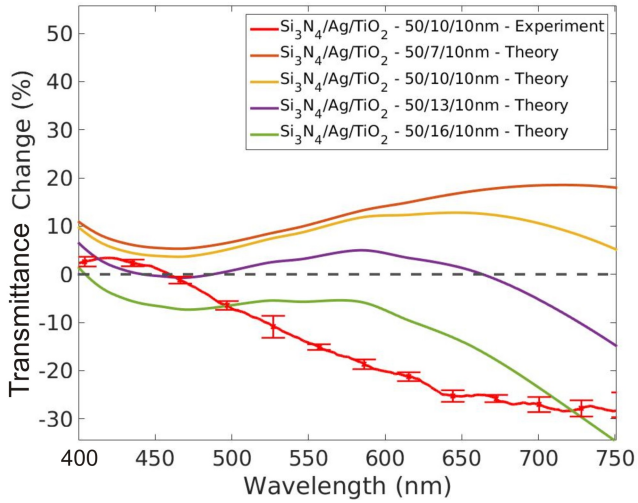

Figure 4.5: Experimental transmittance change over the entire visible spectrum for a 50-nm-thick silicon nitride membrane coated with a 10-nm-thick silver layer that is passivated by a 10-nm-thick TiO_2 layer (red line with error bars). Also shown are calculations of the transmittance change for the three-layer system assuming various silver layer thicknesses. The error bars in the experimental measurement represent one standard deviation. [14]

To mitigate sources of uncertainty, the spectra are averaged across many measurements. To mitigate thickness variations across membrane samples, the control transmittance spectra are averaged over measurements of three distinct bare membranes. To mitigate local thickness variations of a given membrane, the transmittance spectra are averaged over measurements taken at 10 different locations on the membrane. To account for random noise from the light source and spectrometer, the transmittance spectrum is averaged over 150 measurements for all measurements at each location. As demonstrated in Figure 4.4, the spectral measurements of all three silver-coated

membranes show moderate transmission enhancements in the blue part of the visible spectrum where all transmission boost peaks at 400 nm, the lower wavelength bound of the measurement. The maximum measured enhancement of 6±1% is achieved by single-side silver coating. Silver coated membranes passivated with TiO_2 yields similar transmission enhancements as the non-passivated one, except over a larger wavelength range and with slightly smaller transmission enhancements around the peak values.

Comparing the experimental measurements and theoretical calculations, Figure 4.5 shows the transmittance change measurements of the passivated single-side silver-coated membrane over the full visible spectrum besides the calculated transmittance change for various silver layer thicknesses. The transmittance change describes the measured variations between the transmitted spectral intensities of bare membrane ($I_b(\lambda)$) and silver-coated membrane ($I_c(\lambda)$), where it is defined by $[I_c(\lambda) - I_b(\lambda)]/I_b(\lambda)$. While similar positive transmittance changes can be observed at blue wavelengths between measurements and calculations, they start to diverge at larger wavelengths. This divergence can be attributed to the index differences between bulk and sputtered materials, the consideration of perfectly smooth layers in theoretical calculations, and the possibility of having sputtered layers with nano-thickness variations. The theoretical model, which is based on the ideal conditions of perfect layer planarity and sharp boundaries, predicts greater than 10% transmittance change over the entire visible spectrum using a very thin 7-nm-thick silver coating layer.

According to the model calculations of the silver coated membranes, the enhancement effect is quite dependant on the silver layer thickness where increasing the thickness from 7 nm to 16 nm is sufficient to completely eradicate this effect. The most robust transmission enhancement predictions as a function of the silver thickness are located around the blue part of the spectrum. This observation explains why the measured transmission enhancement is limited to the blue frequency range. Fabricating smoother silver layers will most probably improve the experimental enhancement.

A strategy that can be explored in future for developing smoother silver layers is the addition of a seed layer of germanium or nickel [180, 181] that may also change the optical constants of silver. To show if the transmission enhancement conferred by thin silver coatings is visually observable, comparative microscope images of a bare membrane and an identical membrane coated with 10 nm of Ag and 10 nm of TiO_2 are shown in Figure 4.6, where the membrane samples are illuminated by a normal-incidence laser at wavelengths of 365 nm, 470 nm, and 590 nm.

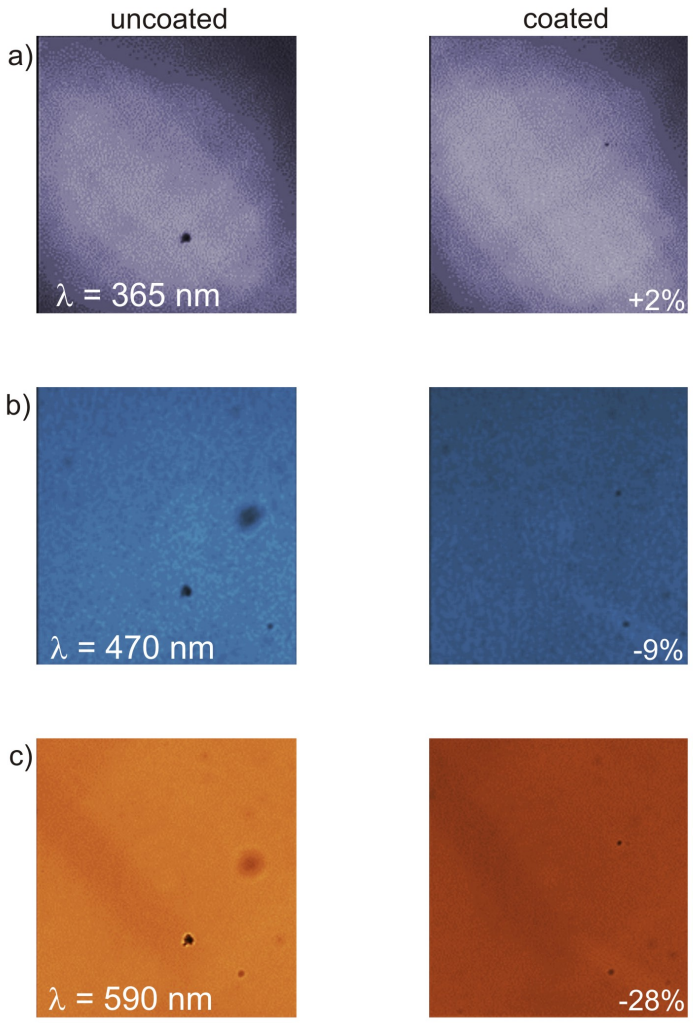

Figure 4.6: Microscope images of (left column) an uncoated 50-nm-thick Si3N4 membrane and (right column) an identical membrane coated with 10-nm-thick Ag and 10-nm-thick TiO_2 under laser illumination at wavelengths of (a) 365 nm, (b) 470 nm, and (c) 590 nm. The images were collected using a monochrome camera and have been false-colored to reflect the color of laser illumination. The percentages on the images in the right column indicate the percent change in the average image brightness relative to the adjacent images in the left column. [14]

At the wavelength of 365 nm below the spectral measurement wavelength limit (400 nm), a modest image brightness increase of about 2% is measurable. In a good agreement with the spectral measurements in Figure 4.5, the images turn dimmer by 9% and 28% at wavelengths of 470 nm and 590 nm.

4.4 Summary

We develop a theory based on Maxwell's equations to generally describe the well-known coating method, which is used specifically to enhance the transmittance of metal films by dielectric coating. The theory include two general conditions, one to determine the possibility of transmission enhancement, and the other one to calculate the optimal thickness of the coating layer. The proposed theory emphasizes that the transmission enhancement effect is not limited to metal films coated with dielectric, but rather any coated material can be made more transparent if the base layer and the coating layer have opposite sign susceptibilities and the appropriate thicknesses.

We conducted two distinct series of experiments that confirm the validity of the introduced theory. In the first set of experiments, we examined silver films coated with a well-explored dielectric (TiO_2) and the less-explored semiconductors (Si, p-Si, Ge). We show up to $\sim$70% light transmission enhancement in the coated silver films where the transmittance can be spectrally tailored depending on the type and thickness of the dielectric coating over the visible and near-infrared part of the spectrum. In the second set of experiments, we investigated the possibility of boosting light transmission through a dielectric layer by metal coating. The transmission measurements of silver-coated silicon nitride membranes show a modest light transmission enhancement of 6 ± 1% in the blue part of the spectrum. Similar transmission enhancements are observed for the passivated single-side and double-side silver-coated membranes.

Chapter 5

Surface Plasmon Resonance: Copper as Good as Gold

Surface plasmon resonance sensing is a well-established method in diverse sensing applications. To enhance the sensitivity of SPR sensors, the SPR coupling efficiency should be improved. For this purpose, various methods like metal thickness optimization [182], dielectric coating [95], nanostructural modification [96, 98–100] and deposition process modulation [102, 103] have been implemented. It has been shown that metals with high figures of merit (low loss) are the best metals for making SPR sensors. Hence, metals like silver, gold, and copper with fairly low loss have been widely used for fabricating SPR sensors. Although copper has the modest price among the three and gold is the most expensive (Cu$\approx$ \$2.7/lb, Ag$\approx$ \$237/lb, Au$\approx$ \$17000/lb), gold continued to be the most preferable metal due to its acceptable SPR performance and chemical stability.

In this work, we introduce copper as a cheaper alternative metal for surface plasmon applications by enhancing the fairly poor SPR coupling efficiency of copper thin films. We examine the influence of different deposition parameters on the SPR couplings of copper, silver and gold thin films, and we find a new DC sputtering deposition recipe for making copper nanofilms with enhanced surface plasmon coupling. Using this deposition recipe, we fabricated 40-nm-thick copper films that have optical resonances comparable to gold. Our method significantly improves the quality factor of the surface plasmon resonance of copper thin films (up to 200% improvement), but shows minimal effect on silver and gold thin films.

5.1 Methodology

We fabricate silver, gold, and copper thin films using the magnetron sputter deposition station (Angstrom Engineering Nexdep) at different slew rates and deposition rates. SPR is measured by recording the intensity of reflected light from a metal film at different angles of incidence. Over a nar-

row range of angles, the reflected intensity shows a sharp and pronounced dip that is an indicative of SPR. We measure the SPR of the fabricated thin films using our home built SPR station which was made based on the Kretschmann's total internal reflection (TIR) coupling method [183], as illustrated in Figure 5.1. The SPR measurements are then qualified based on the SPR parameters: the sharpness and the depth of the SPR dip. The sharper and deeper the dip, the more sensitive the SPR phenomenon becomes.

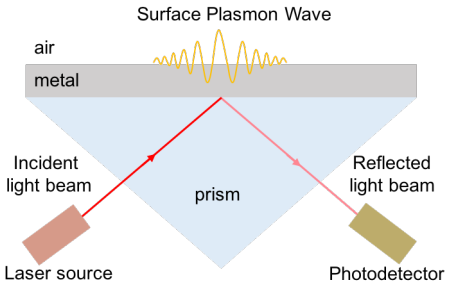

Figure 5.1: Schematic of light coupling to surface plasmon waves using Kretschmann configuration.

The thin film fabrication process starts with a standard glass cleaning method using RO water and acetone to clean the bare glass substrates [184]. The glass substrates are then mounted on a rotating platform spaced about 20 cm above the 5-cm-diameter material source (target). Thin-films of metal are deposited on the cleaned glass substrates from 99.99% metal targets by bombarding the target with Argon ions, as illustrated in Figure 5.2. The magnets on the back of the target are used to discharge the ejected target atoms and start film growth on the glass substrates. All thin films are sputtered at room temperature, where the deposition base vacuum pressure kept to be at least $\sim 5.0 \times 10^{-5}$ torr, and the argon gas pressure 3.0×10^{-3} torr. For optimal SPR responses, we set the thicknesses of all depositions to ∼40 nm for copper [95], and ∼50 nm for gold and silver [182].

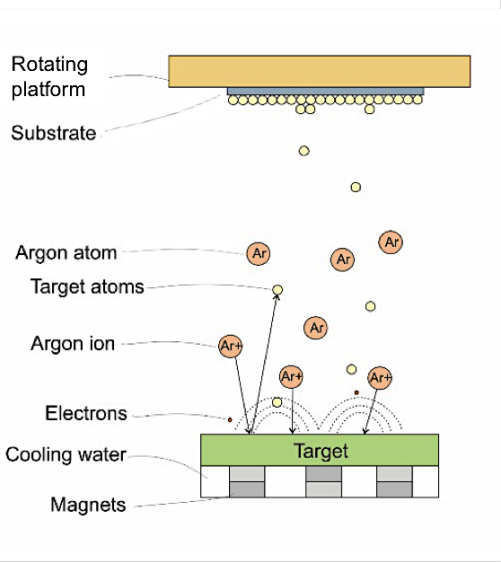

Figure 5.2: Schematic of the sputtering process in the vacuum deposition chamber.

Examining the influence of modifying different deposition parameters on the SPR couplings of copper, silver and gold thin films, we mainly varied two nano-deposition parameters in this work: the deposition rate which is the growth rate of thin films, and the slew rate which is the maximum power change allowed per second controlling the rate of power change on the target. To increase the rate of deposition of our targets, the applied voltage across the targets has to be increased. This will consequently increase the applied power and heat up the target. The required power for reaching certain deposition rate varies from one target to another based on the targets thermal conductivity, thermal coefficient of expansion, mechanical strength characteristics, and melting point. We usually keep an eye on the power applied to the target, but the critical quantity is really the power density, which is the applied power divided by the target's surface area. Since arbitrarily increasing power can cause many adverse effects to the target, we gradually increased the deposition rate of our 2 inch diameter targets to find the maximum safe deposition rates of copper, silver and gold targets at their maximum secure power density. Knowing the maximum safe deposition rates, we sputtered copper and gold at deposition rates as high as 10.0 $\mathring{A}/s$, and silver at higher deposition rates upto 20.0 $\mathring{A}/s$. All depositions are conducted at both low (4.0 $\%/s$) and high (99.9 $\%/s$) slew rates.

The SPR station consists of a BK7 right-angle prism (n = 1.517) mounted on a rotary platform, two HeNe laser sources with yellow (λ_o = 594.0 nm) and red (λ_o = 638.2 nm) operational wavelengths, and a mobile silicon photodetector (DET36A). These two independent laser sources with two different wavelengths are used to confirm the consistency of the proposed method for SPR coupling enhancement in copper films. The glass substrate with metal coating is placed on the back of the prism. The light beam intensity reflected by the installed thin film is detected at various incident angles. A distinct dip in the reflected beam intensity at certain angles is a clear indication of surface plasmon coupling. To account for the non-planarity across metal films, we conduct six reflected intensity measurements at three different sites on each sample.

To compare different SPR spectra measured from different samples, we use the standard quality factor metric of the average reflected beam intensity. The standard quality factor is defined by the ratio of the absorbed peak energy to the peak linewidth, typically the full width at half-maximum [185]. Since we are measuring reflected light rather than absorbed light, the quality factor (QF) will be given by

$$QF = \frac{I_{R,min}}{FWHM}, \tag{5.1}$$

where $I_{R,min}$ is the minimum reflected light intensity and $FWHM$ is the full width at half-maximum of the reflected beam intensity dip. To investigate the morphological cause of the observed SPR enhancement measurements, we take visual photographs, scanning electron microscope (SEM) images, and atomic force microscopy (AFM) images of the silver, gold, and copper films sputtered at different deposition parameters. The photographs are captured in a dark room by a high resolution SLR camera from the same viewing angle and under similar light conditions. The SEM images are taken in high vacuum by a Field Emission Scanning Electron Microscope at 100000x magnification. The AFM images are taken by the Bruker Dimension Icon AFM using the peak force tapping mode over the scan area of 5μm x 5μm.

5.2 Results and Discussions

The intensity measurements of the reflected red laser beam from the fabricated 50-nm-thick silver and gold films at low and high deposition/slew rates show that sputtering rates can play a small but not insignificant role

in changing the SPR quality (Fig. 5.3). Conducting the same measurements for the 40-nm-thick copper films fabricated at low and high deposition/slew rates, we noticed fairly significant improvements in the quality of the SPR dips (depth and acuteness). To clearly demonstrate this prominent SPR response enhancement, we plot copper SPR measurements alongside gold's SPR responses (Fig. 5.4). The measurements are conducted using yellow and red coherent laser sources. Comparing the SPR measurement curves of copper and gold, it can be noticed that SPR responses of copper thin films sputtered at high deposition rates are comparable to gold's SPR responses.

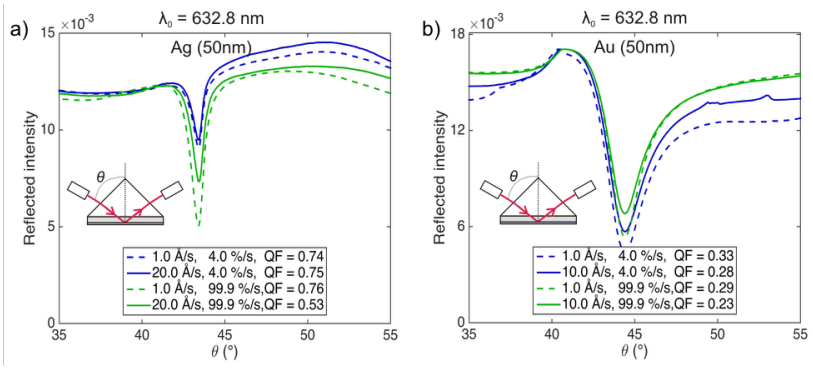

Figure 5.3: Show the SPR measurements of the 50-nm-thick substrates deposited at low and high, deposition/slew rates, for a) silver, and b) gold, using a coherent red He-Ne laser with free-space wavelength $\lambda_o = 632.8$ nm.

To quantitatively compare the SPR responses of silver, copper and gold films made at different deposition/slew rates, we calculate the SPR dip quality factors. We illustrate the calculated quality factors through side by side bars in Figure 5.5. Silver thin films showed to sustain the sharpest dips and the highest SPR quality factors at all deposition/slew rates. The SPR quality factors of gold thin films demonstrate almost constant levels in all situations, whereas the SPR quality factors of copper thin films interestingly exhibit quite large improvements as deposition rate increases.

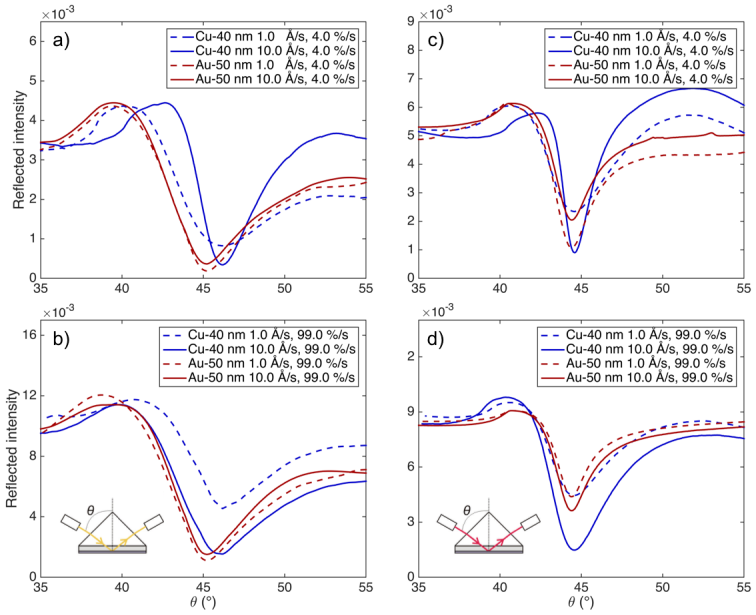

Figure 5.4: Show how the SPR dips of the 40-nm-thick copper (blue lines) become sharper and deeper comparable to the 50-nm-thick gold SPR dips (red lines), when the deposition rate of copper is increased from low deposition rate (1.0 Å/s, blue) to high deposition rate (10.0 Å/s, green). SPR measurements using a coherent yellow $\lambda_o = 594.0$ nm a) b), and red $\lambda_o = 632.8$ nm c) d) He-Ne laser.

In general, it can be observed that the SPR quality factors of copper become comparable to that of gold as we increase deposition rate. For the particular case in which the copper films are made at low slew rate and very high deposition rate and excited using a red laser beam, the SPR quality factors improved by around 200% and reach the highest level ($\sim$0.5), which is better than the best quality factors achieved by gold. The detailed tables of SPR parameters and quality factors are provided in the Appendix.

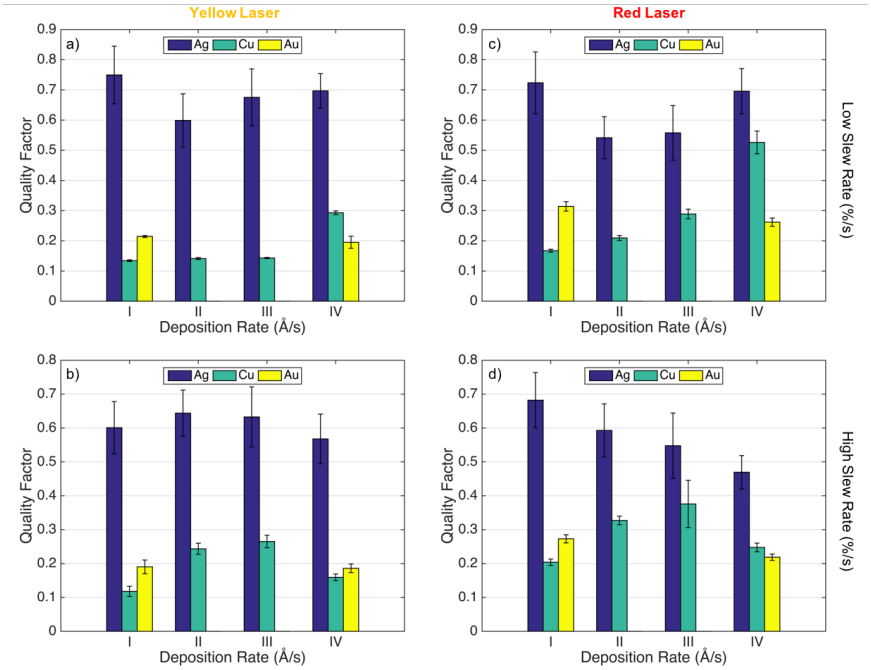

Figure 5.5: The quality factor bar charts with error bars for silver (blue), copper (green), and gold (yellow) at different deposition/slew rates using yellow a) b), and red c) d) lasers. The deposition rates I, II, III, and IV respectively correspond to 1.0 $\mathring{A}/s$, 7.0 $\mathring{A}/s$, 14.0 $\mathring{A}/s$, and 20.0 $\mathring{A}/s$ for silver, and 1.0 $\mathring{A}/s$, 3.0 $\mathring{A}/s$, 7.0 $\mathring{A}/s$, and 10.0 $\mathring{A}/s$ for copper and gold.

To probe the cause of this phenomenon, visual photographs (Fig. 5.6), SEM images (Fig. 5.7), and AFM images (Fig. 5.8) of silver, gold and copper substrates sputtered at different deposition rates and fixed low slew rate are investigated. Looking at the photographs, the two silver substrates (Fig. 5.6 (a), (b)), the two gold substrates (Fig. 5.6 (c), (d)) and the two copper substrates (Fig. 5.6 (e), (f)) look visually identical. As for SEM, we would expect to have different SEM images for copper films rather than silver or gold films due to the differences in copper SPR responses. However, the SEM images show featureless smooth surface for copper thin films (Fig. 5.7 (e), (f)), minimal surface roughness variation for gold thin films (Fig. 5.7 (c), (d)), and diverse surface roughness for silver thin films (Fig. 5.7 (a), (b)) at low and high deposition rates.

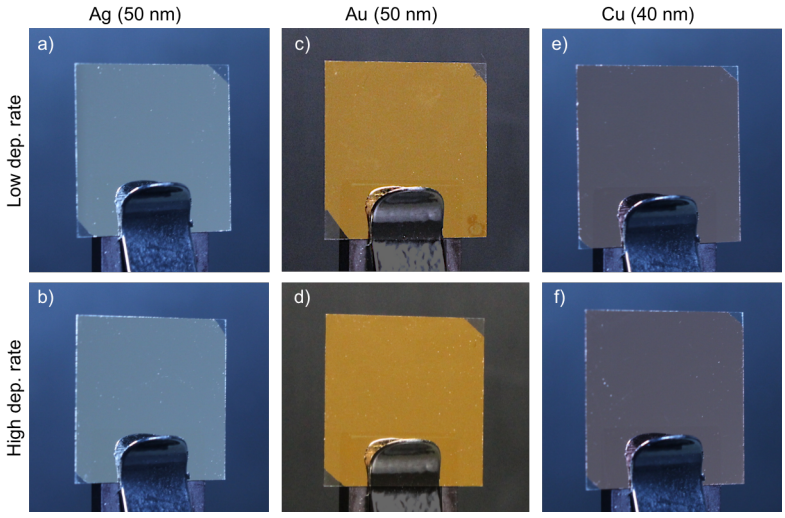

Figure 5.6: Photograph images at low and high deposition rates for the 50-nm-thick silver a) b), the 50-nm-thick gold c) d), and the 40-nm-thick copper e) f) thin films deposited on glass substrates.

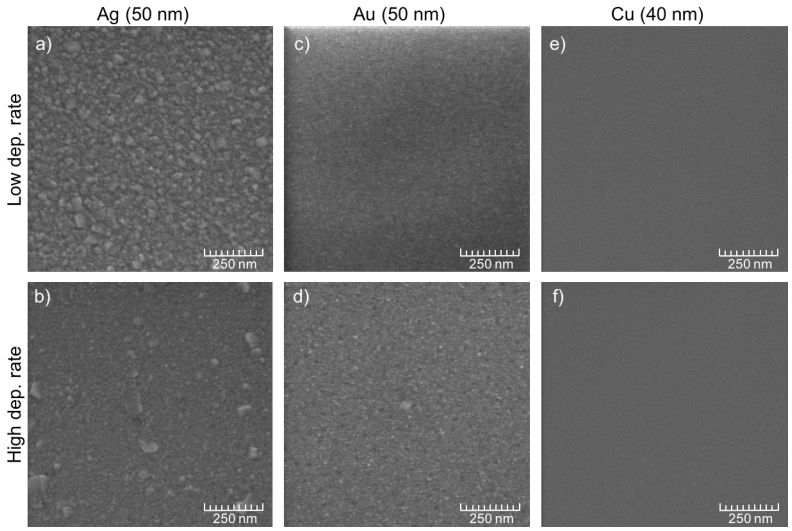

Figure 5.7: Scanning electron microscope (SEM) images at low and high deposition rates for the 50-nm-thick silver a) b), the 50-nm-thick gold c) d), and the 40-nm-thick copper e) f) thin films deposited on glass substrates.

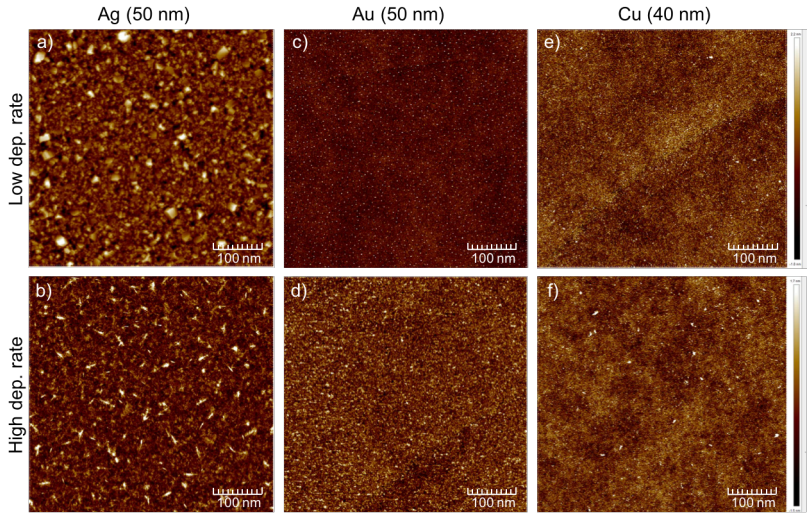

Figure 5.8: The atomic force microscopy (AFM) images at low and high deposition rates for the 50-nm-thick silver a) b), the 50-nm-thick gold c) d), and the 40-nm-thick copper e) f) thin films deposited on glass substrates.

The AFM images show fairly small surface roughness differences between copper films deposited at low and high deposition rates (Fig. 5.8 (e), (f)), and similar surface roughness features for silver (Fig. 5.8 (a), (b)) and gold (Fig. 5.8 (c), (d)). The average surface roughness differences for silver, gold and copper are 5.0 nm, 1.16 nm, and 0.12 nm, respectively. These quite similar SEM and AFM results for copper films deposited at low and high deposition rates suggest that the SPR enhancement effect can be attributed to finer surface features or chemical composition variation. To analyze the chemical composition of the sputtered thin metal films, we used the integrated elemental analysis tool with SEM system (Energy Dispersive Spectroscopy). However, this chemical analysis method cannot provide accurate results since it is based on analyzing the SEM back scattered electrons with quite long penetration effects (around 1 μm), while the maximum thickness of the thin metal films is only 50 nm. For accurate chemical analysis of these thin films, we can try other methods like x-ray photolectron spectroscopy.

5.3 Summary

We have proposed a simple nano-film fabrication procedure to produce copper films with surface plasmon quality factors comparable to gold films.

The considered parameters in this work are the film thickness, the deposition rate and the slew rate. The film thicknesses are fixed to the optimal reported values while the deposition rate and the slew rate are the variable parameters. Experimental results showed significant improvement in surface plasmon coupling performances for copper films deposited with higher deposition rates, while minor enhancement is noticed for silver and gold using the same fabrication process. As the deposition rate increases, the improvement in the SPR quality factors of copper thin films are found to be more consistent and prominent when the depositions are conducted at low slew rates. The maximum measured quality factor improvement of 200% is achieved for copper thin films deposited at low slew rate and the high deposition rate of 10 $\mathring{A}/s$. We believe that replacing of gold films with our modified copper films can significantly reduce the manufacturing cost of commercial SPR sensors.

Chapter 6

Conclusion

This thesis has investigated the interaction of light with sub-wavelength layered systems made of metals and/or dielectrics. Ray optics and the electromagnetic wave theory of light in layered media has been deeply studied before. However, reported observations of the abnormal electromagnetic properties in sub-wavelength layered systems (layered metamaterials), such as negative phase velocity, super-resolution, canalization, and far-field imaging, highlight the necessity of further exploring the intrinsic electromagnetic behaviours of layered metamaterials.

In this thesis, we have discussed the electromagnetic wave theory of layered systems with the practical constraints of loss and finite extent. We have developed the theory and derived a new representation for the electromagnetic field solutions. The developed theory yields new criteria and conditions that facilitate the design of new layered metamaterials. In Chapter 2, we followed a bottom-up approach starting with Maxwell's equations to derive a new expression of the electromagnetic fields in Fourier domain. The new representation is a compact product of three terms where each term is dependent on a particular physical parameter of the layered system. The Floquet-Bloch modes, which have been used before for modeling infinite lossless systems, surprisingly show up in one of the three terms, without invoking the Floquet-Bloch theorem.

This Fourier domain representation of the fields shows its capability of decomposing the wave function to analyze complex electromagnetic properties. We extracted the corresponding band diagrams of the Fourier domain representation and used them to graphically describe a wide range of refractive properties of layered metamaterials and to validate the conventional homogenization methods. Although the derived Fourier domain electromagnetic field solutions can be only used for planar flat systems, the followed strategy in this electromagnetic study is not limited to layered metamaterials and it is applicable to any metamaterial structure. Using band diagrams, we analyzed and distinguished the abnormal intrinsic electromagnetic behaviours that cause the external convergence of light. Analyzing the external behaviour of light just after exiting the planar media, we have

introduced a quantitative method in Chapter 3 based on the small-angle phase behaviour to predict the image plane location and consequently the imaging capability of single and multiple layer slabs made of homogeneous isotropic media. Using the proposed flat lens criterion, we designed three flat lenses with novel functionalities. Although the proposed flat lens criterion provides new insights into the field of flat lens imaging and enables a new method for flat lens design over large parameter spaces, it cannot supplant the existing flat lens analysis methods due to several limitations.

A recognized limitation in the flat lens criterion derivations is the disregard of the interactions between the object and lens, where the reflected waves from the source or object have been neglected. However, the interaction effect on calculations become more prominent when the object-to-lens separation is small [61]. Accounting for these interactions would probably provide more accurate predictions but it will lead to object-dependent predictions where the flat lens criterion is not general. Since the flat lens criterion is based on the small-angle phase alone, the other limitation that can be noticed is the lack of information provided by the flat lens criterion for describing the resolution, contrast, or fidelity of the image. To study large-angle plane-wave components with NA near unity or evanescent plane-wave components with NA greater than one, alternative criteria can be developed in future studies by calculating and analyzing the phase of large-angle and evanescent plane-wave components. Another noteworthy limitation of flat lens design is its associated restriction on configurations where the thickness of the layered stack should be much smaller than the wavelength of the light source. This limitation is due to the dependence of flat-lens imaging on the interference of multiple reflected waves within the stack, which is best realized using coherent laser light. However, imaging with partially coherent light source from narrow-band light-emitting diodes, which are low-cost and amenable to fluorescence imaging, should be possible using sufficiently thin stacks. To investigate the compatibility of flat lenses with light sources of different level of coherence, the impact of light coherence on imaging quality should be further examined.

In future works, the correlation between the small-angle flat lens criterion (NA near zero) and super-resolution imaging (NA greater than unity), which has been shown to be accurately predicted by the small-angle criterion, has to be fully understood and established by examining more case studies and rigorously investigating the small-angle flat lens criterion limitations in predicting super-resolution imaging. Consequently, a flat lens aberration theory that accommodates both propagating and evanescent components should be developed. Future flat lens engineering will predominantly focus on practi-

cal challenging features such as imaging over the entire visible spectrum or simultaneously imaging with TM and TE polarizations.

Since light transmission through thin films with complex permittivity is challenging due to the associated loss, we have discussed the theory of optical light transmission through a single bi-layer unit cell made of metal and dielectric in Chapter 4. For the first time, we have theoretically and experimentally shown that transmission enhancement phenomenon in metal-dielectric systems is reciprocal. We show that a thin coating layer on top of a thin base layer can make the base layer more transparent when the two layers have opposite sign susceptibilities. The developed theory can predict the possibility of transmission enhancement and it can estimate the optimal coating layer thickness for the most transparent bi-layer system. Although we experimentally demonstrated that a thin silver coating layer can enhance light transmission through a silicon nitride membrane, the achieved optical transparency enhancements were limited to a narrow-band of the visible spectrum with the maximum transmittance enhancement of $6\pm1\%$. Theoretically, enhancement factors greater than 10% is attainable using thinner silver coatings. However, the experimental implementations of silver-coated membranes are restricted by challenges in making perfectly planar and continuous silver films below 10 nm in thickness. In future, the use of seeding layers to improve the smoothness of the silver layers and the consequences of having bi-layers with opposing magnetic susceptibility can be explored.

Exploring the plasmonic properties of single layers of metals, we have proposed an easy nano-film fabrication procedure for making copper nano-films with enhanced surface plasmon coupling in Chapter 5. The deposition method is based on the modification of two deposition parameters: the deposition rates and the slew rates. We have been able to produce copper films that have optical resonances comparable to gold films. Implementing the introduced nano-film fabrication method, copper nano-films can work as a cheaper substitute for gold nano-films in surface plasmon applications. In future work, copper films could be passivated for making more sensitive, robust and chemically stable SPR sensors.

Overall, this thesis provides a fundamental theoretical study of electromagnetic fields in layered metamaterials with a discussion of three common applications. This work introduced a general method for characterizing and communicating the electromagnetic properties of lossy finite layered metamaterials. Moreover, the thesis proposed three engineering methods for three practical implementations of layered metamaterials to achieve designing new systems with new features. This work is a firm step towards a better understating of electromagnetic fields in layered metamaterials.

Bibliography

[1] E. J. Zeman and G. C. Schatz, "An accurate electromagnetic theory study of surface enhancement factors for ag, au, cu, li, na, al, ga, in, zn, and cd," *Journal of Physical Chemistry*, vol. 91, no. 3, pp. 634–643, 1987.

[2] R. Mehfuz, *Improving the excitation efficiency of Surface Plasmon Polaritons near small apertures in metallic films*. PhD thesis, University of British Columbia, 2013.

[3] C. M. Soukoulis and M. Wegener, "Past achievements and future challenges in the development of three-dimensional photonic metamaterials," *Nature Photonics*, vol. 5, no. 9, pp. 523–530, 2011.

[4] P. Ott, M. H. Al Shakhs, H. J. Lezec, and K. J. Chau, "Flat lens criterion by small-angle phase," *Optics express*, vol. 22, no. 24, pp. 29340–29355, 2014.

[5] K. J. Chau, M. H. Al Shakhs, and P. Ott, "Fourier-domain electromagnetic wave theory for layered metamaterials of finite extent," *Progress In Electromagnetics Research M*, vol. 40, pp. 45–56, 2014.

[6] P. A. Belov and Y. Hao, "Subwavelength imaging at optical frequencies using a transmission device formed by a periodic layered metal-dielectric structure operating in the canalization regime," *Physical Review B*, vol. 73, no. 11, p. 113110, 2006.

[7] T. Xu, A. Agrawal, M. Abashin, K. J. Chau, and H. J. Lezec, "All-angle negative refraction and active flat lensing of ultraviolet light," *Nature*, vol. 497, no. 7450, pp. 470–474, 2013.

[8] M. H. Al Shakhs, P. Ott, and K. J. Chau, "Band diagrams of layered plasmonic metamaterials," *Journal of Applied Physics*, vol. 116, no. 17, p. 173101, 2014.

[9] N. Fang and X. Zhang, "Imaging properties of a metamaterial superlens," *Applied Physics Letters*, vol. 82, no. 2, pp. 161–163, 2003.

[10] D. Melville and R. Blaikie, "Super-resolution imaging through a planar silver layer," *Optics express*, vol. 13, no. 6, pp. 2127–2134, 2005.

[11] D. O. Melville, R. J. Blaikie, and C. R. Wolf, "Submicron imaging with a planar silver lens," *Applied Physics Letters*, vol. 84, no. 22, pp. 4403–4405, 2004.

[12] D. O. Melville and R. J. Blaikie, "Near-field optical lithography using a planar silver lens," *Journal of Vacuum Science & Technology B*, vol. 22, no. 6, pp. 3470–3474, 2004.

[13] R. Kotyński, T. Stefaniuk, and A. Pastuszczak, "Sub-wavelength diffraction-free imaging with low-loss metal-dielectric multilayers," *Applied Physics A*, vol. 103, no. 3, pp. 905–909, 2011.

[14] M. Al Shakhs, L. Augusto, L. Markley, and K. J. Chau, "Boosting the transparency of thin layers by coatings of opposing susceptibility: How metals help see through dielectrics," *Scientific reports*, vol. 6, 2016.

[15] P. Drude, "Zur elektronentheorie der metalle," *Annalen der Physik*, vol. 306, no. 3, pp. 566–613, 1900.

[16] P. Drude, "Zur elektronentheorie der metalle; ii. teil. galvanomagnetische und thermomagnetische effecte," *Annalen der Physik*, vol. 308, no. 11, pp. 369–402, 1900.

[17] P. B. Johnson and R.-W. Christy, "Optical constants of the noble metals," *Physical review B*, vol. 6, no. 12, p. 4370, 1972.

[18] R. A. Depine and A. Lakhtakia, "A new condition to identify isotropic dielectric-magnetic materials displaying negative phase velocity," *Microw. Opt. Technol. Lett.*, vol. 41, 2004.

[19] V. G. Veselago, "The Electrodynamics of Substances with Simultanously Negative Values of ϵ and μ," *Soviet Physics*, vol. 10, 1968.

[20] W. Cai and V. M. Shalaev, *Optical metamaterials*, vol. 10. Springer, 2010.

[21] A. De Baas, "Nanostructured metamaterials–exchange between experts in electromagnetics and material science," *Luxembourg: Publication Office of the European Union*, 2010.

[22] V. M. Shalaev, "Optical negative-index metamaterials," *Nature photonics*, vol. 1, no. 1, pp. 41–48, 2007.

[23] D. R. Smith, J. B. Pendry, and M. C. Wiltshire, "Metamaterials and negative refractive index," *Science*, vol. 305, no. 5685, pp. 788–792, 2004.

[24] J. C. Bose, "On the rotation of plane of polarisation of electric waves by a twisted structure," *Proceedings of the Royal Society of London*, vol. 63, no. 389-400, pp. 146–152, 1898.

[25] R. M. Walser, "Metamaterials: What are they? what are they good for?," in *APS March Meeting Abstracts*, vol. 1, p. 5001, 2000.

[26] D. R. Smith, W. J. Padilla, D. Vier, S. C. Nemat-Nasser, and S. Schultz, "Composite medium with simultaneously negative permeability and permittivity," *Physical review letters*, vol. 84, no. 18, p. 4184, 2000.

[27] J. B. Pendry, "Negative refraction makes a perfect lens," *Physical review letters*, vol. 85, no. 18, p. 3966, 2000.

[28] S. A. Ramakrishna, J. Pendry, M. Wiltshire, and W. Stewart, "Imaging the near field," *Journal of Modern Optics*, vol. 50, no. 9, pp. 1419–1430, 2003.

[29] A. Pastuszczak and R. Kotyński, "Optimized low-loss multilayers for imaging with sub-wavelength resolution in the visible wavelength range," *Journal of Applied Physics*, vol. 109, no. 8, p. 084302, 2011.

[30] B. Zeng, X. Yang, C. Wang, Q. Feng, and X. Luo, "Super-resolution imaging at different wavelengths by using a one-dimensional metamaterial structure," *Journal of Optics*, vol. 12, no. 3, p. 035104, 2010.

[31] N. A. Mortensen, M. Yan, O. Sigmund, and O. Breinbjerg, "On the unambiguous determination of effective optical properties of periodic metamaterials: a one-dimensional case study," *Journal of the European Optical Society-Rapid publications*, vol. 5, 2010.

[32] I. Smolyaninov, Y. Hung, and C. Davis, "Two-dimensional metamaterial structure exhibiting reduced visibility at 500 nm," *Optics letters*, vol. 33, no. 12, pp. 1342–1344, 2008.

[33] R. A. Shore and A. D. Yaghjian, "Traveling waves on two-and three-dimensional periodic arrays of lossless scatterers," *Radio Science*, vol. 42, no. 6, 2007.

[34] J. Valentine, S. Zhang, T. Zentgraf, E. Ulin-Avila, D. A. Genov, G. Bartal, and X. Zhang, "Three-dimensional optical metamaterial with a negative refractive index," *nature*, vol. 455, no. 7211, pp. 376–379, 2008.

[35] B. Casse, W. Lu, Y. Huang, E. Gultepe, L. Menon, and S. Sridhar, "Super-resolution imaging using a three-dimensional metamaterials nanolens," *Applied Physics Letters*, vol. 96, no. 2, p. 023114, 2010.

[36] T. Allen and R. DeCorby, "Assessing the maximum transmittance of periodic metal-dielectric multilayers," *JOSA B*, vol. 28, no. 10, pp. 2529–2536, 2011.

[37] P. Yeh, A. Yariv, and C.-S. Hong, "Electromagnetic propagation in periodic stratified media. i. general theory," *JOSA*, vol. 67, no. 4, pp. 423–438, 1977.

[38] A. A. Maradudin, *Structured surfaces as optical metamaterials*. Cambridge University Press, 2011.

[39] P.-H. Tichit, S. Burokur, D. Germain, and A. De Lustrac, "Design and experimental demonstration of a high-directive emission with transformation optics," *Physical Review B*, vol. 83, no. 15, p. 155108, 2011.

[40] P.-H. Tichit, S. N. Burokur, C.-W. Qiu, and A. de Lustrac, "Experimental verification of isotropic radiation from a coherent dipole source via electric-field-driven l c resonator metamaterials," *Physical review letters*, vol. 111, no. 13, p. 133901, 2013.

[41] A. Boltasseva and V. M. Shalaev, "Fabrication of optical negative-index metamaterials: Recent advances and outlook," *Metamaterials*, vol. 2, no. 1, pp. 1–17, 2008.

[42] H. A. Macleod, *Thin-film optical filters*. CRC press, 2001.

[43] J. Mason, S. Smith, and D. Wasserman, "Strong absorption and selective thermal emission from a midinfrared metamaterial," *Applied Physics Letters*, vol. 98, no. 24, p. 241105, 2011.

[44] R. Jorgenson and S. Yee, "A fiber-optic chemical sensor based on surface plasmon resonance," *Sensors and Actuators B: Chemical*, vol. 12, no. 3, pp. 213–220, 1993.

[45] W. Emkey and C. Jack, "Analysis and evaluation of graded-index fiber lenses," *Journal of Lightwave Technology*, vol. 5, no. 9, pp. 1156–1164, 1987.

[46] F. Aieta, P. Genevet, M. A. Kats, N. Yu, R. Blanchard, Z. Gaburro, and F. Capasso, "Aberration-free ultrathin flat lenses and axicons at telecom wavelengths based on plasmonic metasurfaces," *Nano letters*, vol. 12, no. 9, pp. 4932–4936, 2012.

[47] R. Fleury, D. L. Sounas, and A. Alu, "Negative refraction and planar focusing based on parity-time symmetric metasurfaces," *Physical review letters*, vol. 113, no. 2, p. 023903, 2014.

[48] T. Dumelow, J. A. P. da Costa, and V. N. Freire, "Slab lenses from simple anisotropic media," *Physical Review B*, vol. 72, no. 23, p. 235115, 2005.

[49] W. T. Lu and S. Sridhar, "Flat lens without optical axis: Theory of imaging," *Optics express*, vol. 13, no. 26, pp. 10673–10680, 2005.

[50] N. Fang, H. Lee, C. Sun, and X. Zhang, "Sub-diffraction-limited optical imaging with a silver superlens," *Science*, vol. 308, no. 5721, pp. 534–537, 2005.

[51] R. Blaikie and S. McNab, "Simulation study of perfect lenses for near-field optical nanolithography," *Microelectronic engineering*, vol. 61, pp. 97–103, 2002.

[52] J. Shen and P. Platzman, "Near field imaging with negative dielectric constant lenses," *Applied physics letters*, vol. 80, no. 18, pp. 3286–3288, 2002.

[53] S. Durant, N. Fang, and X. Zhang, "Comment on" submicron imaging with a planar silver lens"(appl. phys. lett. 84, 4403 (2004))," *Applied Physics Letters*, vol. 86, no. 12, pp. 126101–126101, 2005.

[54] H. Lee, Y. Xiong, N. Fang, W. Srituravanich, S. Durant, M. Ambati, C. Sun, and X. Zhang, "Realization of optical superlens imaging below the diffraction limit," *New Journal of Physics*, vol. 7, no. 1, p. 255, 2005.

[55] E. Shamonina, V. Kalinin, K. Ringhofer, and L. Solymar, "Imaging, compression and poynting vector streamlines for negative permittivity materials," *Electronics Letters*, vol. 37, no. 20, p. 1, 2001.

[56] K. Webb and M. Yang, "Subwavelength imaging with a multilayer silver film structure," *Optics letters*, vol. 31, no. 14, pp. 2130–2132, 2006.

[57] S. Feng and J. M. Elson, "Diffraction-suppressed high-resolution imaging through metallodielectric nanofilms," *Optics express*, vol. 14, no. 1, pp. 216–221, 2006.

[58] D. O. Melville and R. J. Blaikie, "Analysis and optimization of multilayer silver superlenses for near-field optical lithography," *Physica B: Condensed Matter*, vol. 394, no. 2, pp. 197–202, 2007.

[59] D. de Ceglia, M. A. Vincenti, M. Cappeddu, M. Centini, N. Akozbek, A. DOrazio, J. W. Haus, M. J. Bloemer, and M. Scalora, "Tailoring metallodielectric structures for superresolution and superguiding applications in the visible and near-ir ranges," *Physical Review A*, vol. 77, no. 3, p. 033848, 2008.

[60] C. P. Moore, M. D. Arnold, P. J. Bones, and R. J. Blaikie, "Image fidelity for single-layer and multi-layer silver superlenses," *JOSA A*, vol. 25, no. 4, pp. 911–918, 2008.

[61] C. P. Moore, R. J. Blaikie, and M. D. Arnold, "An improved transfer-matrix model for optical superlenses," *Optics Express*, vol. 17, no. 16, pp. 14260–14269, 2009.

[62] R. Kotyński and T. Stefaniuk, "Comparison of imaging with subwavelength resolution in the canalization and resonant tunnelling regimes," *Journal of Optics A: Pure and Applied Optics*, vol. 11, no. 1, p. 015001, 2008.

[63] J. Bénédicto, E. Centeno, and A. Moreau, "Lens equation for flat lenses made with hyperbolic metamaterials," *Optics letters*, vol. 37, no. 22, pp. 4786–4788, 2012.

[64] P. H. Berning and A. Turner, "Induced transmission in absorbing films applied to band pass filter design," *JOSA*, vol. 47, no. 3, pp. 230–239, 1957.

[65] H. Macleod, "A new approach to the design of metal-dielectric thin-film optical coatings," *Journal of Modern Optics*, vol. 25, no. 2, pp. 93–106, 1978.

[66] P. Lissberger, "Coatings with induced transmission," *Applied Optics*, vol. 20, no. 1, pp. 95–104, 1981.

[67] R. Dragila, B. Luther-Davies, and S. Vukovic, "High transparency of classically opaque metallic films," *Physical review letters*, vol. 55, no. 10, p. 1117, 1985.

[68] I. R. Hooper, T. Preist, and J. R. Sambles, "Making tunnel barriers (including metals) transparent," *Physical review letters*, vol. 97, no. 5, p. 053902, 2006.

[69] L. Holland and G. Siddall, "Heat-reflecting windows using gold and bismuth oxide films," *British Journal of Applied Physics*, vol. 9, no. 9, p. 359, 1958.

[70] J. C. Fan, F. J. Bachner, G. H. Foley, and P. M. Zavracky, "Transparent heat-mirror films of tio2/ag/tio2 for solar energy collection and radiation insulation," *Applied Physics Letters*, vol. 25, no. 12, pp. 693–695, 1974.

[71] C. Granqvist, "Radiative heating and cooling with spectrally selective surfaces," *Applied optics*, vol. 20, no. 15, pp. 2606–2615, 1981.

[72] C. M. Lampert, "Heat mirror coatings for energy conserving windows," *Solar Energy Materials*, vol. 6, no. 1, pp. 1–41, 1981.

[73] B. E. Yoldas and T. OKeefe, "Deposition of optically transparent ir reflective coatings on glass," *Applied optics*, vol. 23, no. 20, pp. 3638–3643, 1984.

[74] C. G. Granqvist, "Transparent conductors as solar energy materials: A panoramic review," *Solar energy materials and solar cells*, vol. 91, no. 17, pp. 1529–1598, 2007.

[75] K. Ellmer, "Past achievements and future challenges in the development of optically transparent electrodes," *Nature Photonics*, vol. 6, no. 12, pp. 809–817, 2012.

[76] J. Ham, S. Kim, G. H. Jung, W. J. Dong, and J.-L. Lee, "Design of broadband transparent electrodes for flexible organic solar cells," *Journal of Materials Chemistry A*, vol. 1, no. 9, pp. 3076–3082, 2013.

[77] P. Lansåker, P. Petersson, G. A. Niklasson, and C.-G. Granqvist, "Thin sputter deposited gold films on in 2 o 3: Sn, sno 2: In, tio

2 and glass: optical, electrical and structural effects," *Solar Energy Materials and Solar Cells*, vol. 117, pp. 462–470, 2013.

[78] M. J. Bloemer and M. Scalora, "Transmissive properties of ag/mgf2 photonic band gaps," *Applied physics letters*, vol. 72, no. 14, pp. 1676–1678, 1998.

[79] K.-T. Lee, S. Seo, J. Y. Lee, and L. J. Guo, "Ultrathin metal-semiconductor-metal resonator for angle invariant visible band transmission filters," *Applied Physics Letters*, vol. 104, no. 23, p. 231112, 2014.

[80] C.-S. Park, V. R. Shrestha, S.-S. Lee, E.-S. Kim, and D.-Y. Choi, "Omnidirectional color filters capitalizing on a nano-resonator of ag-tio2-ag integrated with a phase compensating dielectric overlay," *Scientific reports*, vol. 5, 2015.

[81] B. Wood, J. Pendry, and D. Tsai, "Directed subwavelength imaging using a layered metal-dielectric system," *Physical Review B*, vol. 74, no. 11, p. 115116, 2006.

[82] Z. Jacob, L. V. Alekseyev, and E. Narimanov, "Optical hyperlens: far-field imaging beyond the diffraction limit," *Optics express*, vol. 14, no. 18, pp. 8247–8256, 2006.

[83] A. Fang, T. Koschny, and C. M. Soukoulis, "Optical anisotropic metamaterials: Negative refraction and focusing," *Physical Review B*, vol. 79, no. 24, p. 245127, 2009.

[84] S. Nelson, K. S. Johnston, and S. S. Yee, "High sensitivity surface plasmon resonace sensor based on phase detection," *Sensors and Actuators B: Chemical*, vol. 35, no. 1, pp. 187–191, 1996.

[85] J. Homola, S. S. Yee, and G. Gauglitz, "Surface plasmon resonance sensors: review," *Sensors and Actuators B: Chemical*, vol. 54, no. 1, pp. 3–15, 1999.

[86] A. G. Brolo, R. Gordon, B. Leathem, and K. L. Kavanagh, "Surface plasmon sensor based on the enhanced light transmission through arrays of nanoholes in gold films," *Langmuir*, vol. 20, no. 12, pp. 4813–4815, 2004.

[87] J. Homola, "Surface plasmon resonance sensors for detection of chemical and biological species," *Chemical reviews*, vol. 108, no. 2, pp. 462–493, 2008.

[88] K. M. Mayer and J. H. Hafner, "Localized surface plasmon resonance sensors," *Chemical reviews*, vol. 111, no. 6, pp. 3828–3857, 2011.

[89] L. C. Oliveira, A. M. N. Lima, C. Thirstrup, and H. F. Neff, *Surface Plasmon Resonance Sensors: A Materials Guide to Design and Optimization*. Springer, 2015.

[90] V. J. Sorger, R. F. Oulton, R.-M. Ma, and X. Zhang, "Toward integrated plasmonic circuits," *MRS bulletin*, vol. 37, no. 08, pp. 728–738, 2012.

[91] G. V. Naik, V. M. Shalaev, and A. Boltasseva, "Alternative plasmonic materials: beyond gold and silver," *Advanced Materials*, vol. 25, no. 24, pp. 3264–3294, 2013.

[92] F. Markey, "Principles of surface plasmon resonance," in *Real-Time Analysis of Biomolecular Interactions*, pp. 13–22, Springer, 2000.

[93] M. J. Previte, Y. Zhang, K. Aslan, and C. D. Geddes, "Surface plasmon coupled fluorescence from copper substrates," *Applied Physics Letters*, vol. 91, no. 15, p. 151902, 2007.

[94] S. Wu, H. Ho, W. Law, C. Lin, and S. Kong, "Highly sensitive differential phase-sensitive surface plasmon resonance biosensor based on the mach–zehnder configuration," *Optics Letters*, vol. 29, no. 20, pp. 2378–2380, 2004.

[95] S. Singh, S. K. Mishra, and B. D. Gupta, "Sensitivity enhancement of a surface plasmon resonance based fibre optic refractive index sensor utilizing an additional layer of oxides," *Sensors and Actuators A: Physical*, vol. 193, pp. 136–140, 2013.

[96] K. Aslan, K. McDonald, M. J. Previte, Y. Zhang, and C. D. Geddes, "Silver island nanodeposits to enhance surface plasmon coupled fluorescence from copper thin films," *Chemical Physics Letters*, vol. 464, no. 4, pp. 216–219, 2008.

[97] H. Ditlbacher, J. Krenn, G. Schider, A. Leitner, and F. Aussenegg, "Two-dimensional optics with surface plasmon polaritons," *Applied Physics Letters*, vol. 81, no. 10, pp. 1762–1764, 2002.

[98] C. Ruan, W. Wang, and B. Gu, "Surface-enhanced raman scattering for perchlorate detection using cystamine-modified gold nanoparticles," *Analytica chimica acta*, vol. 567, no. 1, pp. 114–120, 2006.

[99] J.-F. Masson, L. S. Live, and M.-P. Murray-Méthot, "High sensitivity plasmonic structures for use in surface plasmon resonance sensors and method of fabrication thereof," 2014. US Patent 8,860,943.

[100] X. Chen, C. Zhao, L. Rothberg, and M.-K. Ng, "Plasmon enhancement of bulk heterojunction organic photovoltaic devices by electrode modification," *Applied Physics Letters*, vol. 93, no. 12, p. 123302, 2008.

[101] S. Mishra, B. Zou, and K. S. Chiang, "Surface-plasmon-resonance refractive-index sensor with cu-coated polymer waveguide,"

[102] D. Lepage, D. Carrier, A. Jiménez, J. Beauvais, and J. J. Dubowski, "Plasmonic propagations distances for interferometric surface plasmon resonance biosensing," *Nanoscale research letters*, vol. 6, no. 1, pp. 1–7, 2011.

[103] K. M. McPeak, S. V. Jayanti, S. J. Kress, S. Meyer, S. Iotti, A. Rossinelli, and D. J. Norris, "Plasmonic films can easily be better: rules and recipes," *ACS photonics*, vol. 2, no. 3, pp. 326–333, 2015.

[104] C. Menzel, T. Paul, C. Rockstuhl, T. Pertsch, S. Tretyakov, and F. Lederer, "Validity of effective material parameters for optical fishnet metamaterials," *Physical Review B*, vol. 81, no. 3, p. 035320, 2010.

[105] T. Paul, C. Menzel, W. Śmigaj, C. Rockstuhl, P. Lalanne, and F. Lederer, "Reflection and transmission of light at periodic layered metamaterial films," *Physical Review B*, vol. 84, no. 11, p. 115142, 2011.

[106] A. Nicolson and G. Ross, "Measurement of the intrinsic properties of materials by time-domain techniques," *IEEE Transactions on instrumentation and measurement*, vol. 19, no. 4, pp. 377–382, 1970.

[107] W. B. Weir, "Automatic measurement of complex dielectric constant and permeability at microwave frequencies," *Proceedings of the IEEE*, vol. 62, no. 1, pp. 33–36, 1974.

[108] D. Smith, S. Schultz, P. Markoš, and C. Soukoulis, "Determination of effective permittivity and permeability of metamaterials from reflec-

tion and transmission coefficients," *Physical Review B*, vol. 65, no. 19, p. 195104, 2002.

[109] P. Markoš and C. M. Soukoulis, "Transmission properties and effective electromagnetic parameters of double negative metamaterials," *Optics express*, vol. 11, no. 7, pp. 649–661, 2003.

[110] X. Chen, T. M. Grzegorczyk, B.-I. Wu, J. Pacheco Jr, and J. A. Kong, "Robust method to retrieve the constitutive effective parameters of metamaterials," *Physical Review E*, vol. 70, no. 1, p. 016608, 2004.

[111] D. Smith, D. Vier, T. Koschny, and C. Soukoulis, "Electromagnetic parameter retrieval from inhomogeneous metamaterials," *Physical review E*, vol. 71, no. 3, p. 036617, 2005.

[112] S. Arslanagić, T. V. Hansen, N. A. Mortensen, A. H. Gregersen, O. Sigmund, R. W. Ziolkowski, and O. Breinbjerg, "A review of the scattering-parameter extraction method with clarification of ambiguity issues in relation to metamaterial homogenization," *IEEE Antennas and Propagation Magazine*, vol. 55, no. 2, pp. 91–106, 2013.

[113] D. R. Smith, D. Vier, N. Kroll, and S. Schultz, "Direct calculation of permeability and permittivity for a left-handed metamaterial," *Applied Physics Letters*, vol. 77, no. 14, pp. 2246–2248, 2000.

[114] D. R. Smith and J. B. Pendry, "Homogenization of metamaterials by field averaging," *JOSA B*, vol. 23, no. 3, pp. 391–403, 2006.

[115] J.-M. Lerat, N. Malléjac, and O. Acher, "Determination of the effective parameters of a metamaterial by field summation method," *Journal of applied physics*, vol. 100, no. 8, p. 084908, 2006.

[116] A. Andryieuski, S. Ha, A. A. Sukhorukov, Y. S. Kivshar, and A. V. Lavrinenko, "Unified approach for retrieval of effective parameters of metamaterials," in *SPIE Optics+ Optoelectronics*, pp. 807008–807008, International Society for Optics and Photonics, 2011.

[117] A. Pors, I. Tsukerman, and S. I. Bozhevolnyi, "Effective constitutive parameters of plasmonic metamaterials: homogenization by dual field interpolation," *Physical Review E*, vol. 84, no. 1, p. 016609, 2011.

[118] I. Tsukerman, "Nonlocal homogenization of metamaterials by dual interpolation of fields," *JOSA B*, vol. 28, no. 12, pp. 2956–2965, 2011.

[119] S. Rytov, "Electromagnetic properties of a finely stratified medium," *SOVIET PHYSICS JETP-USSR*, vol. 2, no. 3, pp. 466–475, 1956.

[120] A. H. Sihvola, *Electromagnetic mixing formulas and applications*. No. 47, Iet, 1999.

[121] C. R. Simovski and S. He, "Frequency range and explicit expressions for negative permittivity and permeability for an isotropic medium formed by a lattice of perfectly conducting ω particles," *Physics letters A*, vol. 311, no. 2, pp. 254–263, 2003.

[122] K. J. Chau, "Homogenization of waveguide-based metamaterials by energy averaging," *Physical Review B*, vol. 85, no. 12, p. 125101, 2012.

[123] G. Lubkowski, R. Schuhmann, and T. Weiland, "Extraction of effective metamaterial parameters by parameter fitting of dispersive models," *Microwave and Optical Technology Letters*, vol. 49, no. 2, pp. 285–288, 2007.

[124] A. Alù, "First-principles homogenization theory for periodic metamaterials," *Physical Review B*, vol. 84, no. 7, p. 075153, 2011.

[125] D. Sjöberg, C. Engström, G. Kristensson, D. J. Wall, and N. Wellander, "A floquet-bloch decomposition of maxwell's equations applied to homogenization," *Multiscale Modeling & Simulation*, vol. 4, no. 1, pp. 149–171, 2005.

[126] I. Tsukerman, "Negative refraction and the minimum lattice cell size," *JOSA B*, vol. 25, no. 6, pp. 927–936, 2008.

[127] A. Căbuz, D. Felbacq, and D. Cassagne, "Spatial dispersion in negative-index composite metamaterials," *Physical Review A*, vol. 77, no. 1, p. 013807, 2008.

[128] C. Rockstuhl, T. Paul, F. Lederer, T. Pertsch, T. Zentgraf, T. P. Meyrath, and H. Giessen, "Transition from thin-film to bulk properties of metamaterials," *Physical Review B*, vol. 77, no. 3, p. 035126, 2008.

[129] A. Andryieuski, S. Ha, A. A. Sukhorukov, Y. S. Kivshar, and A. V. Lavrinenko, "Bloch-mode analysis for retrieving effective parameters of metamaterials," *Physical Review B*, vol. 86, no. 3, p. 035127, 2012.

[130] F. Bloch, "Quantum mechanics of electrons in crystal lattices," *Z. Phys*, vol. 52, pp. 555–600, 1928.

[131] G. Floquet, "Sur les équations différentielles linéaires à coefficients périodiques," in *Annales scientifiques de l'École normale supérieure*, vol. 12, pp. 47–88, 1883.

[132] L. Rayleigh, "On the maintenance of vibrations by forces of double frequency, and on the propagation of waves through a medium endowed with a periodic structure," *The London, Edinburgh, and Dublin Philosophical Magazine and Journal of Science*, vol. 24, no. 147, pp. 145–159, 1887.

[133] V. Bykov, "Spontaneous emission in a periodic structure," *Soviet Journal of Experimental and Theoretical Physics*, vol. 35, p. 269, 1972.

[134] I. A. Sukhoivanov and I. V. Guryev, *Photonic crystals: physics and practical modeling*, vol. 152. Springer, 2009.

[135] E. Yablonovitch, "Inhibited spontaneous emission in solid-state physics and electronics," *Physical review letters*, vol. 58, no. 20, p. 2059, 1987.

[136] S. John, "Strong localization of photons in certain disordered dielectric superlattices," *Physical review letters*, vol. 58, no. 23, p. 2486, 1987.

[137] S. Fan, P. R. Villeneuve, and J. Joannopoulos, "Large omnidirectional band gaps in metallodielectric photonic crystals," *Physical Review B*, vol. 54, no. 16, p. 11245, 1996.

[138] K. C. Huang, E. Lidorikis, X. Jiang, J. D. Joannopoulos, K. A. Nelson, P. Bienstman, and S. Fan, "Nature of lossy bloch states in polaritonic photonic crystals," *Physical Review B*, vol. 69, no. 19, p. 195111, 2004.

[139] G. Parisi, P. Zilio, and F. Romanato, "Complex bloch-modes calculation of plasmonic crystal slabs by means of finite elements method," *Optics Express*, vol. 20, no. 15, pp. 16690–16703, 2012.

[140] A. Yariv and P. Yeh, *Optical waves in crystals*, vol. 10. Wiley, New York, 1984.

[141] S. G. Johnson and J. D. Joannopoulos, "Introduction to photonic crystals: Blochs theorem, band diagrams, and gaps (but no defects)," *Photonic Crystal Tutorial*, pp. 1–16, 2003.

[142] C. Sibilia, T. M. Benson, M. Marciniak, and T. Szoplik, *Photonic crystals: physics and technology*. Springer, 2008.

[143] K. Sakoda, *Optical properties of photonic crystals*, vol. 80. Springer Science & Business Media, 2004.

[144] F. Abeles, "Investigations on the propagation of sinusoidal electromagnetic waves in stratified media. application to thin films," *Ann. Phys.(Paris)*, vol. 5, pp. 596–640, 1950.

[145] M. Born and E. Wolf, *Principles of optics: electromagnetic theory of propagation, interference and diffraction of light*. CUP Archive, 2000.

[146] D. W. Berreman, "Optics in stratified and anisotropic media: 4× 4-matrix formulation," *Josa*, vol. 62, no. 4, pp. 502–510, 1972.

[147] J. Lekner, "Light in periodically stratified media," *JOSA A*, vol. 11, no. 11, pp. 2892–2899, 1994.

[148] P. Yeh, "Electromagnetic propagation in birefringent layered media," *JOSA*, vol. 69, no. 5, pp. 742–756, 1979.

[149] O. S. Heavens, *Optical properties of thin solid films*. Courier Corporation, 1991.

[150] E. Verhagen, R. de Waele, L. Kuipers, and A. Polman, "Three-dimensional negative index of refraction at optical frequencies by coupling plasmonic waveguides," *Physical review letters*, vol. 105, no. 22, p. 223901, 2010.

[151] I. Aghanejad, K. J. Chau, and L. Markley, "Electromagnetic origins of negative refraction in coupled plasmonic waveguide metamaterials," *Physical Review B*, vol. 94, no. 16, p. 165133, 2016.

[152] M. Davanço, Y. Urzhumov, and G. Shvets, "The complex bloch bands of a 2d plasmonic crystal displaying isotropic negative refraction," *Optics express*, vol. 15, no. 15, pp. 9681–9691, 2007.

[153] C. Fietz, Y. Urzhumov, and G. Shvets, "Complex k band diagrams of 3d metamaterial/photonic crystals.," *Optics express*, vol. 19, no. 20, pp. 19027–19041, 2011.

[154] B. Lombardet, L. A. Dunbar, R. Ferrini, and R. Houdré, "Fourier analysis of bloch wave propagation in photonic crystals," *JOSA B*, vol. 22, no. 6, pp. 1179–1190, 2005.

[155] B. Lombardet, L. Dunbar, R. Ferrini, and R. Houdré, "Bloch wave propagation in two-dimensional photonic crystals: Influence of the polarization," *Optical and quantum electronics*, vol. 37, no. 1-3, pp. 293–307, 2005.

[156] O. Breinbjerg, "Properties of floquet-bloch space harmonics in 1d periodic magneto-dielectric structures," in *2012 International Conference on Electromagnetics in Advanced Applications*, IEEE, 2012.

[157] L. Brillouin, *Wave propagation in periodic structures: electric filters and crystal lattices*. Courier Corporation, 2003.

[158] A. Yariv and P. Yeh, "Electromagnetic propagation in periodic stratified media. ii. birefringence, phase matching, and x-ray lasers," *JOSA*, vol. 67, no. 4, pp. 438–447, 1977.

[159] W.-C. Liu and M. W. Kowarz, "Vector diffraction from subwavelength optical disk structures: two-dimensional modeling of near-field profiles, far-field intensities, and detector signals from a dvd," *Applied optics*, vol. 38, no. 17, pp. 3787–3797, 1999.

[160] G. Veronis and S. Fan, "Overview of simulation techniques for plasmonic devices," in *Surface plasmon nanophotonics*, pp. 169–182, Springer, 2007.

[161] W. M. Haynes, *CRC handbook of chemistry and physics*. CRC press, 2014.

[162] R. Rumpf, "Design and optimization of nano-optical elements by coupling fabrication to optical behavior," *Ph.D. Dissertation*, pp. 60–81, 2006.

[163] C. M. Rappaport and B. J. McCartin, "Fdfd analysis of electromagnetic scattering in anisotropic media using unconstrained triangular meshes," *IEEE Transactions on Antennas and Propagation*, vol. 39, no. 3, pp. 345–349, 1991.

[164] G. Shvets, "Photonic approach to making a material with a negative index of refraction," *Physical Review B*, vol. 67, no. 3, p. 035109, 2003.

[165] H. J. Lezec, J. A. Dionne, and H. A. Atwater, "Negative refraction at visible frequencies," *Science*, vol. 316, no. 5823, pp. 430–432, 2007.

[166] R. Kotyński and T. Stefaniuk, "Comparison of imaging with subwavelength resolution in the canalization and resonant tunnelling regimes," *Journal of Optics A: Pure and Applied Optics*, vol. 11, no. 1, p. 015001, 2008.

[167] C. R. Simovski, "Bloch material parameters of magneto-dielectric metamaterials and the concept of bloch lattices," *Metamaterials*, vol. 1, no. 2, pp. 62–80, 2007.

[168] R. F. Oulton and J. B. Pendry, "Negative refraction: Imaging through the looking-glass," *Nature Physics*, vol. 9, no. 6, pp. 323–324, 2013.

[169] J. W. Goodman, *Introduction to Fourier optics*. Roberts and Company Publishers, 2005.

[170] P. Yeh, *Optical waves in layered media*, vol. 61. Wiley-Interscience, 2005.

[171] J. A. Kong, *Electromagnetic Wave Theory*. EMW Publishing, 2005.

[172] H. R. Philipp, "Optical properties of silicon nitride," *Journal of the Electrochemical Society*, vol. 120, no. 2, pp. 295–300, 1973.

[173] M. A. Kats, R. Blanchard, P. Genevet, and F. Capasso, "Nanometre optical coatings based on strong interference effects in highly absorbing media," *Nature materials*, vol. 12, no. 1, pp. 20–24, 2013.

[174] F. F. Schlich and R. Spolenak, "Strong interference in ultrathin semiconducting layers on a wide variety of substrate materials," *Applied Physics Letters*, vol. 103, no. 21, p. 213112, 2013.

[175] W. Streyer, S. Law, G. Rooney, T. Jacobs, and D. Wasserman, "Strong absorption and selective emission from engineered metals with dielectric coatings," *Optics express*, vol. 21, no. 7, pp. 9113–9122, 2013.

[176] S. S. Mirshafieyan and J. Guo, "Silicon colors: spectral selective perfect light absorption in single layer silicon films on aluminum surface and its thermal tunability," *Optics express*, vol. 22, no. 25, pp. 31545–31554, 2014.

[177] J. R. DeVore, "Refractive indices of rutile and sphalerite," *JOSA*, vol. 41, no. 6, pp. 416–419, 1951.

[178] W. Pawlewicz, "Influence of deposition conditions on sputter-deposited amorphous silicon," *Journal of Applied Physics*, vol. 49, no. 11, pp. 5595–5601, 1978.

[179] J. A. Thornton, "The microstructure of sputter-deposited coatings," *Journal of Vacuum Science & Technology A*, vol. 4, no. 6, pp. 3059–3065, 1986.

[180] V. Logeeswaran, N. P. Kobayashi, M. S. Islam, W. Wu, P. Chaturvedi, N. X. Fang, S. Y. Wang, and R. S. Williams, "Ultrasmooth silver thin films deposited with a germanium nucleation layer," *Nano letters*, vol. 9, no. 1, pp. 178–182, 2008.

[181] H. Liu, B. Wang, E. S. Leong, P. Yang, Y. Zong, G. Si, J. Teng, and S. A. Maier, "Enhanced surface plasmon resonance on a smooth silver film with a seed growth layer," *ACS nano*, vol. 4, no. 6, pp. 3139–3146, 2010.

[182] S. Roh, T. Chung, and B. Lee, "Overview of the characteristics of micro-and nano-structured surface plasmon resonance sensors," *Sensors*, vol. 11, no. 2, pp. 1565–1588, 2011.

[183] E. Kretschmann, "Die bestimmung optischer konstanten von metallen durch anregung von oberflächenplasmaschwingungen," *Zeitschrift für Physik*, vol. 241, no. 4, pp. 313–324, 1971.

[184] P. Kelly, Y. Zhou, and A. Postill, "A novel technique for the deposition of aluminium-doped zinc oxide films," *Thin Solid Films*, vol. 426, no. 1, pp. 111–116, 2003.

[185] J. M. Luther, P. K. Jain, T. Ewers, and A. P. Alivisatos, "Localized surface plasmon resonances arising from free carriers in doped quantum dots," *Nature materials*, vol. 10, no. 5, pp. 361–366, 2011.

[186] X. Yang, J. Yao, J. Rho, X. Yin, and X. Zhang, "Experimental realization of three-dimensional indefinite cavities at the nanoscale with anomalous scaling laws," *Nature Photonics*, vol. 6, no. 7, pp. 450–454, 2012.

Appendices

Appendices A

Surface Plasmon Polaritons

Surface plasmon polariton waves are a valid solution of Maxwell's equations under certain conditions. Having two semi-infinite non-magnetic media where the interface is at $z = 0$, the first and the second media are characterized by the local complex relative permittivities $\underline{\epsilon}_1$ and $\underline{\epsilon}_2$, respectively. Starting with a TM polarized wave, the electromagnetic fields propagating about the interface along the $+x$-direction and decaying along the z directions are given by

$$\underline{H}_y(z) = \begin{cases} \underline{H}_1 e^{i\underline{k}_x x} e^{\underline{k}_{z1} z} & z < 0 \\ \underline{H}_2 e^{i\underline{k}_x x} e^{-\underline{k}_{z2} z} & z > 0, \end{cases} \tag{A.1}$$

$$\underline{E}_x(z) = \begin{cases} -i\underline{k}_{z1}\underline{H}_1 e^{i\underline{k}_x x} e^{\underline{k}_{z1} z}/\omega\epsilon_0\underline{\epsilon}_1 & z < 0 \\ i\underline{k}_{z2}\underline{H}_2 e^{i\underline{k}_x x} e^{-\underline{k}_{z2} z}/\omega\epsilon_0\underline{\epsilon}_2 & z > 0, \end{cases} \tag{A.2}$$

and

$$\underline{E}_z(z) = \begin{cases} -\underline{k}_x\underline{H}_1 e^{i\underline{k}_x x} e^{\underline{k}_{z1} z}/\omega\epsilon_0\underline{\epsilon}_1 & z < 0 \\ -\underline{k}_x\underline{H}_2 e^{i\underline{k}_x x} e^{-\underline{k}_{z2} z}/\omega\epsilon_0\underline{\epsilon}_2 & z > 0. \end{cases} \tag{A.3}$$

where $\underline{H}_1$ and $\underline{H}_2$ are the complex amplitudes of the magnetic field in media 1 and 2, respectively, $\underline{k}_x$ is the complex wave vector component along the x axis, and $\underline{k}_{z1}$ and $\underline{k}_{z2}$ are the complex wave vector components along the z axis in media 1 and 2, respectively. Due to continuity of the fields across the interface, $\underline{k}_x$ is the uniquely defined mode in both media.

Imposing the continuity of the tangential components of the electric fields at $z = 0$, we get

$$\frac{\underline{k}_{z1}\underline{H}_1}{\underline{\epsilon}_1} + \frac{\underline{k}_{z2}\underline{H}_2}{\underline{\epsilon}_2} = 0, \tag{A.4}$$

and

$$\underline{H}_1 - \underline{H}_2 = 0, \tag{A.5}$$

which has a solution only if

$$\frac{\underline{k}_{z1}}{\underline{k}_{z2}} = -\frac{\underline{\epsilon}_1}{\underline{\epsilon}_2}. \tag{A.6}$$

For positive real $\underline{k}_{z1}$ and $\underline{k}_{z2}$, surface waves can exist if the real parts of the permittivities of the two media have opposite signs. Such condition can be satisfied at the interface between a metal and a dielectric media.

Conducting the same exercise for TE polarization, the complex amplitudes of the electric fields across the interface should satisfy

$$\underline{E}_1 = \underline{E}_2, \tag{A.7}$$

and

$$\underline{E}_1(\underline{k}_{z1} + \underline{k}_{z2}) = 0. \tag{A.8}$$

As in the TM polarization case, $\underline{k}_{z1}$ and $\underline{k}_{z2}$ are positive and real. Therefore, the only possible solution will be $\underline{E}_1 = \underline{E}_2 = 0$, which indicates that surface electromagnetic waves cannot exist at the interface of non-magnetic media for TE-polarization.

Appendices B

Evanescent Wave Amplification with a Thin Silver Layer

From Maxwell's equations, the general form of the wavevector k_z for propagating waves in free-space [27] is given by

$$k_z = +\sqrt{\omega^2 c^{-2} - k_x^2 - k_y^2}, \tag{B.1}$$

where $\omega^2 c^{-2} > k_x^2 + k_y^2$. For larger values of the transverse wavevector, k_z will be given by

$$k_z = +i\sqrt{k_x^2 + k_y^2 - \omega^2 c^{-2}}, \tag{B.2}$$

where $\omega^2 c^{-2} < k_x^2 + k_y^2$. Electromagnetic waves defined by the latter wavevector are known as evanescent waves where they decay exponentially with z. In a medium defined by the electromagnetic properties ϵ and μ, the wavevector of the evanescent waves is given by

$$k_z = +i\sqrt{k_x^2 + k_y^2 - \epsilon\,\mu\,\omega^2 c^{-2}}, \tag{B.3}$$

where $\epsilon\,\mu\,\omega^2 c^{-2} < k_x^2 + k_y^2$.

Working with a sub-wavelength thin layer of silver, the electrostatic limit can be applied to decouple electrostatic and magnetostatic fields. For TM-polarized fields, the transmission coefficient becomes independence of μ and a function of ϵ, which is negative at optical frequencies. Based on the electrostatic limit

$$\omega \ll c\sqrt{k_x^2 + k_y^2}. \tag{B.4}$$

The transmission coefficient T of the thin layer assuming the electrostatic limit becomes

$$\begin{aligned}\lim_{k_x^2+k_y^2\to\infty} T &= \lim_{k_x^2+k_y^2\to\infty} \frac{2\epsilon\, k_z}{\epsilon\, k_z + k_z^{'}}\ \frac{2k_z^{'}}{k_z^{'} + \epsilon\, k_z} \\ &\quad \times \frac{exp(ik_z^{'}d)}{1-(\frac{k_z^{'}-\epsilon k_z}{k_z^{'}+\epsilon k_z})^2\ exp(2ik_z^{'}d)} \\ &= \frac{4\epsilon\ exp(ik_z d)}{(\epsilon+1)^2-(\epsilon-1)^2\ exp(2ik_z d)}.\end{aligned} \tag{B.5}$$

Assuming that ϵ is becoming negative, the transmission coefficient becomes

$$\begin{aligned}\lim_{\epsilon\to-1}\ \lim_{k_x^2+k_y^2\to\infty} T &= \lim_{\epsilon\to-1} \frac{4\epsilon\ exp(ik_z d)}{(\epsilon+1)^2-(\epsilon-1)^2\ exp(2ik_z d)} \\ &= exp(-ik_z d) \\ &= exp(+d\sqrt{k_x^2+k_y^2}),\end{aligned} \tag{B.6}$$

which means the thin silver layer does amplify evanescent waves.

Appendices C

S-parameter Method

For a normally incident planewave, the effective wavevector $k_{z(eff)}$ within the layered system along the z direction based on the S-parameter method [167], is given by

$$k_{z(eff)}d = \pm \arccos(\frac{1 - S_{11}^2 + S_{21}^2}{2S_{21}}) + 2m\pi, \tag{C.1}$$

where S_{11} is the reflection coefficient, S_{21} is the transmission coefficient, d is the total thickness of the layered system, and m is an integer.
To derive the above expression, we first substitute the layered system with a homogeneous medium that has identical scattering parameters. Applying the boundary conditions at the front ($z_1 = 0$) and back ($z_2 = d$) interfaces, we get

$$E_l^+ e^{ik_{lz}z_{l+1}} + E_l^- e^{-ik_{lz}z_{l+1}} = E_{l+1}^+ e^{ik_{(l+1)z}z_{l+1}} + E_{l+1}^- e^{-ik_{(l+1)z}z_{l+1}}, \tag{C.2}$$

$$H_l^+ e^{ik_{lz}z_{l+1}} + H_l^- e^{-ik_{lz}z_{l+1}} = H_{l+1}^+ e^{ik_{(l+1)z}z_{l+1}} + H_{l+1}^- e^{-ik_{(l+1)z}z_{l+1}}, \tag{C.3}$$

where E^+ and H^+ represents all wave components propagating towards positive $\hat{z}$ direction, and E^- and H^- represents those propagating towards negative $\hat{z}$ direction. The subscripts l and $l+1$ are used to denote the regions on the left and right side of the interfaces, respectively.
Knowing that $H = \frac{\pm k}{\mu\omega}E$, Eq. (C.3) can be rewritten in terms of electric field

$$\begin{aligned} E_l^+ e^{ik_{lz}z_{l+1}} &- E_l^- e^{-ik_{lz}z_{l+1}} \\ &= p_{l(l+1)}[E_{l+1}^+ e^{ik_{(l+1)z}z_{l+1}} - E_{l+1}^- e^{-ik_{(l+1)z}z_{l+1}}], \end{aligned} \tag{C.4}$$

where

$$p_{l(l+1)} = \frac{\mu_l k_{(l+1)z}}{\mu_{l+1} k_{lz}}. \tag{C.5}$$

The semi-infinite half spaces on both sides of the layered system are assumed to be free-space and denoted by the subscript 0 from the front side and t from the back side. Knowing the electric wave components, the

reflection coefficient R and the transmission coefficient T are defined as

$$R = \frac{E_0^-}{E_0^+}, \tag{C.6}$$

$$T = \frac{E_t^+}{E_0^+}. \tag{C.7}$$

After few lines of manipulations, we can re-write Eq. (C.2) and Eq. (C.4) as

$$\begin{aligned} E_l^+ e^{ik_{lz}z_{l+1}} = \frac{1}{2}(1 + p_{l(l+1)}) \\ [E_{l+1}^+ e^{ik_{(l+1)z}z_{l+1}} + Q_{l(l+1)} E_{l+1}^- e^{-ik_{(l+1)z}z_{l+1}}], \end{aligned} \tag{C.8}$$

$$\begin{aligned} E_l^- e^{-ik_{lz}z_{l+1}} = \frac{1}{2}(1 + p_{l(l+1)}) \\ [Q_{l(l+1)} E_{l+1}^+ e^{ik_{(l+1)z}z_{l+1}} + E_{l+1}^- e^{-ik_{(l+1)z}z_{l+1}}], \end{aligned} \tag{C.9}$$

where

$$Q_{(l+1)l} = \frac{1 - p_{(l+1)l}}{1 + p_{(l+1)l}} = -Q_{l(l+1)}. \tag{C.10}$$

Taking the ratio of Eq. (C.8) and Eq. (C.9), after few manupulations we obtaine

$$\begin{aligned} R = \frac{E_0^-}{E_0^+} &= \frac{e^{i2k_{0z}z_1}}{Q_{01}} + \frac{[1 - (1/Q_{01}^2)]e^{i2(k_{1z}+k_{0z})z_1}}{(1/Q_{01})e^{i2k_{1z}z_1} + Q_{12}e^{i2k_{1z}z_2}} \\ &= \frac{Q_{01} + Q_{12}e^{i2k_{1z}(z_2-z_1)}}{1 + Q_{01}Q_{12}e^{i2k_{1z}(z_2-z_1)}} e^{i2k_{0z}z_1}. \end{aligned} \tag{C.11}$$

Knowing that $Q_{12} = Q_{10} = -Q_{01}$, $k_{1z} = nk_0$, $z_1 = 0$ and $z_2 - z_1 = d$, we get

$$R = \frac{Q_{01}(1 - e^{i2nk_0d})}{1 - Q_{01}^2 e^{i2nk_0d}} = S_{11}. \tag{C.12}$$

Recalling that,

$$E_0^+ e^{ik_{0z}d_t} = \frac{1}{2}(1+p_{01}) \\ [E_t^+ e^{ik_{1z}z_0} + Q_{01}E_t^- e^{-ik_{1z}z_0}], \tag{C.13}$$

and

$$E_1^+ e^{ik_{1z}d_t} = \frac{1}{2}(1+p_{1t}) \\ [E_t^+ e^{ik_{tz}d} + Q_{1t}E_t^- e^{-ik_{tz}d}], \tag{C.14}$$

we can solve for E_t^+

$$E_t^+ = \frac{2}{(1+p_{1t})}[E_1^+ e^{i(k_{1z}-k_{tz})d}], \tag{C.15}$$

and the transmission coefficient will be

$$T = \frac{(1-Q_{01}^2)e^{ink_0d}}{1-Q_{01}^2 e^{i2nk_0d}} = S_{21}. \tag{C.16}$$

Using Eq. C.12 and Eq. C.16, we solve for Q_{01}^2

$$Q_{01}^2 = \frac{e^{ink_0d} - S_{21}}{e^{ink_0d} - S_{21}e^{i2nk_0d}}, \tag{C.17}$$

and

$$Q_{01}^2 = \frac{S_{11}^2}{1 - 2S_{21}e^{ink_0d} + S_{21}^2 e^{i2nk_0d}}. \tag{C.18}$$

Equating Eq. (C.18) and Eq. (C.17), we get

$$\frac{e^{ink_0d} - S_{21}}{e^{ink_0d} - S_{21}e^{i2nk_0d}} = \frac{S_{11}^2}{1 - 2S_{21}e^{ink_0d} + S_{21}^2 e^{i2nk_0d}}. \tag{C.19}$$

After few lines of simplification, we obtain this expression

$$\frac{e^{ink_0d} + e^{-ink_0d}}{2} = \frac{1 - S_{11}^2 + S_{21}^2}{2S_{21}}. \tag{C.20}$$

Since $\frac{e^{ink_0d}+e^{-ink_0d}}{2} = \cos(nk_0d)$, we get the final expression for effective wave vector as Eq. C.1.

Appendices D

Maxwell-Garnett Method

Assume that a plane wave is incident on a metal-dielectric layered structure where the thicknesses t_m and t_d are fairly small compared to the wavelength and ϵ_m and ϵ_d are the dielectric constants of the metal and the dielectric layers, respectively. For TE polarization where electric field is perpindicular to the plane of incidence, the electric displacement D in the layered medium can be considered to be uniform. The corresponding metal and dielectric electric fields are E_m and E_d, and related to the uniform electric displacement by

$$E_m = \frac{D}{\epsilon_m}, \tag{D.1}$$

$$E_d = \frac{D}{\epsilon_d}, \tag{D.2}$$

The averaged mean field over the total volume is

$$E = \frac{t_m \frac{D}{\epsilon_m} + t_d \frac{D}{\epsilon_d}}{t_m + t_d}, \tag{D.3}$$

The effective dielectric constant $\epsilon_\perp$ is:

$$\epsilon_\perp = \frac{D}{E} = \frac{(t_m + t_d)\epsilon_m \epsilon_d}{t_m \epsilon_d + t_d \epsilon_m} = \frac{\epsilon_m \epsilon_d}{f_m \epsilon_d + f_d \epsilon_m}, \tag{D.4}$$

where $f_m = t_m/(t_m + t_d)$ and $f_d = t_d/(t_m + t_d) = 1 - f_m$ are the metal and dielectric filling factors, respectively.
For TM polarization where electric field is parallel to the plane of incidence, the electric field E now is uniform. The corresponding metal and dielectric electric displacements are

$$D_m = \epsilon_m E, \tag{D.5}$$

and

$$D_d = \epsilon_d E. \tag{D.6}$$

The averaged mean field over the total volume is

$$D = \frac{t_m \epsilon_m E + t_d \epsilon_d E}{t_m + t_d}, \tag{D.7}$$

Therefore, the effective dielectric constant $\epsilon_{\|}$ will be:

$$\epsilon_{\|} = \frac{D}{E} = \frac{t_m \epsilon_m + t_d \epsilon_d}{t_m + t_d} = f_m \epsilon_m + f_d \epsilon_d, \tag{D.8}$$

The expressions of introduced $\epsilon_{\|}$ and $\epsilon_{\perp}$ can be re-written as [186]

$$\epsilon_{\perp} = \frac{\epsilon_d \epsilon_m}{(1-p)\epsilon_m + p\epsilon_d}, \tag{D.9}$$

$$\epsilon_{\|} = (1-p)\epsilon_d + p\epsilon_m, \tag{D.10}$$

where $f_1 = p$ and $f_2 = (1-p)$, or as [81]

$$\epsilon_{\|} = \frac{\epsilon_d + \eta \epsilon_m}{1+\eta}, \tag{D.11}$$

$$\epsilon_{\perp} = \frac{\epsilon_d \epsilon_m (\eta + 1)}{\epsilon_m + \eta \epsilon_d}, \tag{D.12}$$

where $\eta = t_d/t_m = p/(1-p)$.

Appendices E

Finite Difference Frequency Domain MATLAB Code

```
% This MATLAB code simulates two-dimensional optical structures using the
% finite-difference frequency-domain method.

function [R,T,m,F,Dr1,Dr2,Dspp] = fdfd2d(lam0,UR2,ER2,RES2,NPML,kinc,pol,nx1,nx2,ny4,ny5)

% INPUT ARGUMENTS
% lam0 is the free space wavelength
% UR2 contains the relative permeability on a 2X grid
% ER2 contains the relative permittivity on a 2X grid
% NPML is the size of the PML on the 1X grid
% RES2 = [dx2 dy2]
% kinc is the indicent wave vector
% pol is the polarization ('E' or 'H')

% OUTPUT ARGUMENTS
% R contains diffraction efficiencies of reflected waves
% T contains diffraction efficiencies of transmitted waves
% m contains the indices of the harmonics in R and T
% F is the computed field

%% HANDLE INPUT AND OUTPUT ARGUMENTS
c = 3e8;
% DETERMINE SIZE OF GRID
[Nx2,Ny2] = size(ER2);
dx2 = RES2(1);
```

```
dy2 = RES2(2);
% 1X GRID PARAMETERS
Nx = Nx2/2;        dx = 2*dx2;
Ny = Ny2/2;        dy = 2*dy2;
% COMPUTE MATRIX SIZE
M = Nx*Ny;
% COMPUTE REFRACTIVE INDEX IN REFLECTION REGION
erref = ER2(:,1);              erref = mean(erref(:));
urref = UR2(:,1);              urref = mean(urref(:));
nref = sqrt(erref*urref);
if erref<0 && urref<0
    nref = -nref;
end
% COMPUTE REFRACTIVE INDEX IN TRANSMISSION REGION
ertrn = ER2(:,Ny2);            ertrn = mean(ertrn(:));
urtrn = UR2(:,Ny2);            urtrn = mean(urtrn(:));
ntrn = sqrt(ertrn*urtrn);
if ertrn<0 && urtrn<0
    ntrn = -ntrn;
end

%% INCORPORATE PERFECTLY MATCHED LAYER BOUNDARY
   CONDITION
% PML PARAMETERS
N0    = 376.73032165;                    %free space
   impedance
amax = 3;
cmax = 1;
p     = 3;
% INITIALIZE PML TO PROBLEM SPACE
sx = ones(Nx2,Ny2);
sy = ones(Nx2,Ny2);
% COMPUTE FREE SPACE WAVE NUMBERS
k0 = 2*pi/lam0;
% Y PML
N = 2*NPML;
for n = 1 : N
    % compute Y-PML value
    ay = 1 + amax*(n/N)^p;
    cy = cmax*sin(0.5*pi*n/N)^2;
```

```
64      s   = ay*(1-i*cy*N0/k0);
65      % incorporate value into PML
66      sy(:,N-n+1)    = s;
67      sy(:,Ny2-N+n) = s;
68  end
69  % X PML
70  for n = 1 : N
71      % compute X-PML value
72      ax = 1 + amax*(n/N)^p;
73      cx = cmax*sin(0.5*pi*n/N)^2;
74      s   = ax*(1-i*cx*N0/k0);
75      % incorporate value into PML
76      sx(N-n+1,:)    = s;
77      sx(Nx2-N+n,:) = s;
78  end
79  % COMPUTE TENSOR COMPONENTS WITH PML
80  ER2xx = ER2 ./ sx .* sy;
81  ER2yy = ER2 .* sx ./ sy;
82  ER2zz = ER2 .* sx .* sy;
83  UR2xx = UR2 ./ sx .* sy;
84  UR2yy = UR2 .* sx ./ sy;
85  UR2zz = UR2 .* sx .* sy;
86  % OVERLAY MATERIALS ONTO 1X GRID
87  ERxx = ER2xx(2:2:Nx2,1:2:Ny2);
88  ERyy = ER2yy(1:2:Nx2,2:2:Ny2);
89  ERzz = ER2zz(1:2:Nx2,1:2:Ny2);
90  URxx = UR2xx(1:2:Nx2,2:2:Ny2);
91  URyy = UR2yy(2:2:Nx2,1:2:Ny2);
92  URzz = UR2zz(2:2:Nx2,2:2:Ny2);
93  % CLEAR TEMPORARY VARIABLES
94  clear N0 amax cmax p sx sy n N ay cy s;
95  clear UR2 ER2 ER2xx ER2yy ER2zz UR2xx UR2yy UR2zz;
96
97  %% PERFORM FINITE-DIFFERENCE FREQUENCY-DOMAIN ANALYSIS
98  % FORM DIAGONAL MATERIAL MATRICES
99  ERxx = diag(sparse(ERxx(:)));
100 ERyy = diag(sparse(ERyy(:)));
101 ERzz = diag(sparse(ERzz(:)));
102 URxx = diag(sparse(URxx(:)));
103 URyy = diag(sparse(URyy(:)));
```

```
104 URzz = diag(sparse(URzz(:)));
105 % COMPUTE DERIVATIVE OPERATORS
106 NS   = [Nx Ny];
107 RES  = [dx dy];
108 BC   = [-2 -2 0 0];
109 [DEX,DEY,DHX,DHY] = yeeder2d(NS,k0*RES,BC,kinc/k0);
110 % At the end of this code, the function code of the
    Yee grid derivatove
111 % operators on a 2D grid is included
112
113 % COMPUTE FIELD MATRIX
114 switch pol
115     case 'E',
116         A = DHX/URyy*DEX + DHY/URxx*DEY + ERzz;
117     case 'H',
118         A = DEX/ERyy*DHX + DEY/ERxx*DHY + URzz;
119     otherwise,
120         error('Unrecognized polarization.');
121 end
122 % COMPUTE SOURCE FIELD
123 micrometers=1;
124 nanometers = micrometers/1000;
125 w0=1200 * nanometers;
126 xa    = [0:Nx-1]*dx;
127 ya    = [0:Ny-1]*dy;
128 [Y,X] = meshgrid(ya,xa);
129 fsrc  = exp(-i*(kinc(1)*X+kinc(2)*Y)); % plane wave
    source
130 fsrc  = fsrc(:);
131 % COMPUTE SCATTERED-FIELD MASKING MATRIX
132 Q = zeros(Nx,Ny);
133 Q(:,1:NPML+2) = 1;
134 Q = diag(sparse(Q(:)));
135 % COMPUTE SOURCE VECTOR
136 f = (Q*A-A*Q)*fsrc;
137 % PREPARE MEMORY
138 clear NS RES BC DEX DEZ DHX DHZ;
139 clear ya X Y fsrc;
140 clear ERxx ERyy ERzz URxx URyy URzz;
141 % COMPUTE FIELD
```

```
142 F = A\f;                    %backward division is used
    here!!
143 F = full(F);
144 F = reshape(F,Nx,Ny);
145
146 %% COMPUTE DIFFRACTION EFFICIENCIES
147 % EXTRACT REFLECTED AND TRANSMITTED WAVES
148 Fref = F(:,NPML+1);
149 Ftrn = F(:,Ny-NPML);
150 % REMOVE PHASE TILT
151 p    = exp(+i*kinc(1)*xa');
152 Fref = Fref .* p;
153 Ftrn = Ftrn .* p;
154 % COMPUTE SPATIAL HARMONICS
155 Fref = fftshift(fft(Fref))/Nx;
156 Ftrn = fftshift(fft(Ftrn))/Nx;
157 % COMPUTE WAVE VECTOR COMPONENTS OF THE SPATIAL
    HARMONICS
158 m   = [-floor(Nx/2):floor(Nx/2)]';
159 kx  = kinc(1) - 2*pi*m/(Nx*dx);
160 kzR = conj( sqrt((k0*nref)^2 - kx.^2) );
161 kzT = conj( sqrt((k0*ntrn)^2 - kx.^2) );
162 x_left = round(nx1/2) -round((1000*nanometers)/dx);
163 x_right = round(nx2/2) + round((1000*nanometers)/dx);
164 Dr1_yb = round(ny5/2);
165 Dr1_ya = round(ny5/2) + round(300*nanometers)/dy;
166 Dr1_y=Dr1_yb:Dr1_ya;
167 Dr2_y=Dr1_ya;
168 Dspp_yb=round(ny4/2) - round((50*nanometers)/dy);
169 Dspp_ya= round(ny5/2);
170 Dspp_y=Dspp_yb:Dspp_ya;
171 F_rad1 = F(x_left,Dr1_y).*conj( F(x_left,Dr1_y) ); %
    field source
172 Dr1 = sum( F_rad1 );% free space detector left
    vertical |
173 F_rad2 = F(x_left:x_right,Dr2_y).*conj(F(x_left:
    x_right,Dr2_y) ); % field source H*conj(H)
174 Dr2 = sum (F_rad2 );% free space detector top
    horizontal
175 F_spp = F(x_left, Dspp_y).*conj( F(x_left, Dspp_y) );
```

```
176 Dspp = sum(F_spp ); % SPP
177 % COMPUTE DIFFRACTION EFFICIENCY
178 switch pol
179     case 'E',
180         R =  abs(Fref).^2 .* real(kzR/kinc(2));
181         T =  abs(Ftrn).^2 .* real(kzT*urref/kinc(2)/
                urtrn);
182     case 'H',
183         R =  abs(Fref).^2 .* real(kzR/kinc(2));
184         T =  abs(Ftrn).^2 .* real(kzT*erref/kinc(2)/
                ertrn);
185 end
```

```
1  function [DEX,DEY,DHX,DHY] = yeeder2d(NS,RES,BC,kinc)
2  % YEEDER2D      Yee Grid Derivatove Operators on a 2D
       Grid
3  %
4  % [DEX,DEY,DHX,DHY] = yeeder2d(NS,RES,BC,kinc);
5  %
6  % Input Arguments
7  % ===============
8  % NS     [Nx Ny] 1X grid size
9  % RES    [dx dy] 1X grid resolution
10 % BC     [xlo xhi ylo yhi] boundary conditions
11 %        -2: pseudo-periodic (requires kinc)
12 %        -1: periodic
13 %         0: Dirichlet
14 % kinc   [kx ky] incident wave vector
15 %        This argument is only needed for pseudo-
       periodic boundaries.
16 %
17 % Note: For normalized grids, use dx=k0*dx and kinc=
       kinc/k0
18 %%%%%%%%%%%%%%%%%%%%%%%%%%%%%%%%%%%%%%%%%%%%%%%%%%%%
19 % VERIFY INPUT/OUTPUT ARGUMENTS
20 %%%%%%%%%%%%%%%%%%%%%%%%%%%%%%%%%%%%%%%%%%%%%%%%%%%%
21 % VERIFY NUMBER OF INPUT ARGUMENTS
22 error(nargchk(3,4,nargin));
23 % VERIFY NUMBER OF OUTPUT ARGUMENTS
24 error(nargchk(1,4,nargout));
```

```
% EXTRACT GRID PARAMETERS
Nx = NS(1);       dx = RES(1);
Ny = NS(2);       dy = RES(2);
% DETERMINE MATRIX SIZE
M = Nx*Ny;
%%%%%%%%%%%%%%%%%%%%%%%%%%%%%%%%%%%%%%%%%%%%%%%%%%%%%%%%%%%%%%%%%%%%%%%%%%%%%%%%
% DEX
%%%%%%%%%%%%%%%%%%%%%%%%%%%%%%%%%%%%%%%%%%%%%%%%%%%%%%%%%%%%%%%%%%%%%%%%%%%%%%%%
% INITIALIZE MATRIX
DEX = sparse(M,M);
% PLACE MAIN DIAGONALS
DEX = spdiags(-ones(M,1),0,DEX);
DEX = spdiags(+ones(M,1),+1,DEX);
% CORRECT BOUNDARY TERMS (DEFAULT TO DIRICHLET)
for ny = 1 : Ny-1
    neq = Nx*(ny-1) + Nx;
    DEX(neq,neq+1) = 0;
end
% HANDLE BOUNDARY CONDITIONS ON XHI SIDE
switch BC(2)
    case -2,
        dpx = exp(-i*kinc(1)*Nx*dx);
        for ny = 1 : Ny
            neq = Nx*(ny-1) + Nx;
            nv  = Nx*(ny-1) + 1;
            DEX(neq,nv) = +dpx;
        end
    case -1,
        for ny = 1 : Ny
            neq = Nx*(ny-1) + Nx;
            nv  = Nx*(ny-1) + 1;
            DEX(neq,nv) = +1;
        end
    case 0,     %Dirichlet
    otherwise,
      error('Unrecognized x-high boundary condition.')
        ;
end
% FINISH COMPUTATION
DEX = DEX / dx;
```

```
64 %%%%%%%%%%%%%%%%%%%%%%%%%%%%%%%%%%%%%%%%%%%%%%%%%%%%%%%%%%%%%%%%%%%%%%%%
65 % DEY
66 %%%%%%%%%%%%%%%%%%%%%%%%%%%%%%%%%%%%%%%%%%%%%%%%%%%%%%%%%%%%%%%%%%%%%%%%
67 % INITIALIZE MATRIX
68 DEY = sparse(M,M);
69 % PLACE MAIN DIAGONALS
70 DEY = spdiags(-ones(M,1),0,DEY);
71 DEY = spdiags(+ones(M,1),+Nx,DEY);
72 % HANDLE BOUNDARY CONDITIONS ON YHI SIDE
73 switch BC(4)
74     case -2,
75         dpy = exp(-i*kinc(2)*Ny*dy);
76         for nx = 1 : Nx
77             neq = Nx*(Ny-1) + nx;
78             nv  = nx;
79             DEY(neq,nv) = +dpy;
80         end
81     case -1,
82         for nx = 1 : Nx
83             neq = Nx*(Ny-1) + nx;
84             nv  = nx;
85             DEY(neq,nv) = +1;
86         end
87     case 0,
88     otherwise,
89       error('Unrecognized y-high boundary condition.')
           ;
90 end
91 % FINISH COMPUTATION
92 DEY = DEY / dy;
93 %%%%%%%%%%%%%%%%%%%%%%%%%%%%%%%%%%%%%%%%%%%%%%%%%%%%%%%%%%%%%%%%%%%%%%%%
94 % DHX
95 %%%%%%%%%%%%%%%%%%%%%%%%%%%%%%%%%%%%%%%%%%%%%%%%%%%%%%%%%%%%%%%%%%%%%%%%
96 % INITIALIZE MATRIX
97 DHX = sparse(M,M);
98 % PLACE MAIN DIAGONALS
99 DHX = spdiags(+ones(M,1),0,DHX);
100 DHX = spdiags(-ones(M,1),-1,DHX);
101 % CORRECT BOUNDARY TERMS (DEFAULT TO DIRICHLET)
102 for ny = 2 : Ny
```

```
    neq = Nx*(ny-1) + 1;
    DHX(neq,neq-1) = 0;
end
% HANDLE BOUNDARY CONDITIONS ON XLOW SIDE
switch BC(1)
    case -2,
        dpx = exp(+i*kinc(1)*Nx*dx);
        for ny = 1 : Ny
            neq = Nx*(ny-1) + 1;
            nv  = Nx*(ny-1) + Nx;
            DHX(neq,nv) = -dpx;
        end
    case -1,
        for ny = 1 : Ny
            neq = Nx*(ny-1) + 1;
            nv  = Nx*(ny-1) + Nx;
            DHX(neq,nv) = -1;
        end
    case 0,
    otherwise,
      error('Unrecognized x-low boundary condition.');
end
% FINISH COMPUTATION
DHX = DHX / dx;
%%%%%%%%%%%%%%%%%%%%%%%%%%%%%%%%%%%%%%%%%%%
% DHY
%%%%%%%%%%%%%%%%%%%%%%%%%%%%%%%%%%%%%%%%%%%
% INITIALIZE MATRIX
DHY = sparse(M,M);
% PLACE MAIN DIAGONALS
DHY = spdiags(+ones(M,1),0,DHY);
DHY = spdiags(-ones(M,1),-Nx,DHY);
% HANDLE BOUNDARY CONDITIONS ON YLOW SIDE
switch BC(3)
    case -2,
        dpy = exp(+i*kinc(2)*Ny*dy);
        for nx = 1 : Nx
            neq = nx;
            nv  = Nx*(Ny-1) + nx;
            DHY(neq,nv) = -dpy;
```

```
143         end
144     case -1,
145         for nx = 1 : Nx
146             neq = nx;
147             nv  = Nx*(Ny-1) + nx;
148             DHY(neq,nv) = -1;
149         end
150     case 0,
151     otherwise,
152       error('Unrecognized y-low boundary condition.');
153 end
154 % FINISH COMPUTATION
155 DHY = DHY / dy;
```

Appendices F

Quality Factor Tables

Table F.1: The dip properties of the reflected light intensities from 50 nm of silver sputtered using different deposition parameters at two different wavelengths

Ag (50 nm)		λ_o **= 594 nm**			λ_o **= 632.8 nm**		
Slew rate (%/s)	Dep. rate (Å/s)	FWHM (^{o})	Dip	QF	FWHM (^{o})	Dip	QF
4.0	1.0	0.65 ± 0.09	0.48 ± 0.01	0.75 ± 0.10	0.62 ± 0.09	0.44 ± 0.01	0.72 ± 0.10
	20.0	0.71 ± 0.04	0.49 ± 0.02	0.70 ± 0.06	0.57± 0.06	0.39 ± 0.01	0.70 ± 0.07
99.9	1.0	1.01 ± 0.12	0.60 ± 0.02	0.60 ± 0.08	0.84 ± 0.09	0.57 ± 0.02	0.68 ± 0.08
	20.0	0.94 ± 0.11	0.53 ± 0.02	0.57 ± 0.07	0.79 ± 0.08	0.37 ± 0.01	0.47 ± 0.05

Table F.2: The dip properties of the reflected light intensities from 50 nm of gold sputtered using different deposition parameters at two different wavelengths

Au (50 nm)		λ_o **= 594 nm**			λ_o **= 632.8 nm**		
Slew rate (%/s)	Dep. rate (Å/s)	FWHM (^{o})	Dip	QF	FWHM (^{o})	Dip	QF
4.0	1.0	4.34 ± 0.08	0.93 ± 0.01	0.21 ± 0.003	2.44 ± 0.09	0.76 ± 0.01	0.31 ± 0.02
	10.0	4.40 ± 0.44	0.85 ± 0.01	0.20 ± 0.02	2.51± 0.11	0.66 ± 0.01	0.26 ± 0.01
99.9	1.0	4.42 ± 0.43	0.84 ± 0.01	0.19 ± 0.02	2.41 ± 0.07	0.66 ± 0.01	0.27 ± 0.01
	10.0	4.29 ± 0.32	0.80 ± 0.01	0.19 ± 0.01	2.60 ± 0.09	0.57 ± 0.01	0.22 ± 0.01

Table F.3: The dip properties of the reflected light intensities from 40 nm of copper sputtered using different deposition parameters at two different wavelengths

Cu (40 nm)		λ_o **= 594 nm**			λ_o **= 632.8 nm**		
Slew rate (%/s)	Dep. rate (Å/s)	FWHM (^{o})	Dip	QF	FWHM (^{o})	Dip	QF
4.0	1.0	4.60 ± 0.14	0.62 ± 0.01	0.134 ± 0.003	2.76 ± 0.11	0.46 ± 0.01	0.167 ± 0.005
	10.0	3.06 ± 0.04	0.90 ± 0.01	0.29 ± 0.01	1.57 ± 0.08	0.82 ± 0.02	0.53 ± 0.04
99.9	1.0	4.08 ± 0.53	0.48 ± 0.02	0.12 ± 0.02	2.98 ± 0.09	0.61 ± 0.03	0.20 ± 0.01
	10.0	4.87 ± 0.33	0.78 ± 0.02	0.16 ± 0.01	3.27 ± 0.13	0.81 ± 0.01	0.25 ± 0.01

Appendices G

Experimental Tools

In the experiments of this thesis, we have used various experimental tools to fabricate nano-layers, and conduct light transmission and reflection measurements, thickness measurements, and morphological studies. This appendix will briefly discuss the prominent features of the used experimental tools.

Sputter Deposition System

Sputter deposition is a physical vapor deposition method based upon vaporizing a source material (target) by bombarding the target with Argon ions. To discharge the ejected atoms from the target and start film growth on a substrate, the most common approach is to use a magnetron source on the back of the target.

For the experiments in Chapter 4 and 5, we used an Angstrom Engineering Nexdep Deposition System to deposit different metals and dielectrics with various film thicknesses onto microscope glass substrates and silicon nitride membranes.

Atomic Force Microscope

Atomic-force microscopy (AFM) is a very-high-resolution type of scanning probe microscopy to measure local properties, such as height, with a probe. The demonstrated resolution of AFM is 1000 times better than the optical diffraction limit, in the order of fractions of a nanometer.

The AFM images in Chapter 5 are taken by the Bruker Dimension Icon AFM using the peak force tipping mode over the scan range of 5μm x 5μm. The measured average surface roughness of silver, gold and copper films fabricated using different deposition parameters are shown in the following table.

Table G.1: The measured average surface roughness of silver, gold and copper films fabricated at different deposition and slew rates.

Slew rate (%/s)	Dep. rate (Å/s)	Average surface roughness (nm)		
		Ag (50 nm)	Au (50 nm)	Cu (40 nm)
4.0	1.0	7.210	0.702	0.575
	10.0 / 20.0	2.210	0.727	0.458
99.9	1.0	7.050	0.525	0.478
	10.0 / 20.0	2.990	1.680	0.545

Scanning Electron Microscope

Scanning electron microscopy (SEM) is a type of nano-imaging that uses a focused beam of high energy electrons to produce high-resolution images of solid specimens. The interaction of electrons with atoms in the sample produces various signals that contain information about the sample's external morphology (texture), chemical composition, and crystalline structure. A resolution better than 1 nanometer is achievable by SEM.

The SEM images in Chapter 5 are taken by the Tescan Mira3 XMU Field Emission SEM using the high vacuum mode over various magnification levels and at different sites of the samples. The presented SEM images in this thesis are the best taken images at the highest magnification that provides an acceptable resolution.

Profilometer

Profilometer is a measuring instrument used to measure the thickness and the surface roughness of thin films. In Chapter 4, we used a mechanical stylus-based high resolution profilometer (KLA Tencor Alphastep) to measure the thicknesses of a series of thin-film samples in order to calibrate the quartz crystal monitoring system in the sputtering deposition station.

The stylus-based profilometers use a physically moving probe along the surface to acquire the surface height as a function of position. This process is performed by continuously monitoring the sample force pushing up the probe as it scans along the surface. The acquired sample forces are then used to reconstruct the surface. The probe's shape and tip size can affect measurements and restrict resolution. Typical profilometers are capable of measuring small vertical features ranging from 10 nanometres to 1 millimetre.

Spectrometer

Spectrometer is an instrument that measures the intensity of light as a function of wavelength. In this work, we used the high-performance Ocean Optics USB4000 spectrometer with a wavelength range, from 200 to 1100 nm for conducting the visible light transmission measurements of the silver-coated membranes.

Filmetrics F20 Analyzer

Filmetrics are usually used to measure the thickness and optical constants of dielectric and semiconductor thin films, where the measured films must be optically smooth and within the thickness range set by the system. Selecting the appropriate mode, filmetrics can also be used for reflection and transmission measurements. In this work, we used the Filmetrics F20 analyzer with a wide wavelength range from 380 to 1700 nm for conducting the visible and infrared light transmission measurements of the dielectric-coated silver films.